(2)

TECHNICAL REPORT BRL-TR-3261

BRL

COMPUTATIONAL STUDIES OF THE FLOW START-UP PROCESS IN TWO-DIMENSIONAL UNSTEADY DIVERGENT NOZZLES

DIXIE M. HISLEY

SEPTEMBER 1991

U.S. ARMY LABORATORY COMMAND

BALLISTIC RESEARCH LABORATORY
ABERDEEN PROVING GROUND, MARYLAND

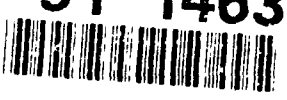

NOTICES

Destroy this report when it is no longer needed. DO NOT return it to the originator.

Additional copies of this report may be obtained from the National Technical Information Service, U.S. Department of Commerce, 5285 Port Royal Road, Springfield, VA 22161.

The findings of this report are not to be construed as an official Department of the Army position, unless so designated by other authorized documents.

The use of trade names or manufacturers' names in this report does not constitute indorsement of any commercial product.

DISCLAIMER NOTICE

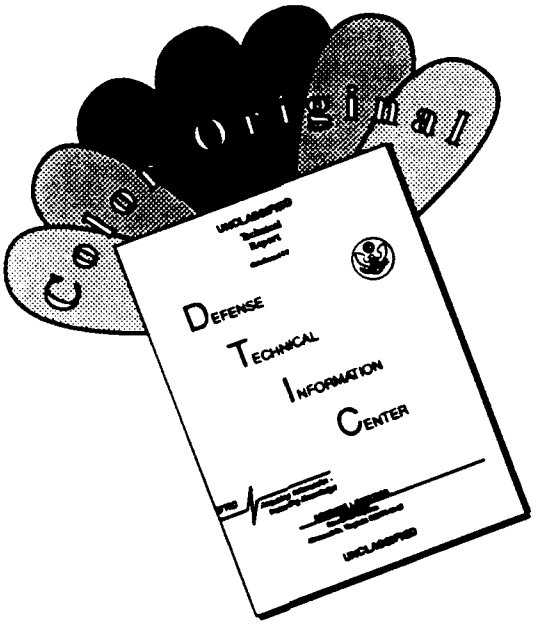

THIS DOCUMENT IS BEST QUALITY AVAILABLE. THE COPY FURNISHED TO DTIC CONTAINED A SIGNIFICANT NUMBER OF COLOR PAGES WHICH DO NOT REPRODUCE LEGIBLY ON BLACK AND WHITE MICROFICHE.

UNCLASSIFIED

REPORT DOCUMENTATION PAGE

Form Approved
OMB No. 0704-0188

1. AGENCY USE ONLY (Leave blank)	2. REPORT DATE	3. REPORT TYPE AND DATES COVERED
	September 1991	Final May 1990 - May 1991

4. TITLE AND SUBTITLE
Computational Studies of the Flow Start-Up Process in Two-Dimensional Unsteady Divergent Nozzles

5. FUNDING NUMBERS
WO: 44061-102-63-0001

6. AUTHOR(S)
Dixie M. Hisley

7. PERFORMING ORGANIZATION NAME(S) AND ADDRESS(ES)

8. PERFORMING ORGANIZATION REPORT NUMBER

9. SPONSORING / MONITORING AGENCY NAME(S) AND ADDRESS(ES)
U.S. Army Ballistic Research Laboratory
ATTN: SLCBR-DD-T
Aberdeen Proving Ground, MD 21005-5066

10. SPONSORING / MONITORING AGENCY REPORT NUMBER
BRL-TR-3261

11. SUPPLEMENTARY NOTES

12a. DISTRIBUTION / AVAILABILITY STATEMENT
Approved for public release; distribution is unlimited.

12b. DISTRIBUTION CODE

13. ABSTRACT *(Maximum 200 words)*

A two-dimensional computational study of the flow patterns that develop in unsteady overexpanded divergent nozzles with comparison to experimental data was performed and analyzed for two nozzle angles (16° and 45°). The computations were performed on a Cray XMP/48 supercomputer by discretizing the governing equations with an upwind, total variation diminishing (TVD), finite-volume, implicit scheme. Experimental shadowgraphs indicated viscous effects were present. Therefore, a systematic study was performed. First, the Euler equations were cast as the governing equations. The Euler equations produced computational results that compared well to inviscid theory, but did not reproduce experimental results. Next, the thin-shear layer equations were cast as the governing equations. Finally, the Baldwin Lomax turbulence model was added to the computational simulations.

The thin-shear layer viscous computations improved the comparison of density contour data to shadowgraph pictures over the inviscid computations for the 16°-nozzle configuration. However, the laminar viscous and turbulent computations did not significantly alter the inviscid static overpressure solutions for the 16° nozzle. The thin-shear layer viscous computations also improved the comparison of density contour data to shadowgraph pictures for the 45°-nozzle configuration. The 45° nozzle results showed that viscous effects alter the recompression shock system such that significantly different contour plots and pressure vs. time histories can result between the inviscid, laminar viscous, and turbulent solutions.

14. SUBJECT TERMS	15. NUMBER OF PAGES
computational fluid dynamics; divergent nozzles; gas dynamics; unsteady flow; large blast simulator; blast simulator; shock tube; Navier-Stokes; Baldwin Lomax Turbulence model	95
	16. PRICE CODE

17. SECURITY CLASSIFICATION OF REPORT	18. SECURITY CLASSIFICATION OF THIS PAGE	19. SECURITY CLASSIFICATION OF ABSTRACT	20. LIMITATION OF ABSTRACT
UNCLASSIFIED	UNCLASSIFIED	UNCLASSIFIED	UL

INTENTIONALLY LEFT BLANK.

TABLE OF CONTENTS

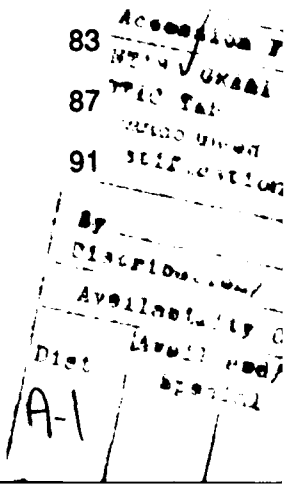

INTENTIONALLY LEFT BLANK.

LIST OF FIGURES

LIST OF FIGURES (Con't)

LIST OF FIGURES (Con't)

INTENTIONALLY LEFT BLANK.

ACKNOWLEDGMENTS

This author wishes to thank Dr. John Anderson, Dr. Mark Lewis, and Dr. Everett Jones for reviewing this work. Mr. Klaus O. Opalka is appreciated for providing the experimental results. Also, special thanks go to Dr. Man M. Rai, Gregory A. Molvik, and Christopher A. Atwood for their development and explanations of many of the concepts utilized in the computational approach.

INTENTIONALLY LEFT BLANK.

1. INTRODUCTION

1.1 Background. The U.S. Army is conducting research into the design and operation of a Large Blast/Thermal Simulator (LB/TS), essentially a large multi-driver shock tube with thermal capabilities, Figure 1. The goal of the LB/TS is to be a controllable experimental facility that will allow the Army to more efficiently test tactical equipment for nuclear hardness. The LB/TS will accomplish this goal by subjecting full-scale Army equipment to the same static pressure loading, dynamic pressure loading, and thermal pulse as the equipment would experience in the event of a nuclear explosion. The LB/TS is designed to produce varying duration decaying waveshapes over a range of primary shock overpressures.

Early LB/TS designs utilized convergent-divergent nozzles to retard the outflow of the high-pressure driver gas, thus generating long duration waveforms. Convergent-divergent nozzles have been investigated by many authors and an excellent review of efforts predating 1968 have been presented by Amann (1968). The efforts of previous investigators as reported by Amann can be split into two groups. In one group, the unstationary starting procedure within the jet is analyzed whereas, the other group concentrates on the newly formed quasi-stationary conditions downstream of the diverging nozzle exit and beginning after its start-up. A more recent effort, which uses computational fluid dynamics (CFD) techniques, to investigate the start-up process of a shock tunnel as well as the quasi-stationary conditions downstream of an M = 6 designed nozzle is presented by Byun et al. (1990). In this paper, the flow start-up time required to get quasi-steady flow around a circular cylinder downstream of the nozzle exit is computationally determined to be 9.5 milliseconds.

From an LB/TS standpoint, the unstationary starting procedure in the jet flow is of interest as well as the flow after the start-up of the jet. However, the LB/TS is designed (through the different volumes and lengths of the multiple drivers among other wave-shaping techniques) so that the flow after the start-up of the jet produces unsteady, gradually decaying waveforms at test stations of interest. See Figure 2 for an example of a typical static and dynamic pressure blast waveform obtained from an existing blast simulator in France. The static pressure was recorded from a probe located in the shock tube wall and seven diameters

downstream from the beginning of the driven section. A stagnation probe was located at the same x location, but, approximately one quarter diameter off the shock tube wall.

The advantage of diverging nozzles in an LB/TS is to reduce the pressure losses associated with the large area discontinuity at the exit of the nozzle throat (shown in Figure 1). The disadvantages are a pressure spike that appears at the front of the blast wave which becomes larger as the diverging nozzle cone angle is made smaller and the additional thrust formed by the driver/nozzle combination on the reaction pier. Added to these concerns is the question of the effect of the diverging nozzles on the desired smoothly decaying static and dynamic pressure blast loading waveforms. Diverging nozzles after the throat sections are not shown in the design of Figure 1, but are still under consideration for the proposed LB/TS facility.

The complex three-dimensional (3-D) geometry of the proposed LB/TS would require hundreds of hours of Cray cpu time for computer simulations. From an engineering design standpoint, this is unacceptable. A computationally efficient tool is needed to perform design parametric studies and obtain gross flow properties for the LB/TS at a reasonable cost. A significant influence on the gas dynamics which result in the LB/TS shock tube (ignoring for this study the thermal simulation) is due to the area ratios present in the geometry. Therefore, one technique to simplify the 3-D problem is to keep the same length scales along the axis of the shock tube, but compute a two-dimensional (2-D) axisymmetric or quasi-one-dimensional (1-D) approximation to the 3-D geometry as follows:

$$D_2 = \frac{\sqrt{4A_3}}{\pi}, \tag{1}$$

$$A_1 = A_3, \tag{2}$$

where A_3 is the 3-D cross-sectional area, D_2 is the 2-D axisymmetric diameter, and A_1 is the 1-D area necessary to maintain equivalent area ratios. The cross-sectional areas of the multiple varying length drivers, converging nozzles, and throat sections are lumped into one driver for the 2-D and 1-D geometries.

As shown in Figure 3, 1/57 scale 2-D axisymmetric shock tubes have been built as experimental tools for LB/TS design studies. These lumped area approximations to the 3-D

facility have been built with and without diverging nozzles to study the resultant flow characteristics. Another difference between the tubes that is evident in Figures 3b and 3c, but is not relevant to this study, is that the stepped driver was replaced with a single diameter driver to facilitate volume versus flow duration studies. These 2-D axisymmetric shock tubes were computationally modeled with 1-D and 2-D computer algorithms for comparison to the experimental results and to gain insight into the flow physics present in divergent flows. The next sections comment on the significant flow physics that are captured by each added dimension of geometry as well as the results of previous computational modeling efforts.

The flow patterns encountered in the quasi-one-dimensional simulations for low shock overpressures (< 28 kPa) are similar to the flow patterns which develop in a straight shock tube, as shown in Figures 4a and 4b (Pearson, Opalka, and Hisley 1985). After diaphragm burst, the flow consists of a primary shock moving to the right of the diaphragm into the diverging nozzle and driven section which is open to ambient air at its end. The primary shock is followed by a contact surface which separates the gas processed by the shock from the gas initially in the driver. A rarefaction wave travels to the left of the diaphragm which accelerates and cools the driver gas. The flow is subsonic everywhere in the simulator with an expansion of the flow (velocity increase, pressure decrease) in the convergent nozzle and a compression (velocity decrease, pressure increase) in the divergent nozzle. For subsonic flow through the convergent-divergent nozzle, the flow is always isentropic. Also shown in Figures 4a and 4b are typical pressure versus distance histories, at early time after diaphragm burst, for a straight shock tube, and for the quasi-one-dimensional Q1D LB/TS.

As the shock overpressure is increased to the 28 to 70 kPa regime, the flow becomes choked in the throat and expands supersonically in the divergent nozzle to very low static pressure. Because the flow behind the primary shock is subsonic and at a higher static pressure, a recompression shock must form to match the two flow states, Figure 4c. Typically, the recompression shock stands somewhere in the divergent nozzle. For the highest shock overpressures of interest, above 70 kPa, the recompression shock may be swept out of the nozzle and into the driven section.

In addition to the nozzle flow, the rarefaction wave generated at diaphragm burst reflects from the closed end of the drivers. The rarefaction then moves forward, is partially

transmitted and partially reflected by the converging nozzle. The transmitted rarefaction eventually overtakes the shock and decreases the pressure. The reflected rarefaction moves back into the driver and reflects again from the closed end of the driver. Thus, a series of rarefactions overtake the shock, which effectively empties the shock tube to ambient conditions while producing pressure versus time histories that gradually decay to ambient and are reasonable simulations of blast waveforms.

Up to this point, the LB/TS flow patterns have been described by means of a 1-D analysis. However, the flow that develops in the diverging nozzle at shock overpressures above 28 kPa are better represented by a 2-D analysis. From experimental shadowgraphs and computations (Amann 1982; Hisley and Molvik 1986), it is readily discovered that the recompression shock that develops in a divergent flow area is not planar, as a 1-D analysis indicates, but consists of a system of oblique and normal shocks as shown in Figure 5. Finally, the mixing of the flows from the separate drivers in the LB/TS can only be fully captured by a 3-D calculation.

However, as stated earlier, 3-D calculations are not practical from a cost-effective engineering standpoint, therefore, the initial analysis work for the LB/TS has been done with experiments performed in single-driver, 1/57 scale, 2-D axisymmetric shock tubes and with the Ballistic Research Laboratory Quasi-One-Dimensional (BRL-Q1D) Code (Coulter 1987a, 1987b; Opalka and Mark 1986). A comparison of the experimental results and the results of the BRL-Q1D code showed that the code modeled low shock pressure cases with reasonable accuracy, but, as expected from the previous discussion, was less accurate at higher shock overpressures. The deviations were attributed to the strong influence of 2-D effects caused by the large and rapid area expansion downstream of the throat section, typical of the LB/TS geometry.

A 2-D axisymmetric inviscid code, BLAST2D, was developed to better simulate the flow in the small-scale LB/TS axisymmetric shock tubes. The code was originally written by this author in 1985 during a six month stay at NASA Ames Research Center. During this time period, Dr. Man Mohan Rai was an excellent mentor who provided explanations of many state-of-the-art computational fluid dynamics (CFD) concepts, such as the incorporation of Riemann problems and the use of Total Variation Diminishing (TVD) concepts into solution

algorithms. In subsequent years, a joint effort was maintained between BRL and NASA Ames to further develop the code. Significant contributions were the addition and validation of a laminar viscous subroutine and the addition of the Baldwin-Lomax turbulence model by Gregory A. Molvik (1987) and an extension and validation of the code to three dimensions (BLAST3D) by Christoper A. Atwood (to be published).

A recent validation of the inviscid BLAST2D algorithm was published by Hisley (1990a). Computations were performed for the reflection of planar shocks from wedge surfaces. An extensive amount of experimental, theoretical, and computational data has been published (Glaz et al. 1986; Shirouzu and Glass 1984; Deschambault and Glass 1983; Lock and Dewey 1989) for the reflection of planar shocks from various inclined rigid surfaces. The wealth of qualitative and quantitative data available makes the simulation of these problems a good choice for computer code verification and comparison. The BLAST2D code was shown in this report to produce accurate results which compared well to theory, experimental data, and computational results from an established code, the SHARC code (Hikida, Bell, and Needham 1988). Other authors who have developed codes and published results in the past for the simulation of blast wave/target interaction problems (external flow problems) are noted in Mark and Kutler (1983), Bennet, Abbett, and Wolf (1986), and Yee (1987).

In a previous report (Hisley and Molvik 1986), BLAST2D results were presented for the shock tube configuration in Figure 3a. Computational/experimental comparisons of static pressure were improved over Q1D predictions for this configuration, however, dynamic pressure comparisons were still poor. Figure 6 presents typical computational pressure and density contour plots. Figure 7 presents typical static pressure and dynamic pressure comparisons from this reference. The static pressure was recorded from a probe located in the shock tube wall and seven diameters downstream from the beginning of the driven section. A stagnation probe was located at the same x location, but, approximately one quarter diameter off the shock tube wall.

Another report (Hisley 1986b) furthered the investigation for LB/TS geometries shown in Figures 3b and 3c. Typical static and stagnation overpressure plots from this reference are shown in Figure 8. Temperature, pressure, and numerical accuracy variations were performed and analyzed to see if new insight about the physics of the flow and reasons for

computational/experimental discrepancies could be obtained. The significant conclusion of this report was to confirm that overexpanded diverging nozzles, particularly as the expansion angle increased, were not properly modeled by an inviscid code and that physical dissipation was present experimentally that was not being modeled numerically. As a result of these findings, it was concluded that better understanding of the flow development in divergent flows was required.

Experiments were next performed in overexpanded 2-D planar nozzles, Figure 9, to obtain shadowgraphs of divergent flows as well as pressure versus time histories (Reichenbach and Opalka 1990). The area ratios of the planar convergent-divergent nozzles were on the order of the area ratios considered for the LB/TS. The experiments were performed in planar nozzles instead of axisymmetric in order to facilitate the taking of shadowgraph pictures.

1.2 Objectives. Using the BLAST2D code, a systematic study of the unsteady, overexpanded 2-D planar nozzle experiments is performed; first, with an inviscid algorithm and then again with thin-layer laminar viscous terms added and finally with the addition of the Baldwin-Lomax turbulence model. The objective of this report is to obtain better insight into the flow processes that develop in diverging nozzles and how to computationally simulate that flow. As stated earlier, previous efforts by this author for 2-D axisymmetric converging-diverging nozzle configurations only involved inviscid computations. Therefore, this report will go beyond previous work by performing not only inviscid computations, but laminar viscous and turbulent computations as well. Furthermore, an assessment of the effect of including the viscous terms will be made with emphasis on the changes that occur in static pressure versus time, dynamic pressure versus time, and contour plots. Particular emphasis will be placed on how well the computational simulations compare to the experimental data. It is important for the computations to compare well to the experimental data so that the BLAST2D code can be used with confidence in the future as a complement to the experimental database that will be obtained with the LB/TS facility.

2. GOVERNING EQUATIONS

This section introduces the Navier-Stokes equations in 2-D Cartesian coordinates and integral form. Subsequently, the governing equations are nondimensionalized, transformed to

body-conformal coordinates, and the thin-layer viscous stress assumption is applied. Finally, the governing equations are presented in discrete form for a generalized control volume.

2.1 Navier-Stokes Equations. The governing equations are the 2-D compressible Navier-Stokes equations, written in integral form,

$$\frac{d}{dt}\int_v Q d\mathcal{V} + \int_s n \cdot G dS = 0 \tag{3}$$

where $\mathcal{V}$ is the cell volume, ndS is the projection of surface area with outward normal n, Q is the vector of conserved variables per unit volume,

$$Q = \begin{pmatrix} \rho \\ \rho u \\ \rho v \\ e \end{pmatrix} \tag{4}$$

and G is a second order tensor of the inviscid and viscous flux of Q expanded in terms of vectors E and F below:

$$E = \begin{pmatrix} \rho u \\ \rho u^2 + p + \tau_{xx} \\ \rho uv + \tau_{xy} \\ (e + p) + \tau_{xx}u + \tau_{xy}v + q_x \end{pmatrix}, \quad F = \begin{pmatrix} \rho v \\ \rho uv + \tau_{yx} \\ \rho v^2 + p + \tau_{yy} \\ (e + p)v + \tau_{yx}u + \tau_{yy}v + q_y \end{pmatrix} \tag{5}$$

This set of four integral equations represents the conservation of mass, momentum in x (longitudinal) and y directions (height), and energy per unit volume. The density is ρ, the pressure is p, the velocities in the x and y directions are u and v, respectively. The total energy per unit volume is e, where

$$e = \frac{p}{(\gamma - 1)} + 1/2\rho\,(u^2 + v^2) \tag{6}$$

The total energy per unit volume is related to the internal energy per unit mass, ε, by $\varepsilon = \rho\,\varepsilon + \rho\,(u^2 + v^2)/2$. An equation of state $p = p(\rho, \varepsilon)$ is required to complete the system of equations. A perfect gas equation of state $p = \rho\,RT$ is used in this study with the assumption that intermolecular forces are negligible. A real gas equation of state is required when intermolecular forces are important, that is, for very high pressures, p on the order of

1,000 atm, and/or low temperatures, T on the order of 30 K (Anderson 1989). Also, a calorically perfect gas is assumed which implies constant specific heats, that is, negligible electronic and vibrational molecular modes. Thus, $\varepsilon = c_v T$, $h = c_p T$, and $\gamma = 1.4$ apply.

The viscous stress terms are defined below with the assumption that Stokes' hypothesis can be used to define the relationship between the first, second, and bulk viscosity coefficients. Thus, the bulk coefficient ζ is zero, and the first and second coefficients are related through $\lambda = -2/3\ \mu$. Stokes' hypothesis is strictly valid only for monatomic gases, but is frequently used when the relative effects of the shearing stress are much larger than the dilational stress effects (Jones 1989). The viscous stress terms are

$$\begin{aligned} \tau_{xx} &= -2\mu\frac{\partial u}{\partial x} + \frac{2}{3}\mu\left(\frac{\partial u}{\partial x} + \frac{\partial v}{\partial y}\right) \\ \tau_{yy} &= -2\mu\frac{\partial v}{\partial y} + \frac{2}{3}\mu\left(\frac{\partial u}{\partial x} + \frac{\partial v}{\partial y}\right) \\ \tau_{xy} &= -\mu\left(\frac{\partial u}{\partial y} + \frac{\partial v}{\partial x}\right) \end{aligned} \tag{7}$$

Fourier's law for heat transfer by conduction defines q_x and q_y,

$$q = -(q_x + q_y) = -k\Delta T = -\frac{\mu c_p}{Pr}(T_x + T_y) \tag{8}$$

The Prandtl number, which relates the diffusion of momentum to the diffusion of heat, is constant at .72 for air. Finally, the thermal conductivity and the viscosity are related through the use of Sutherland's formula

$$\frac{\mu}{\mu_{ref}} = \left(\frac{T}{T_{ref}}\right)^{3/2}\left(\frac{T_{ref} + 110K}{T + 110K}\right) \tag{9}$$

where Sutherland's formula is valid in the range of temperature from 100 K to 1,888 K.

2.2 Nondimensionalization. To this point, the variables and equations have been presented in dimensional form. If a change of notation is made such that dimensional quantities are now denoted by a ~, then the variables can be nondimensionalized as follows:

$$x = \frac{\tilde{x}}{\tilde{L}} \quad u = \frac{\tilde{u}}{\tilde{c}_1} \quad p = \frac{\tilde{p}}{\tilde{p}_1}$$

$$y = \frac{\tilde{y}}{\tilde{L}} \quad v = \frac{\tilde{v}}{\tilde{c}_1} \quad e = \frac{\tilde{e}}{\tilde{\rho}_1 \tilde{c}_1^2} \tag{10}$$

$$\rho = \frac{\tilde{\rho}}{\tilde{\rho}_1} \quad t = \frac{\tilde{t}\tilde{c}_1}{\tilde{L}} \quad \mu = \frac{\tilde{\mu}}{\tilde{\mu}_1}$$

The reference length $\tilde{L}$ is equal to 1 m, the reference speed of sound is $\tilde{c}_1 = \sqrt{\frac{\tilde{p}_1}{\tilde{\rho}_1}}$, and the superscript 1 represents the ambient conditions initially present in the driven section. The Reynolds number is defined as

$$Re = \frac{\tilde{\rho}_1 \tilde{c}_1 \tilde{L}}{\tilde{\mu}_1} \tag{11}$$

With this nondimensionalization and change of notation, the equations look identical to those already presented except a factor of $\frac{1}{Re}$ multiplies the viscous stress and heat transfer terms. Also, the nondimensional Fourier's law for heat transfer and Sutherland's formula become respectively,

$$q = -(q_x + q_y) = -\frac{\mu\gamma}{(\gamma - 1)\,Pr}(T_x + Ty) \tag{12}$$

$$\mu = T^{3/2}\left(\frac{1 + 110K/\tilde{T}_1}{T + 110K/\tilde{T}_1}\right) \tag{13}$$

2.3 Transformation to Computational Space. The physical, independent variables (x, y, t) are transformed into a body-conformal, curvilinear grid (ξ, η, τ) by a general transformation of the form

$$\tau = t$$

$$\xi = \xi(x, y)$$

$$\eta = \eta(x, y) \tag{14}$$

Note that ξ and η are not functions of t; thus, this transformation only holds for grids that are constant with respect to time.

In order to satisfy boundary conditions on arbitrarily shaped boundaries, it is convenient to make this transformation. Thus, a variety of geometries can be treated with the same coding. The lower and upper walls of the shock tube lie along the constant η lines of 1 and *jmax*, respectively, where *jmax* is the total number of grid points in the y direction. The right and left walls of the shock tube lie along the constant ξ lines of 1 and *imax*, respectively, where *imax* is the total number of grid points in the x direction. The indices *i* and *j* correspond to the ξ and η directions, respectively, in the computational mesh. The cell center of an elemental volume in the grid is denoted by (*i, j*), the right and left cell walls are located at (*i + 1/2, j*) and (*i - 1/2, j*). The top and bottom cell walls are located at (*i, j + 1/2*) and (*i, j - 1/2*). Application of the chain rule of differentiation yields

$$\begin{aligned} \frac{\partial}{\partial \tau} &= \frac{\partial}{\partial t} \\ \frac{\partial}{\partial \xi} &= x_\xi \frac{\partial}{\partial x} + y_\xi \frac{\partial}{\partial y} \\ \frac{\partial}{\partial \eta} &= x_\eta \frac{\partial}{\partial x} + y_\eta \frac{\partial}{\partial y} \end{aligned} \tag{15}$$

The inverse transformation is

$$\begin{aligned} \frac{\partial}{\partial t} &= \frac{\partial}{\partial \tau} \\ \frac{\partial}{\partial x} &= \xi_x \frac{\partial}{\partial \xi} + \eta_x \frac{\partial}{\partial \eta} \\ \frac{\partial}{\partial y} &= \xi_y \frac{\partial}{\partial \xi} + \eta_y \frac{\partial}{\partial \eta} \end{aligned} \tag{16}$$

The metrics ξ_x, ξ_y, η_x, η_y, can be solved for in terms of the inverse metrics x_ξ, y_ξ, x_η, y_η with the result,

$$\begin{aligned} \xi_x &= y_\eta J \qquad \eta_x = -y_\xi J \\ \xi_y &= -x_\eta J \qquad \eta_y = x_\xi J \\ J &= (x_\xi y_\eta - x_\eta y_\xi)^{-1} \end{aligned} \tag{17}$$

The Jacobian of the coordinate transformation, J, is equivalent to the inverse of the cell volume, $\mathcal{V}$.

Application of the chain rule with these metrics to Eq. 3 transforms the governing equations to computational space. For a 2-D cell, the integration of flux over the surface in Eq. 3 is replaced by an integral over each face of the cell. Thus, the integral form of the transformed nondimensionalized thin-layer Navier-Stokes equations for a 2-D generalized cell volume becomes,

$$\frac{d}{dt}\int_{\mathcal{V}} Q\,d\mathcal{V} + \int_{j-1/2}^{j+1/2}(E_{i+1/2} - E_{i-1/2})\,d\eta + \int_{i-1/2}^{i+1/2}(F_{j+1/2} - F_{j-1/2})\,d\xi = \frac{1}{Re}\int_{i-1/2}^{i+1/2}(S_{j+1/2} - S_{j-1/2})\,d\xi \tag{18}$$

where, in terms of the inverse metrics,

$$Q = \begin{pmatrix} \rho \\ \rho u \\ \rho v \\ e \end{pmatrix}, \quad E = \begin{pmatrix} \rho U \\ \rho U u + y_\eta p \\ \rho U v - x_\eta p \\ (e + p)U \end{pmatrix}, \quad F = \begin{pmatrix} \rho V \\ \rho V u - y_\xi p \\ \rho V v + x_\xi p \\ (e + p)V \end{pmatrix} \tag{19}$$

The viscous stress terms have been grouped together and placed on the right-hand side as vector S in Eq. 18. The viscous stress terms have been nondimensionalized, transformed to computational space, and a thin, shear layer approximation has been assumed. The thin-layer viscous stress assumption neglects diffusion parallel to the surface of the shock tube. Thus, all $\partial(*)/\partial\xi$ stress terms are neglected. In contrast to boundary layer theory, the full, normal momentum equation is retained and no assumptions are made about the normal pressure. After algebraic manipulation, the vector S has the form (Molvik 1987)

$$S = \frac{1}{\mathcal{V}}\begin{pmatrix} 0 \\ \mu m_1 u_\eta - \frac{\mu}{3} m_2 y_\xi \\ \mu m_1 v_\eta + \frac{\mu}{3} m_2 x_\xi \\ \frac{\mu m_1}{2}(u^2 + v^2)_\eta + \frac{\mu}{3} V\mu_2 + \frac{\mu\gamma}{(\gamma - 1)Pr} m_1 T_\eta \end{pmatrix} \tag{20}$$

The contravariant velocities U and V, written in terms of the inverse metrics and the constants m_1 and m_2 are, respectively,

$$u = y_\eta u - x_\eta v \qquad V = y_\xi u + x_\xi v \tag{21}$$

$$m_1 = y_\xi^2 + x_\xi^2 \qquad m_2 = -y_\xi u_\eta + x_\xi v_\eta \tag{22}$$

If an average flux is defined on the cell faces and $\Delta\xi$ and $\Delta\eta$ are set to unity, the integral form of the Navier-Stokes equations can be rewritten in discrete form as

$$\mathcal{V}_{i,j}\frac{\bar{Q}_{i,j}^{n+1} - \bar{Q}_{i,j}^{n}}{\Delta\tau} + (\hat{E}_{i+1/2,j}^{m} - \hat{E}_{i-1/2,j}^{m}) + (\hat{F}_{i,j+1/2}^{m} - \hat{F}_{i,j-1/2}^{m}) = \frac{1}{Re}(\hat{S}_{i,j+1/2}^{m} - \hat{S}_{i,j-1/2}^{m}) \tag{23}$$

The vectors $\hat{E}$ and $\hat{F}$ are the convective numerical fluxes, to be defined later, in computational space (τ, ξ, η) consistent with the transformed physical fluxes E and F in (τ, ξ, η). The vector $\bar{Q}$ consists of the cell-averaged dependent variables. The integration scheme is fully implicit if $m = n + 1$ and is explicit if $m = n$. The vector $\bar{Q}$ evaluated at time level n represents known or initial conditions in Eq. 23. Thus, once the numerical fluxes in Eq. 23 are evaluated, $\bar{Q}$ at time level $n + 1$ can be solved for. The next section presents mathematical details of the techniques used to discretize and evaluate the fluxes presented in Eq. 22.

3. NUMERICAL ALGORITHM

3.1 Introduction. Discretization of the governing equations into an upwind, TVD, finite-volume, implicit scheme produces an algorithm that is well suited for blast wave calculations, because, upwind flux difference splitting with TVD achieves second-order accuracy without introducing spurious oscillations near discontinuities. Strong gradients and complex flow fields are resolved accurately. TVD schemes are often referred to as a modern shock-capturing method due to the fact that the numerical dissipation terms are nonlinear, that is, the amount of dissipation is controlled by automatic feedback mechanisms that can vary from one grid point to another. Also, the dissipation is scaled to the underlying eigensystem of the hyperbolic Euler equations. In classical shock-capturing methods, as reported by

Yee (1987), the numerical dissipation terms are either linear such that the same amount of numerical dissipation is added at all grid points or the numerical dissipation is controlled by parameters that must be optimized. Classical shock-capturing methods typically result in oscillatory solutions at strong discontinuities.

The advantages of classical techniques are programming simplicity and adequate resolution for weak gradient problems. However, for the complex flow fields and strong gradients typical of blast problems, upwind differencing with TVD provides better resolution. The disadvantage of upwind differencing with TVD are longer computing times caused by an increase in the number of arithmetic operations per integration step and loss of programming simplicity. The results shown in this paper were generated on a Cray XMP/48 and typically took one hour of cpu time for the inviscid case, to five hours of cpu time for the viscous case.

Conservative schemes capture shocks and other discontinuities automatically. The finite volume philosophy ensures conservation at interior points. The scheme is made implicit by linearizing only the first-order contribution and by employing a Newton iteration of the type described by Rai (1984) to reduce the linearization and factorization errors. The implicit version of the scheme requires more computations per integration step than the explicit version, but permits larger time steps which, for stiff problems, reduces computational expense.

The next section presents the first-order accurate upwind scheme which is the foundation of the computational algorithm. Subsequently, the first-order scheme is expanded to second-order accuracy with the addition of second-order terms and TVD concepts. Development of the implicit version of the algorithm and the Newton iterative procedure used is presented. Next, boundary conditions are discussed. Finally, the turbulence modeling is described.

3.2 First-Order Scheme.

3.2.1 Upwind Flux Difference Splitting and the Riemann Problem. An understanding of upwind flux difference splitting begins with an examination of the mathematical nature of the unsteady Euler equations. Steger and Warming (1981) report that if the equation of state used to close the Euler equations has the functional form $p = \rho f(\varepsilon)$, then the nonlinear flux

vectors $E(Q)$ and $F(Q)$ are homogeneous functions of degree one in Q, that is $E(\alpha Q) = \alpha E(Q)$ for any value α and similarly for F. Thus, the flux vectors can be shown to be equivalent to

$$E = AQ \tag{24}$$

$$F = BQ \tag{25}$$

where A and B are the Jacobian matrices $\frac{\partial E}{\partial Q}$ $\frac{\partial F}{\partial Q}$, respectively. For the hyperbolic Euler equations, A and B have a complete set of linearly independent eigenvectors such that a similarity transformation exists. This similarity transformation for the ξ direction flux is,

$$A = R \Lambda R^{-1} \tag{26}$$

where R is the right eigenvector matrix, R^{-1} is the left eigenvector matrix and Λ represents the diagonalized eigenvalue matrix,

$$R = \frac{1}{2}\begin{pmatrix} 1/c & 1/c & 1/c & 1/c \\ \frac{u}{c} - \hat{S}_x & \frac{u}{c} - \hat{S}_y & \frac{u}{c} + \hat{S}y & \frac{u}{c} + \hat{S}_x \\ \frac{v}{c} - \hat{S}_y & \frac{v}{c} + \hat{S}_x & \frac{v}{c} - \hat{S}_y & \frac{v}{c} + \hat{S}y \\ \frac{q^2}{2c} - \hat{U} + \frac{c}{\chi} & \frac{q^2}{2c} + \hat{V} & \frac{q^2}{2c} - \hat{V} & \frac{q^2}{2c} + \hat{U} + \frac{c}{\chi} \end{pmatrix} \tag{27}$$

$$R^{-1} = \begin{pmatrix} \frac{\chi q^2}{2c} + \hat{U} & -\frac{\chi}{c}u - \hat{s}_x & -\frac{\chi}{c}v - \hat{s}_y & \frac{\chi}{c} \\ -\frac{\chi q^2}{2c} - \hat{V} + c & \frac{\chi}{c}u - \hat{s}_y & \frac{\chi}{c}v + \hat{s}_x & -\frac{\chi}{c} \\ -\frac{\chi q^2}{2c} + \hat{V} + c & \frac{\chi}{c}u + \hat{s}_y & \frac{\chi}{c}v - \hat{s}_x & -\frac{\chi}{c} \\ \frac{\chi q^2}{2c} - \hat{U} & -\frac{\chi}{c}u + \hat{s}_x & -\frac{\chi}{c}v + \hat{s}_y & \frac{\chi}{c} \end{pmatrix} \tag{28}$$

$$\Lambda = diag\left[U - \sqrt{x_\eta^2 + y_\eta^2}\ c,\ U,\ U,\ U + \sqrt{x_\eta^2 + y_\eta^2}\ c\right] \tag{29}$$

where

$$\begin{aligned}
\hat{s}_x &= y_\eta / \sqrt{x_\eta^2 + y_\eta^2} \\
\hat{s}_y &= -x_\eta / \sqrt{x_\eta^2 + y_\eta^2} \\
\hat{U} &= u\hat{s}_x + v\hat{s}_y \\
\hat{V} &= v\hat{s}_x - u\hat{s}_y \\
q^2 &= u^2 + v^2 \\
\chi &= \gamma - 1
\end{aligned}$$

The eigenvalue matrix can be split according to the sign of the eigenvalues (characteristic speeds), thus $\Lambda = \Lambda^+ + \Lambda^-$. The superscript + denotes positive eigenvalues, or from characteristic theory, right-running waves and the superscript - denotes negative eigenvalues or left-running waves. Also, the Jacobian matrix A can be split,

$$A = A^+ + A^- \tag{30}$$

where

$$A^+ = R\,\Lambda^+\,R^{-1} \qquad A^- = R\,\Lambda^-\,R^{-1}$$

Similarly, B^+ and B^- can be constructed by replacing x_η with $-x_\xi$, and y_η with $-y_\xi$. From a purely mathematical analysis of the Euler equations, a more physical picture of right and left moving waves emerges which in turn suggests the use of the Riemann problem to determine the constant states separated by the wave families.

Riemann problems are the building blocks upon which the upwind flux differencing is performed. Therefore, it is appropriate to interject at this point exactly what the Riemann problem is and how it is incorporated into the numerical solution procedure. Consider the dependent variables at cell centers for all the cells in the grid, as pairs of states defining a sequence of 1-D Riemann problems. The Riemann problem for the ξ direction Figure 10, is: Given two states ($\rho 1$, *u1*, *p1*) and ($\rho 4$, *u4*, *p4*) determine the combination of shocks, contact discontinuities, and expansions which result in these end states, that is, determine ($\rho 2$, *u2*, *p2*) and ($\rho 3$, *u3*, *p3*). For the Riemann problem in the η direction, substitute *v* for *u*.

To obtain an exact solution of states 2 and 3, Riemann solvers require an iterative procedure which is computationally expensive when performed for a large number of cells and time steps. The expense of producing an exact solution to the Riemann problem is justified only if the information made available could be put to some sophisticated use. The approximate Riemann solvers are considerably less expensive because the Riemann problem is solved with a direct non-iterative method which is about as time consuming as one cycle of the iterative procedures. Comparisons of the solutions from the exact vs. approximate Riemann solvers reveal slight differences. Other approximate Riemann solvers could have been used, but Roe's method is the approach recommended by Chakravarthy (1985) when computational efficiency is important.

From either an exact or approximate solution to the Riemann problem, the change in flux across the right running and left running wave families can be determined, respectively. Upwinding requires that the change in flux or flux difference across right running wave families (positive eigenvalues) be used in the derivative evaluations of fluxes into neighboring fluid cells to the right of the Riemann solution and that the flux difference across left running wave families (negative eigenvalues) be used in the derivative evaluations of fluxes into neighboring fluid cells to the left. In this way a method of characteristic-like flavor is brought into the numerical algorithm and the concept of upwind flux difference splitting is illustrated.

The flux change associated with the waves traveling in the positive ξ direction is given the symbol ΔE^{+} and that in the negative direction is represented by ΔE^{-}. The flux remaining at the interface for all time associated with this Riemann problem must then be represented by either of the following equations:

$$\hat{E}_{i+1/2} = E_i + \Delta E^{-}_{i+1/2} \tag{31}$$

$$\hat{E}_{i+1/2} = E_{i+1} - \Delta E^{+}_{i+1/2} \tag{32}$$

or, by averaging the two equations, the final form of the numerical flux becomes,

$$\hat{E}_{i+1/2} = 1/2\,(E_i + E_{i+1} + \Delta E^{-}_{i+1/2} - \Delta E^{+}_{i+1/2}) \tag{33}$$

The flux difference across the positive and negative velocity waves can be calculated:

$$\Delta E^{+}_{i+1/2} = 1/2\,(R_{i+1/2}(\Lambda + |\Lambda|)_{i+1/2} R^{-1}_{i+1/2})\,(\bar{Q}_{i+1} - \bar{Q}_i) = A^{+}(\bar{Q}_{i+1} - \bar{Q}_i) \qquad (34)$$

$$\Delta E^{-}_{i+1/2} = 1/2\,(R_{i+1/2}(\Lambda - |\Lambda|)_{i+1/2} R^{-1}_{i+1/2})\,(\bar{Q}_{i+1} - \bar{Q}_i) = A^{-}(\bar{Q}_{i+1} - \bar{Q}_i) \qquad (35)$$

However, the dependent variables are not defined at the cell interfaces where these matrices must be evaluated.

3.2.2 Roe's Approximate Riemann Solver. Roe (1981) has developed a special averaging process to calculate the dependent variables on the cell interface and satisfy the following relations:

(1) $[A]^{Roe}_{i+1/2}$ constitutes a linear mapping from the vector space Q to the vector space E.

(2) $[A]^{Roe}_{i+1/2} \rightarrow A_{i+1/2} = \partial E/\partial Q$.

(3) $\hat{E}_{i+1} - \hat{E}_i = [A]^{Roe}_{i+1/2}(\bar{Q}_{i+1} - \bar{Q}_i) = [A^{+} + A^{-}]^{Roe}_{i+1/2}(\bar{Q}_{i+1} - \bar{Q}_i)$

(4) The eigenvectors of $[A]^{Roe}_{i+1/2}$ are linearly independent.

By satisfying the relations above, called Property U (intent of Property U is to insure *uniform* validity across discontinuities) by Roe, the shock capturing capabilities of the algorithm are retained and correct wave speeds are assured.

The superscript ^{Roe} denotes Roe-averaged dependent variables at the cell interfaces which are defined as follows:

$$u_{i+1/2} = \frac{u_i\sqrt{\rho_i} + u_{i+1}\sqrt{\rho_{i+1}}}{\sqrt{\rho_i} + \sqrt{\rho_{i+1}}} \qquad v_{i+1/2} = \frac{v_i\sqrt{\rho_i} + v_{i+1}\sqrt{\rho_{i+1}}}{\sqrt{\rho_i} + \sqrt{\rho_{i+1}}}$$

$$h_{i+1/2} = \frac{h_i\sqrt{\rho_i} + h_{i+1}\sqrt{\rho_{i+1}}}{\sqrt{\rho_i} + \sqrt{\rho_{i+1}}}$$

$$c_{i+1/2} = \left\{(h_{i+1/2} - 1/2(u^2_{i+1/2} + v^2_{i+1/2}))\,(\gamma - 1)\right\}^{1/2} \qquad (36)$$

where the total enthalpy per unit mass is

$$h = (e + p)/\rho \tag{37}$$

The first-order flux $\hat{F}$ on the $j + 1/2$ interface can be obtained in a similar manner by replacing x_η with $-x_\xi$, y_η with $-y_\xi$, and i with j.

3.2.3 Entropy Fix. Chakravarthy and Osher (1985) report that an entropy fix is required with Roe's scheme. In Roe's approximate Riemann solver, weak solutions (solutions with shocks and contact discontinuities) are not uniquely determined by their initial values. An entropy condition is required to determine the physically relevant solutions. The purpose of the entropy fix is to remove expansion shocks and glitches from occurring at sonic rarefactions, such as shown in Figure 11 (Chakravarthy and Osher 1985). Various authors have presented their preferred versions of an entropy fix, however, the version used here is attributed to Harten as reported by Yee (1987). A slight modification of the absolute value of the eigenvalue matrix is performed,

$$|\tilde{\Lambda}| = \begin{cases} |\Lambda| & |\Lambda| - \delta_1 \geq 0 \\ (\Lambda^2 + \delta_1^2)/2\delta_1 & |\Lambda| - \delta_1 < 0 \end{cases} \tag{38}$$

$$\delta_1 = \varepsilon(|U| + c\sqrt{\xi_x^2 + \xi_y^2})$$

and is substituted for $|\Lambda|$ in Eq. 34 and 35. In this study, ε is a constant which is set equal to .10. When $\delta_1 = 0$, the scheme is the least dissipative; the larger the δ_1 , the more dissipative the scheme becomes.

3.3 Second-Order Scheme.

3.3.1 Inviscid Flux. A second-order inviscid flux can be produced by adding a correction term to the first-order flux. However, the second-order correction term causes oscillations in regions of high gradient, for example, in the region of shocks. In order to avoid these instabilities, the correction term must fulfill the criteria for the algorithm to be TVD. TVD schemes achieve second-order accuracy without introducing spurious oscillations near discontinuities by employing a feedback mechanism—"smart numerical dissipation"—wherein fluxes are compared at neighboring control volumes. In regions of little change, no numerical

dissipation is added to the second-order correction terms, while in regions of large change, numerical dissipation is added to ensure stability.

During this process, no new extrema are created by the numerical dissipation. TVD data preserve monotonicity; a) no new extrema must be created and b) the absolute value of any extrema must not increase. TVD schemes yield oscillation-free solutions by modifying flux differences to meet the above criteria. Chakravarthy (1985) outlines a class of explicit flux limiting schemes that fulfill this criteria. The second-order flux for the fully upwind scheme can be written as

$$\hat{E}^{2nd}_{i+1/2} = \hat{E}^{1st}_{i+1/2} + 1/2\left[\Delta\tilde{\hat{E}}^{+}_{i-1/2} - \Delta\tilde{\hat{E}}^{-}_{i+3/2}\right] \tag{39}$$

If the following definitions are made to provide the measure of the change in the right and left running flux, respectively,

$$\begin{aligned} \Delta\sigma^{+}_{i+1/2} &= 1/2\left((\Lambda + |\Lambda|)_{i+1/2} R^{-1}_{i+1/2}\right)\left(\bar{Q}_{i+1} - \bar{Q}_i\right) \\ \Delta\sigma^{-}_{i+1/2} &= 1/2\left((\Lambda - |\Lambda|)_{i+1/2} R^{-1}_{i+1/2}\right)\left(\bar{Q}_{i+1} - \bar{Q}_i\right) \end{aligned} \tag{40}$$

then the TVD limited values of the flux differences can be written as

$$\Delta\tilde{\hat{E}}^{-}_{i+1/2} = R_{i+1/2}\Delta\tilde{\sigma}^{-}_{i+1/2}, \qquad \Delta\tilde{\hat{E}}^{+}_{i+1/2} = R_{i+1/2}\Delta\tilde{\sigma}^{+}_{i+1/2} \tag{41}$$

The symbols ~ and ≈ shown over $\Delta\sigma$ denote flux-limited values and are computed as follows:

$$\Delta\tilde{\sigma}^{-}_{i+1/2} = minmod\left[\Delta\sigma^{-}_{i+1/2},\ \beta\Delta\sigma^{-}_{i-1/2}\right] \tag{42}$$

$$\Delta\tilde{\hat{\sigma}}^{+}_{i+1/2} = minmod\left[\Delta\sigma^{+}_{i+1/2},\ \beta\Delta\sigma^{+}_{i-3/2}\right] \tag{43}$$

where the "minmod" slope-limiter operator is defined as

$$minmod[x,\ y] = sign(x) * max[0,\ min\{|x|,\ y * sign(x)\}] \tag{44}$$

and β is a compression parameter that is restricted to fall in the range

$$1 < \beta \leq 2 \tag{45}$$

The minmod limiter returns the smaller magnitude when the signs are equal, and returns zero when the arguments are of opposite sign. The result is that dissipation is added locally in regions of high flux gradient. At inflection points, the scheme reverts to first-order accuracy.

Eq. 23 can be rewritten with the first-order numerical fluxes, $\hat{E}$ and $\hat{F}$, replaced with the second-order fluxes:

$$\mathcal{V}_{i,j}\frac{\bar{Q}_{i,j}^{n+1}-\bar{Q}_{i,j}^{n}}{\Delta\tau}+\left[\hat{E}_{i+1/2,j}^{2nd}-\hat{E}_{i-1/2,j}^{2nd}+\hat{F}_{i,j+1/2}^{2nd}-\hat{F}_{i,j-1/2}^{2nd}\right]^{n} = \left[\frac{1}{Re}(\hat{S}_{i,j+1/2}-\hat{S}_{i,j-1/2}\right]^{n}. \tag{46}$$

3.3.2 Viscous Flux. A second-order evaluation of the viscous flux terms is obtained by performing a central difference about the corresponding cell interface. The metrics on the cell interface are known quantities and are not included in the averaging. For example, the x-momentum viscous term becomes

$$\frac{1}{2}\left[\left(\frac{\mu}{\mathcal{V}}\right)_{j+1}+\left(\frac{\mu}{\mathcal{V}}\right)_{j}\right]\left[\left((m_1)_{j+1/2}+\frac{1}{3}y_\xi^2\right)(u_{j+1}-u_j)-\frac{1}{3}y_\xi x_\xi(v_{j+1}-v_j)\right]=(\hat{S}_2)_{j+1/2} \tag{47}$$

The y-momentum and energy viscous terms are differenced in a similar fashion. The viscous flux terms are central-differenced in order to obtain a second-order accurate evaluation. It is not clear what effect the present numerical dissipation (due to the inviscid TVD terms) has on the true viscosity terms in the boundary layer region. However, solutions using this algorithm were presented by Molvik (1987) for a steady boundary layer, and a shock-induced boundary layer. The steady boundary layer solution was in excellent agreement with results from an established boundary layer code and the shock-induced boundary layer solution was in excellent agreement with a similarity solution by Mirel.

3.3.3 Temporal Accuracy. The above discussion describes the explicit fully upwind second-order accurate in space scheme. Second-order accuracy in time is achieved by replacing the first-order, backward derivative of the time-dependent variables with a second-order backward difference (Atwood, to be published).

$$C_0Q^{n+1}+C_1Q^{n}+C_2Q^{n-1} \tag{48}$$

where

$$C_0 = \frac{1 - \sigma}{(1 - \sigma)\Delta\tau_2 + \Delta\tau_1}$$

$$C_1 = \frac{\sigma}{(1 - \sigma)\Delta\tau_2 + \Delta\tau_1}$$

$$C_2 = \frac{-1}{(1 - \sigma)\Delta\tau_2 + \Delta\tau_1}$$

$$\sigma = \left(1 + \frac{\Delta\tau_1}{\Delta\tau_2}\right)^2, \quad \Delta\tau_1 = \tau^n - \tau^{n-1}, \quad \Delta\tau_2 = \tau^{n+1} - \tau^n$$

3.4 Implicit Scheme. The advantage of an implicit scheme over an explicit algorithm is increased stability, which allows larger Courant numbers, that is, larger time steps to be taken. This feature is critical to overcome the stiff nature of viscous problems where the disparate length scales can lead to unacceptably small time steps in an explicit algorithm. For a fully implicit scheme, the fluxes must be evaluated at the $n + 1$ time level. The first-order numerical flux on the $i + 1/2$ cell interface evaluated at the $n + 1$ time level, see Eq. 33 through 35 is represented as:

$$\hat{E}^{n+1}_{i+1/2} = \frac{1}{2}\left[E^{n+1}_{i+1} + E^{n+1}_{i} + (A^- - A^+)^{n+1}_{i+1/2}\left(\bar{Q}^{n+1}_{i+1} - \bar{Q}^{n+1}_{i}\right)\right] \tag{49}$$

An approximate linearization of this interface flux may be achieved by freezing the coefficient $(A^- - A^+)$ at time level n and linearizing the remaining terms. Numerical experiments have shown that such an approximation is acceptable (Rai 1984). The linearized numerical flux is then written as:

$$\hat{E}^{n+1}_{i+1/2} = \frac{1}{2}\left[E^n_{i+1} + A^n_{i+1}\Delta\bar{Q}_{i+1} + E^n_i + A^n_i\Delta\bar{Q}_i + (A^- - A^+)^n_{i+1/2}(\bar{Q}^n_{i+1} + \Delta\bar{Q}_{i+1} - \bar{Q}^n_i - \Delta\bar{Q}_i)\right] \tag{50}$$

Reorganizing and using Eq. 49:

$$\hat{E}^{n+1}_{i+1/2} = \frac{1}{2}\left[A^n_{i+1} + (A^- - A^+)^n_{i+1/2}\right]\Delta\bar{Q}_{i+1} + \frac{1}{2}\left[A^n_i - (A^- - A^+)^n_{i+1/2}\right]\Delta\bar{Q}_i + \hat{E}^n_{i+1/2}$$

$$= (A^R)^n_{i+1/2}\Delta\bar{Q}_{i+1} + (A^L)^n_{i+1/2}\Delta\bar{Q}_i + \hat{E}^n_{i+1/2} \tag{51}$$

where

$$\Delta\bar{Q}_i = \bar{Q}^{n+1}_i - \bar{Q}^n_i$$

The linearization of the viscous numerical flux is accomplished by freezing the value of viscosity and linearizing the remaining terms. Since these remaining terms are only a function of the dependent variables in the neighboring cells, the linearization becomes:

$$\hat{S}^{n+1}_{j+1/2} = \hat{S}^{n}_{j+1/2} + \left(\frac{\partial \hat{S}_{j+1/2}}{\partial \bar{Q}_{j+1}}\right)^{n} \Delta\bar{Q}_{j+1} + \left(\frac{\partial \hat{S}_{j+1/2}}{\partial \bar{Q}_{j}}\right)^{n} \Delta\bar{Q}_{j} \qquad (52)$$

$$= \hat{S}^{n}_{j+1/2} + M^{R}_{j+1/2}\Delta\bar{Q}_{j+1} + M^{L}_{j+1/2}\Delta\bar{Q}_{j}$$

In order to compute $\frac{\partial \hat{S}}{\partial Q}$, express S in terms of combinations of the dependent variables in Q, then compute $\left(\frac{\partial S}{\partial q_i}\right)_{i=1,4}$ while holding other q_i constant. For example, using Eq. 47 for $(\hat{s}_2)_{j+1/2}$ as a starting point, let

$$u_{j+1} = \frac{(\rho u)_{j+1}}{\rho_{j+1}} \qquad v_{j+1} = \frac{(\rho v)_{j+1}}{\rho_{j+1}}$$

then

$$9\frac{\partial(\hat{S}_2)_{j+1/2}}{\partial \rho_{j+1}} = \frac{1}{2}\left[\left(\frac{\mu}{\mathcal{V}}\right)_{j+1} + \left(\frac{\mu}{\mathcal{V}}\right)_{j}\right]\left[(m_1)_{j+1/2}\left(\frac{-u}{\rho}\right)_{j+1} - \left\{x_\xi\left(\frac{-v}{\rho}\right)_{j+1} - y_\xi\left(\frac{u}{\rho}\right)_{j+1}\right\}\frac{y_\xi}{3}\right] \qquad (53)$$

The term $\frac{\partial(\hat{s}_2)_{j+1/2}}{\partial_{\rho_j}}$ is identical except the dependent variables are evaluated at j instead of $j+1$. In this fashion, all elements of the matrices M^R and M^L can be computed.

Letting the coefficient matrix be denoted by a B and using a similar type of linearization for the body normal flux, F, as for the streamwise flux, E, the linearized, implicit numerical algorithm is written as:

$$\{\Delta\bar{Q}_{i,j} + \frac{\Delta t}{\mathcal{V}_{i,j}}\left[(A^R)^n_{i+1/2}\Delta\bar{Q}_{i+1,j} + \{(A^L)^n_{i+1/2} - (A^R)^n_{i-1/2}\}\Delta\bar{Q}_{i,j} - (A^L)^n_{i-1/2}\Delta\bar{Q}_{i-1,j}\right]$$

$$+ \frac{\Delta t}{\mathcal{V}_{i,j}}[(B^R - M^R)^n_{j+1/2}\Delta\bar{Q}_{i,j+1} + \{(B^L - M^L)^n_{j+1/2} - (B^R - M^R)^n_{j-1/2}\}\Delta\bar{Q}_{i,j}$$

$$- (B^L - M^L)^n_{j-1/2}\Delta\bar{Q}_{i,j-1}]\}$$

$$= -\frac{\Delta t}{\mathcal{V}_{i,j}}\left[(\hat{E}^n_{i+1/2,j} - \hat{E}^n_{i-1/2,j}) + (\hat{F}^n_{i,j+1/2} - \hat{F}^n_{i,j-1/2} - \frac{1}{Re}(\hat{S}^n_{i,j+1/2} - \hat{S}^n_{i,j-1/2})\right] \quad (54)$$

Notice that the computational stencil in the previous equation involves five grid points: (i, j), $(i, j + 1/2)$, $(i, j - 1/2)$, $(i + 1/2, j)$, $(i - 1/2, j)$. To avoid the expense of inverting a large, sparse pentadiagonal matrix, an approximate factorization is done to break the banded matrix into two tridiagonal matrices. This is written in two steps with the asterisked * variables denoting an intermediate step as:

$$\begin{aligned}\Delta\bar{Q}^*_{i,j} + \frac{\Delta t}{\mathcal{V}_{i,j}}[(A^R)^n_{i+1/2}\Delta\bar{Q}^*_{i+1,j} + \{(A^L)^n_{i+1/2} - (A^R)^n_{i-1/2}\}\Delta\bar{Q}^*_{i,j} - (A^L)^n_{i-1/2}\Delta\bar{Q}^*_{i-1,j}] \\ = -\frac{\Delta t}{\mathcal{V}_{i,j}}[(\hat{E}^n_{i+1/2,j} - \hat{E}_{i-1/2,j}) + (\hat{F}^n_{i,j+1/2} - \hat{F}^n_{i,j-1/2}) - \frac{1}{Re}(\hat{S}^n_{i,j+1/2} - \hat{S}^n_{i,j-1/2})]\end{aligned} \quad (55)$$

Once $\Delta\bar{Q}^*_{i,j}$ is solved for from Eq. 54, it is substituted below and $\Delta\bar{Q}_{i,j}$ is computed.

$$\begin{aligned}\Delta\bar{Q}_{i,j} + \frac{\Delta t}{\mathcal{V}_{i,j}}[(B^R - M^R)^n_{j+1/2}\Delta\bar{Q}_{i,j+1} + \{(B^L - M^L)^n_{j+1/2} - (B^R - M^R)^n_{j-1/2}\}\Delta\bar{Q}_{i,j} \\ - (B^L - M^L)^n_{j-1/2}\Delta\bar{Q}_{i,j-1}] = \Delta\bar{Q}^*_{i,j}\end{aligned} \quad (56)$$

3.5 Iterative Scheme. In order to eliminate the linearization and approximate factorization errors that might occur, a Newton iteration technique is employed. Newton's method finds the zeros of nonlinear equations. For example, to find the value of x such that the scalar function $f(x) = 0$, guess a starting value x^p and iterate as follows:

$$x^{p+1} = x^p - \frac{f(x^p)}{f'(x^p)} \quad (57)$$

Each time x^{p+1} is computed it becomes x^p for the next iteration. Updates of x^{p+1} are computed until very little change in the value of x occurs, then the solution is said to be converged. Another way of writing Eq. 57 by simply rearranging variables is

$$f'(x^p)\left[x^{p+1} - x^p\right] = -f(x^p)\,. \tag{58}$$

The exact same equation holds for a vector function so that

$$f'(\bar{Q}^p)\left[\bar{Q}^{p+1} - \bar{Q}^p\right] = -f(\bar{Q}^p) \tag{59}$$

Now, expanding $f'(\bar{Q}^p)$ and $-f(\bar{Q}^p)$ fully and letting $\Delta\bar{Q}$ be defined as the iterative change in the cell-averaged dependent variables, $(\bar{Q}^{p+1} - \bar{Q}^p)$ instead of the time change, the Newton iterative form for the implicit equations becomes

$$\begin{aligned}\Delta\bar{Q}^{\bullet}_{i,j} + \frac{\Delta t}{\mathcal{V}_{i,j}}\Big[&(A^R)^p_{i+1/2}\Delta\bar{Q}^{\bullet}_{i+1,j} + \{(A^L)^p_{i+1/2} - (A^R)^p_{i-1/2}\}\Delta\bar{Q}^{\bullet}_{i,j} - (A^L)^p_{i-1/2}\Delta\bar{Q}^{\bullet}_{i-1,j}\Big] \\ &= -(\bar{Q}^p_{i,j} - \bar{Q}^n_{i,j}) - \frac{\Delta t}{\mathcal{V}_{i,j}}[(\hat{E}^{2nd}_{i+1/2,j} - \hat{E}^{2nd}_{i-1/2,j}) + (\hat{F}^{2nd}_{i,j+1/2} - \hat{F}^{2nd}_{i,j-1/2}) \\ &\quad - \frac{1}{Re}(\hat{S}_{i,j+1/2} - \hat{S}_{i,j-1/2})]^p\end{aligned} \tag{60}$$

$$\begin{aligned}\Delta\bar{Q}_{i,j} + \frac{\Delta t}{\mathcal{V}_{i,j}}[&(B^R - M^R)^p_{j+1/2}\Delta\bar{Q}_{i,j+1} + \{(B^L - M^L)^p_{j+1/2} - (B^R - M^R)^p_{j-1/2}\}\Delta\bar{Q}_{i,j} \\ &- (B^L - M^L)^p_{j-1/2}\Delta\bar{Q}_{i,j-1}] = \Delta\bar{Q}^{\bullet}_{i,j}\end{aligned} \tag{61}$$

Ideally, the linearization and factorization errors are completely eliminated when the residual of Eq. 61 is driven to zero. Notice that if the residual $\Delta\bar{Q}$ is zero, then $\Delta\bar{Q}^{\bullet}$ is zero, and the left-hand side of Eq. 60 is zero. On the right-hand side, $p = n + 1$, $\bar{Q}^{n+1}$ is converged to an exact solution of the implicit form of the algorithm. However, in this study convergence was defined after four iterations at which time the maximum density residual in the flow solution had decreased by at least an order of magnitude. This definition has been used by this author in previous work with good results and is necessary to reduce the number of iterations and expense of the calculation. Notice that if no subiterations are taken, then Eq. 60 and 61 revert to the implicit, noniterative form presented in the last section.

3.6 Boundary Conditions. The inviscid boundary conditions are obtained by computing a slip boundary condition and specifying an appropriate flux on the walls of the shock tube. At the walls, the normal component of velocity is zero, the tangential component of velocity is nonzero. The flux on these surfaces can then be represented as

$$F = \begin{bmatrix} 0 \\ -y_\xi\, p \\ x_\xi\, p \\ 0 \end{bmatrix} \tag{62}$$

Only a value of pressure need be evaluated at the surface. As a first approximation, one might consider using the pressure of the cell directly above the surface. This translates into a zero-order approximation. However a first-order approximation of the surface flux can be made if a Riemann problem is set up on the surface. This is consistent with the interior scheme and would seem like the reasonable approach. The first-order Riemann solver is used between the first cell off the surface and a reflected cell. If the subscripts 1 and -1 denote the first cell off the surface and the reflected cell respectively, the surface flux can then be written as

$$\hat{F}_s = 1/2\,[F_1 + F_{-1} + (B^- - B^+)_s(\bar{Q}_1 - \bar{Q}_{-1})] \tag{63}$$

The dependent variables of the reflected cell are calculated using the following relations:

$$\begin{aligned} \rho_{-1} &= \rho_1, \qquad p_{-1} = p_1 \\ u_{-1} &= [(x_\xi^2 - y_\xi^2)\,u_1 + 2x_\xi y_\xi v_1]/[x_\xi^2 + y_\xi^2] \\ v_{-1} &= [(y_\xi^2 - x_\xi^2)\,v_1 + 2x_\xi y_\xi u_1]/[x_\xi^2 + y_\xi^2] \end{aligned} \tag{64}$$

The metrics above are those of the cell interface on the surface. A second order flux can be obtained by reflecting even another set of dependent variables with a subscript of -2.

The viscous flux is evaluated on the surface by imposing a no-slip boundary condition, that is, the velocity components are zero at the wall. For the derivatives appearing in the viscous flux at the surface, a second-order accurate difference is used instead of the central differencing used at the interior points.

3.7 Turbulence Modeling. In order to include the effects of turbulence, an eddy viscosity coefficient μ_t is computed. Then, in the stress terms of the laminar Navier-Stokes equations, the molecular coefficient of viscosity μ is replaced by $\mu + \mu_t$. In the heat flux terms, $\frac{\mu}{Pr}$ is replaced by $\frac{\mu}{Pr} + \frac{\mu_t}{Pr_t}$ where Pr_t is taken to be .9 for air. The Baldwin-Lomax algebraic

turbulence model (Baldwin and Lomax 1978) is used in this study to compute values of μ_t. Algebraic refers to the fact that μ_t is obtained from explicit algebraic equations that involve flow properties and empirical parameters. Other turbulence models could have been used to obtain values for μ_t, such as one-equation and two-equation models which require the solution of partial differential equations for the creation and dissipation of turbulent kinetic energy, but with considerably more effort.

The purpose of this study is to discover if turbulence modeling provides the correct trends for better computational/experimental comparisons. If so, then a future effort might be to perform a study of various turbulence models to compare their results and relative cost-effectiveness. However, for a first effort it seemed reasonable to use a simple and computationally inexpensive turbulence model. The Baldwin-Lomax turbulence model is outlined below for completeness.

The Baldwin-Lomax turbulence model defines μ_t in terms of an inner and outer layer in the turbulent boundary layer;

$$\begin{aligned} \mu_t &= (\mu_t)_{inner} \qquad y \le y_{crossover} \\ \mu_t &= (\mu_t)_{outer} \qquad y \ge y_{crossover} \end{aligned} \tag{65}$$

where y is the normal distance from the wall and $y_{crossover}$ is the smallest value of y at which $(\mu_t)_{inner}$ equals $(\mu_t)_{outer}$. The explicit equations for μ_t are

$$(\mu_t)_{inner} = \rho l^2 |\omega| \tag{66}$$

$$(\mu_t)_{outer} = \rho k C_{CP} F_{WAKE} F_{Kleb}(y) \tag{67}$$

where

$$|\omega| = |\frac{\partial u}{\partial y} - \frac{\partial v}{\partial x}|$$

$$l = ky\left[1 - \exp\left(\frac{-y^+}{A^+}\right)\right]$$

$$y^+ = \frac{y\sqrt{\rho_{wall}\tau_{wall}}}{\mu_{wall}} = \frac{\rho_{wall}u_\tau y}{\mu_{wall}}$$

$$A^+ = 26.0, \quad C_{CP} = 1.6, \quad k = .04, \quad K = .0168$$

The only two functions left to be discussed are F_{WAKE} and F_{Kleb} which are related to the function

$$F(y) = y|\omega|\left[1 - \exp\left(\frac{-y^+}{A^+}\right)\right] \tag{68}$$

The function $F(y)$ will have a maximum value, to be denoted F_{max}, at a given normal distance y, to be denoted y_{max} so that F_{WAKE} is taken to be the smaller of

$$y_{MAX} \quad F_{MAX}$$

or

$$y_{MAX} C_{WK} u_{DIF}^2 / F_{MAX} \tag{69}$$

$$\text{where } u_{DIF} = \sqrt{u^2 + v^2} \text{ and } C_{WK} = .25$$

Baldwin and Lomax (1978) report that, near the separation point, the function $F(y)$ develops a double peak and the inner peak is slightly larger. The inner peak occurs at a relatively small value of y_{MAX} such that F_{WAKE} is small and the calculated eddy viscosity is suppressed, causing the predicted separation point to move forward. Their comparisons to experimental data show this turbulence model predicts separation ahead of the experimental separation point by approximately one boundary-layer thickness. For the purpose of this study, the elimination of the need to find the edge of the boundary layer by this model is more significant than the inaccuracy in the prediction of the separation point. Finally, F_{Kleb}, the Klebanoff intermittency factor is given by,

$$F_{Kleb}(y) = \left[1 + 5.5\left(C_{Kleb}\frac{y}{y_{max}}\right)^6\right]^{-1} \tag{70}$$

where $C_{Kleb} = .3$

4. GEOMETRY, GRID, AND INITIAL CONDITIONS

Figure 9 (Reichenback and Opalka 1990) presents the 16° and 45° diverging nozzle configurations that are computationally modeled in this study. The dimensions are presented in millimeters. Notice that the driver section is 30 mm wide, while the driven section (from the throat to the end of the tube) is 40 mm wide. For a truly 2-D geometry, these widths should be equivalent. Because the difference, 10 mm, is not too large, it will be assumed that 3-D effects are not significant and a uniform width of 30 mm is assumed in the computational models. However, area ratios must be equivalent to the original area ratios to simulate shock overpressures correctly. In order to keep the proper area ratios, the diameter of the throat section was enlarged from .016 mm to .0213 mm and the diameter of the driven section (section after the nozzle) was enlarged from .090 mm to .120 mm. The inviscid computational grids with these changes are presented in Figure 12.

The inviscid computational grids contain 214 grid points in the streamwise direction and 30 grid points in the body normal direction. The grids were generated using the GRIDGEN2D code written by Steinbrenner, Chawner, and Fouts (1990). During grid generation, an algebraic solution for the grid is first obtained, then an elliptic solver is applied to smooth the solution and produce grid lines that are nearly orthogonal to the surface boundaries. The viscous grids were generated by replacing the first three grid points (including the point on the surface) with 14 grid points that are exponentially stretched from the surface to the location of the third point in the inviscid grid. The exponential stretching function can be written as

$$s = \Delta s + k\Delta s + k^2\Delta s + \ldots + k^{jmax-2}\Delta s \tag{71}$$

where k = constant to be computed, s = distance between first point and last point involved in exponential stretching (including end points), Δs = spacing between first two grid points and $jmax$ = total number of grid points involved in exponential stretching (including end points), i.e., 14 grid points for the case here. Reorganizing,

$$s - \frac{\Delta s(k^{jmax-1}-1}{k-1} = 0 \qquad (72)$$

Now, Newton's iterative method, described earlier, can be used to solve for a value of k that satisfies Eq. 72.

The two nozzle configurations were simulated at a driver to driven pressure ratio $P_{4/1} = 80$. The driven section was evacuated to $P_1 = 174$ mbar. The temperature of the driver and driven sections were equal at 296 K. The Reynold's number based on conditions behind the primary shock was computed to be 4.65×10^6. Static overpressure was recorded experimentally at a location 370 mm downstream from the diaphragm and on the ceiling of the tube. Computationally, the static overpressure and the dynamic pressure were sampled at three locations which were at the same x location as the experiment. A computational probe was located at the first cell center off of each wall boundary and the third computational probe was located midway between the two walls. The boundaries of the shock tube were solid walls including the end of the driven section.

5. RESULTS AND DISCUSSION

The results have been organized such that the experimental data is presented for the 16° and 45° expansions. Then the inviscid, laminar viscous, and turbulent computational results are presented and compared to the experimental data.

5.1 Experimental Data. Shadowgraphs for the 16° and 45° nozzles at $P_{4/1} = 80$ are shown in Figures 13 and 14, respectively. In order to obtain these figures, two shadowgraphs (one from each optical window) were pieced together; thus, halfway through the nozzle a vertical line is present in some pictures which is not a physical gradient but the overlap of the photographs. In the figures, the primary shock, the contact surface, the recompression shock system, the corner expansion, and diaphragm fragments can be seen. Two important features to notice for the purpose of computational modeling is the turbulent region behind the diffuse contact surface and the separation of the recompression shock system from the lower wall. The purpose of the experiment was to reproduce one-half of the symmetrical flow pattern shown in Figure 5. However, a boundary layer builds up on the lower wall, which

eventually separates from the wall and causes the core flow to seek the center of the half shock tube. These shadowgraphs indicate the need to model viscous and turbulent phenomena in the present computations.

Static overpressure versus time histories are presented in Figures 15a and 15b which were recorded from transducers located 370 mm downstream from the diaphragm location and in the upper wall. A comparison of the experimental data for the two nozzles reveals a similar waveshape up to 500 μs. After this time, the 16° experimental overpressure versus time history reveals a much larger decay in static pressure than the 45° nozzle record. The reason for this difference can be found by examining the shadowgraphs in Figures 13 and 14. A larger decay in the static overpressure is recorded for the 16° nozzle because the recompression shock that develops in this nozzle impinges the upper wall (Figure 13). Thus, the change in static pressure across the recompression shock is recorded by the transducer in the wall at the recording station. However, the recompression shock in the 45° nozzle (Figure 15) does not extend to the wall. Thus, the pressure change across the recompression shock is not recorded. Another point of interest is that the experimental pressure versus time history for the 45° nozzle is noisier (indicative of increased turbulence) than the 16° nozzle history.

5.2 Computational Results. Computationally generated, nondimensional contour plots of density, Mach number, static pressure, and dynamic pressure are presented to aid in visualization of the flow phenomena. Density contour plots will be compared to the experimental shadowgraphs. This is not the best of comparisons because shadowgraphs reflect regions where $\frac{\partial^2 \rho}{\partial x^2} + \frac{\partial^2 \rho}{\partial y^2}$ is significant. However, as reported by this author previously (Molvik 1987), the large gradient regions in the shadowgraphs are typically reproduced in density contour plots. In the same report, it is shown that computational shadowgraph contour plots can be generated but produce superior comparisons only if a very fine computational grid is used throughout. In order to keep run times under five hours, grids too coarse for computational shadowgraphs are used in this study.

For all of the computations performed, plots are presented of static overpressure and dynamic overpressure versus time. In these plots, computational results are provided at the

upper wall, mid-tube and at the lower wall at the same x location as the experimental static pressure probe. Note that the experimental static pressure probe, as stated earlier, is located in the upper wall. Stagnation pressure probes (typically present in blast experiments) could not be utilized in the experiments due to the small size of the tube. Therefore, an experimental dynamic overpressure versus time history which is usually computed from the experimental stagnation and static overpressure data could not be provided. However, computational dynamic overpressure versus time histories are still presented and analyzed.

5.2.1 Inviscid. Figure 16 presents contour plots which occur at 1.45 ms for the 16° nozzle. An examination of these plots confirms trends that hold for moving normal shocks, flow through onverging-diverging ducts, and the properties of oblique and normal shocks. A moving normal shock analysis was performed for the primary shock after it moves into the constant area duct dwnstream of the diverging nozzle. The moving shock analysis, given a shock overpressure, $(P_2 - P_1)$, equal to 400 mbar and $P_1 = 174$ mbar results in the following values:

$$\frac{P_2}{P_1} = 3.3, \quad M_2 = .633, \quad \frac{\rho_2}{\rho_1} = 2.247,$$

which agrees with the contour data.

The flow through the converging-diverging nozzle is choked and subsequently expands to a high supersonic, low pressure, and density conditions in the diverging nozzle. The flow adjusts to the higher pressure downstream of the exit of the nozzle and behind the primary shock by forming a recompression shock system. The recompression shock system is composed of a normal shock near the lower wall and an oblique shock near the upper wall. At a much later time of 4.87 ms, Figure 17 shows the primary shock which has reflected from the right closed end and is interacting with the front of the complex field of reflected oblique shocks. Gradients in total enthalpy are caused by the unsteady temporal nature of the primary shock. Gradients in entropy occur when some streamlines experience a higher entropy increase by going through the recompression shock system at angles close to normal while other streamlines experience a lower entropy increase by going through the recompression shock system at angles that are more oblique. From Crocco's theorem,

$$T\nabla s = \nabla h - V x(\nabla x V) + \frac{\partial V}{\partial t} \qquad (73)$$

where T is temperature, s is entropy, h is total enthalpy, V is velocity and t is time, it is known that whenever gradients in total enthalpy or gradients in entropy exist in the flow field, rotational motion occurs.

The shocks in the recompression shock system repeatedly reflect from the walls. These reflections set up a shock diamond pattern that stretches many diameters downstream without weakening in an inviscid code. The contour data compares well with trends from inviscid theory, however, the experimental shadowgraphs in Figure 13 show some separation of the flow from the walls. Thus, the modeling of viscous and turbulent phenomena must be pursued to improve the comparisons.

Figures 18a and 18b present inviscid computational static overpressure and dynamic pressure versus time histories, respectively, at three radial locations for the 16° nozzle. The static overpressure versus time plot reveals the computational primary shock is smeared compared to the experimental record. This is due to the coarseness of the grid used in the computation. The shock overpressure level at the wall compares well to the shock overpressure level recorded in the experiment. The overpressure level behind the primary shock compares reasonably well to the experiment, but the decrease in pressure at 500 μs, caused by the influence of the recompression shock does not compare accurately. This discrepancy is similar in nature to the computational/experimental comparison shown in Figure 8.

The dynamic pressure ($\frac{\gamma}{2} M^2 P_{static}$) plot shows a jump in dynamic pressure after the arrival of the initial shock to approximately 250 mbar. This is consistent with the increase in Mach number and static pressure across the moving shock. After the arrival of the contact surface, the dynamic pressure jumps to above 1,200 mbar. Although the pressure is constant across the contact surface, the Mach number increases which accounts for the increase in dynamic pressure.

Figures 19 and 20 present similar plots for the 45° nozzle. The significant difference between the 16° and the 45° case is the different angles the recompression shock system makes with the walls of the shock tube and the increased radial complexity of the flow for the 45° nozzle. The density contour data in Figure 19 at .92 ms contains the same gross flow features as shown in the shadowgraphs in Figure 14. However, the computation does not reproduce the regions of separation which are present in the shadowgraphs. Ideally, the addition of the viscous terms to the computations should improve the shadowgraph comparison without degrading the static overpressure history comparison. The inviscid static overpressure versus time history in Figure 20 compares reasonably well to the experimental data at the upper wall. The computational static overpressure at mid-tube is similar to the upper wall record, but the lower wall computational record experiences a large pressure decrease similar to the 16° nozzle case. This is due to the fact that the recompression shock system near the lower wall is swept past the x station where data is computationally sampled. The dynamic pressure record shows histories that are dissimilar for all three locations. This is an indication of the varying strength of the recompression shock system in the radial direction. A recommendation for future experimental work is to sample data at various y locations in order to assist validation of the radial complexity of the flow.

5.2.2 Laminar Viscous and Turbulence. In this section, computational results are presented which show the effect of adding the laminar viscous terms and implementing a no-slip boundary condition at the lower and upper wall. Also, results are presented for two different implementations of the Baldwin-Lomax turbulence model. One implementation is where the Baldwin-Lomax turbulence model is referenced relative to a laminar viscous bottom boundary condition and a slip condition is assumed at the upper wall. This case is denoted by "LV and TUR Bot" in the text and in the figures. Also, results are shown for the Baldwin-Lomax turbulence model referenced relative to a laminar viscous upper boundary with a slip condition assumed at the bottom boundary. This case is denoted by "LV and TUR Top." More rigorous computations were attempted which made both boundaries no-slip simultaneously. The influence of the two walls on the turbulent eddy viscosity was computed using an inverse averaging procedure (Goldberg and Chakravarthy 1988) where

$$\mu_t = \frac{(\mu_t/n)_1 + (\mu_t/n)_2}{(1/n_1^2 + 1/n_2^2)^{\frac{1}{2}}} \tag{74}$$

and the indices 1 and 2 refer to the two walls and n refers to the coordinate locally normal to the wall. However, these computations aborted in the subroutine which computes the time step $\Delta\tau$ from the Courant Friedrichs Lewey (CFL) stability condition. The CFL condition requires the $\Delta\tau$ must be less than or equal to the time required for a sound wave to propagate between two adjacent grid points. Efforts to determine the exact cause of the instability which occured in the CFL condition were unsuccessful, but are still thought to be an inaccuracy in the numerical implementation and not because of a physical limitation.

Figure 21 presents the laminar viscous contour plots at 1.6 ms for the 16° nozzle case. The geometry of the recompression shock system has changed from the inviscid solution. The system is separating from the bottom surface which is confirmed in the velocity vector plot in Figure 22. Figure 23 presents the contour data that results at 2.1 ms when a "LV and TUR Bot" implementation of the Baldwin-Lomax turbulence model is used for the 16° nozzle. The contours near the lower wall are similar to the laminar viscous solution, however, the gradient clusterings near the lower boundary are more smeared. This trend is in agreement with the idea that turbulence acts as an additional mechanism for diffusing energy in the flowfield. Figure 24 presents the contour data that results at 2.0 ms when a "LV and TUR Top" implementation is used. The contours near the slip condition are more like the inviscid solution and the contours near the top boundary (no-slip condition) are similar to the laminar viscous contours except more smeared.

Figures 25–27 present comparisons of the inviscid, laminar viscous, and turbulent static overpressure histories for probes located at the upper wall, the lower wall, and mid-tube, respectively. Comparison of the inviscid, laminar viscous, and turbulent static overpressure versus time histories in these figures reveals some differences. Two cases, the laminar viscous and "LV and TUR Top," static overpressure histories at the upper wall location, Figure 25, have increases in static overpressure at approximately 900 μs. This increase appears to be caused by a small region of separated flow in the corner of the diverging nozzle where it attaches to the driven section. Other than this difference at 900 μs, the comparisons

of the inviscid, laminar viscous, and turbulent static overpressure histories at the upper wall are virtually the same.

The "LV and TUR Bot" static overpressure at the lower wall, Figure 26, has a more slowly decaying waveshape than the other three solutions. Also, this decaying waveshape is not evident in the mid-tube or upper wall histories. Thus, it can be concluded that the effects of the Baldwin-Lomax turbulence model are being confined to a region close to the no-slip wall condition from which it is implemented. The mid-tube comparisons of static overpressure Figure 27, reveals slight differences which indicates the computational viscous terms are not significant to the mid-tube flow conditions.

Comparison of the dynamic pressure histories (Figures 28–30) confirms the correct implementation of the boundary conditions. The upper wall, Figure 28, and lower wall, Figure 29, comparisons show the laminar viscous dynamic pressure jumps to approximately 150 and 75 mbar, respectively, and then decays to zero. The wall solutions are computationally sampled at the first cell center from the wall surface, therefore, the Mach number or velocity for the laminar viscous solution is not exactly zero but is very small, as it should be for a no-slip boundary condition. The "LV and TUR Bot" implementation of the turbulence model produces a dynamic pressure record at the upper wall, Figure 28, which is very close to the inviscid solution. This is reasonable since this implementation of the turbulence model uses a slip boundary condition at the upper wall. The "LV and TUR Top" case produces a dynamic pressure record similar to the laminar viscous solution which is in agreement with the no-slip boundary condition used by this case at the upper wall. At the lower wall, Figure 29, the trends are reversed from the upper wall dynamic pressure description. The mid-tube laminar viscous and turbulent dynamic pressure histories, Figure 30, appear unchanged from the inviscid solution. The next sections examine similar contour plots and overpressure histories for the 45° nozzle.

The 45° laminar viscous nozzle contour plot at 1.1 ms, Figure 31, also shows improved agreement with the shadowgraphs. In addition to the separation of the flow along the lower wall, a region of separation and reverse flow appears in the corner as the flow tries to negotiate the 45° expansion. These regions of separation and reverse flow can be more

clearly seen in the velocity vectors plot, Figure 32. Figure 33 presents the contour data that results at 1.1 ms when a "LV and TUR Bot" implementation of the turbulence model is used for the 45° nozzle. Similar to the 16° nozzle, the contours near the lower wall are a little more smeared. Figure 34 presents the contour data that results at 1.1 ms when a "LV and TUR Top" implementation of the turbulence model is used. Again, similar to the 16° nozzle results, the contours near the no-slip boundary become smeared.

With laminar viscous terms or turbulence on, the static overpressure comparisons at the upper wall, Figure 35, are still similar to the inviscid solution. The inviscid solution appears to provide the best comparison to the experimental data recorded at the upper wall. However, recall that the inviscid solution provides the worst comparison of computational density contour data to shadowgraphs. The comparisons of static overpressure histories at the lower wall, Figure 36, show that the "LV and TUR Bot" static overpressure versus time history is significantly different from the "LV and TUR Top" case, the laminar viscous case, and the inviscid solution. At the mid-tube location, Figure 37, the "LV and TUR Bot" solution is reasonably similar to the inviscid solution, and the laminar viscous solution and "LV and TUR Top" solutions are reasonably similar. Recall that the 16° nozzle mid-tube comparisons were practically identical for all four cases. Thus, the 45° nozzle results show that computationally adding viscous effects alters the recompression shock system such that significantly different pressure versus time histories can result between the inviscid, laminar viscous, and turbulent solutions.

Comparison of the upper and lower wall dynamic pressure histories, Figures 38 and 39, again confirms the correct numerical implementation of the boundary conditions, similar to the 16° nozzle discussion. At the mid-tube location, Figure 40, the "LV and TUR Bot" case and the inviscid solutions are similar but different from the laminar viscous and "LV and TUR Top" solutions. Again, it can be concluded that significantly different results are obtained for the 45° nozzle case depending on how viscous effects are included and at what radial location the flow is sampled.

Finally, Figure 41 presents in one figure the 16° nozzle density contour plots for the inviscid, laminar viscous, and turbulent solutions. Figure 42 presents the velocity vector plots

for the four computational cases. Figures 43 and 44 present similar results for the 45° nozzle. These plots help to further visualize the differences between the inviscid, laminar viscous, and turbulent solutions previously described. Of particular note is the regions of separation in the viscous solutions which are not present in the inviscid solutions. Also the slip and no-slip boundaries are clearly evident in the velocity vectors plot.

6. CONCLUSIONS

A 2-D computational study of the flow patterns that develop in unsteady, overexpanded divergent nozzles with comparison to experimental data was performed and analyzed for two nozzle angles (16° and 45°). Experimental shadowgraphs indicated viscous effects were present. Therefore, the addition of thin layer laminar viscous terms was investigated as well as using the Baldwin-Lomax turbulence model in the computational simulations.

The thin-shear layer approximation improved the comparison of density contour data to shadowgraph pictures over the inviscid computations for both nozzle configurations. The laminar viscous computations produced regions of separation in the corner of the diverging nozzles and along the lower boundary which were qualitatively in good agreement with the shadowgraphs. Turning on the turbulence model relative to one wall or the other had the effect of smearing the contours.

The laminar viscous solution for the 16° nozzle did not significantly alter the inviscid static overpressure solutions. The effect of turning on the turbulence model relative to the lower wall was to alter the static overpressure near the lower wall for the 16° nozzle to a slightly more decaying waveshape. This effect was not noticeable at the mid-tube or upper wall locations, even when the turbulence model was turned on relative to the upper wall. Thus, it was concuded that the turbulence model did not significantly affect the flow for the 16° nozzle configuration.

For the 45° nozzle, the effect of including the laminar viscous terms or the turbulence model relative to the upper or lower wall was to produce significantly different waveshapes from the inviscid solution particularly at the mid-tube and lower wall locations. The

experimental static overpressure versus time histories recorded at the upper wall of the 16° and 45° nozzle configurations were simulated equally well by the inviscid, laminar viscous, and turbulent solutions at the upper wall. However, the computational addition of viscous effects were very important for good comparisons of shadowgraphs and computational contour plots. Moreover, it is concluded from the comparison of shadowgraphs and contour data that the flow physics in the diverging nozzles was best captured by the laminar viscous computations.

The BLAST2D code can be used as a design tool and as a complement to the experimental database that will be obtained with the LB/TS facility. In order to improve the computational modeling of viscous effects in the code, it is recommended that future experimental work provide flowfield conditions at various radial locations and the same x location. Thus, verification or improvement of computational predictions of radial complexity in the flow can be further explored. Future computational work of interest is the coding of various turbulence models in addition to the Baldwin-Lomax algebraic turbulence model used here to determine which is the most suited to diverging nozzle flow.

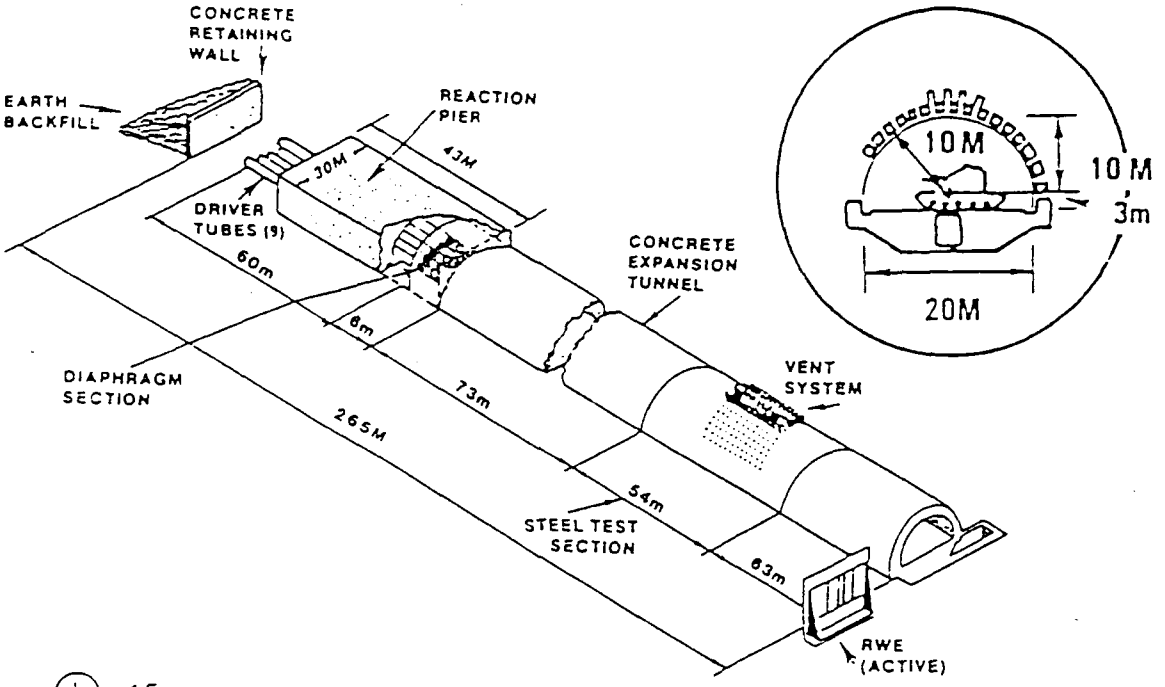

(a) Layout of U.S. Facility

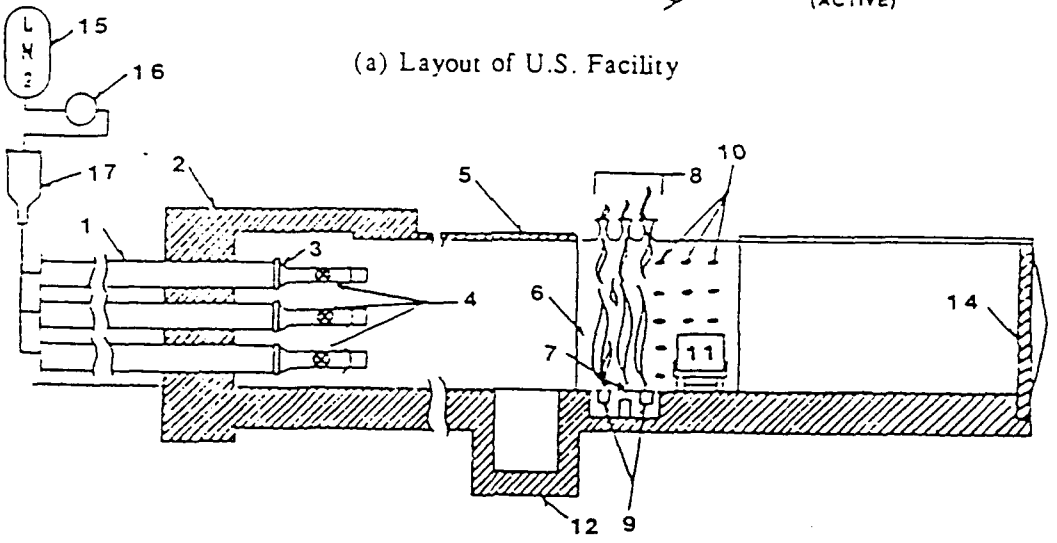

LEGEND

1 - Steel Driver Tubes	9 - Air Curtain Plenum
2 - Concrete Reaction Pier	10 - Instrumentation and Light Ports
3 - Converging Nozzles	11 - Test Target
4 - Throat Valves and Diaphragms	12 - Soil Tank
5 - Concrete Expansion Tunnel	14 - Rarefaction Wave Eliminator
6 - Steel Test Section	15 - Liquid Nitrogen Storage
7 - Thermal Radiation Sources	16 - Cryogenic Pumps
8 - Combustion Products Ejectors	17 - Pebble-Bed Superheaters

(b) The LB/TS Concept

Figure 1. Proposed U.S. Large Blast/Thermal Simulator.

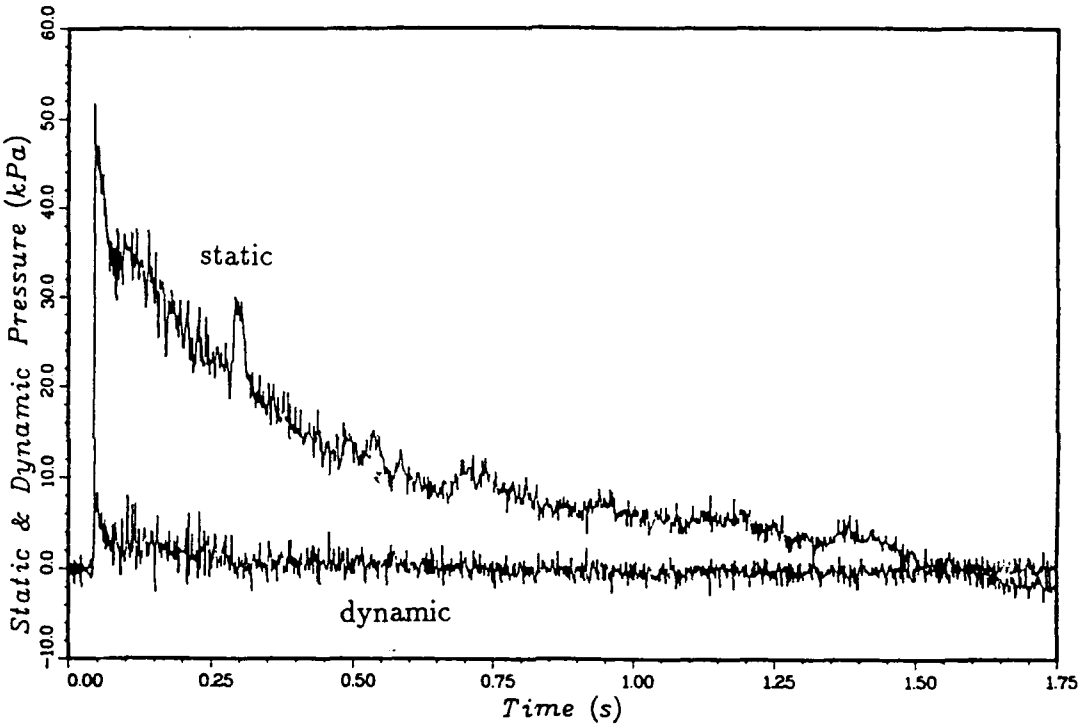

Figure 2. Typical Experimental Static and Dynamic Overpressure Waveform From a Blast Simulator in France.

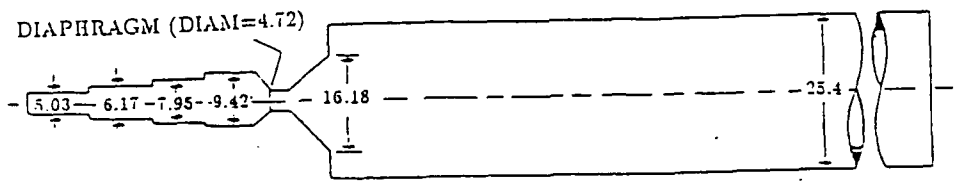

a.

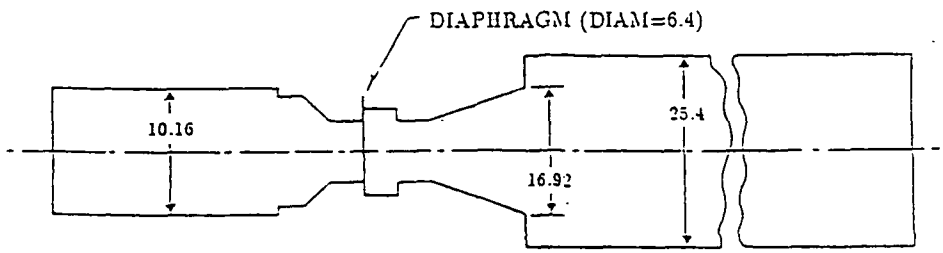

b.

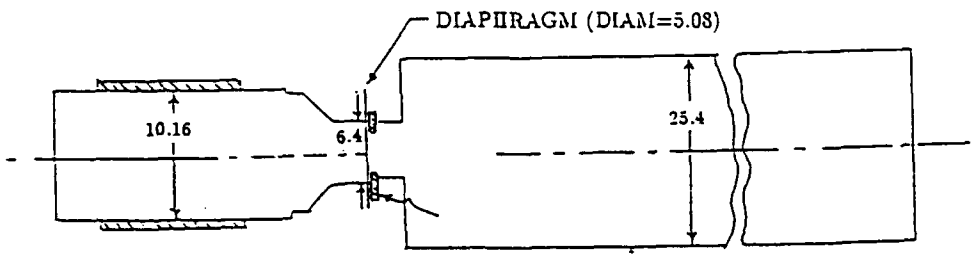

c.

Figure 3. 1/57 Scale Two-Dimensional Axisymmetric Shock Tubes, Experimental Tools for LB/TS Design Studies.

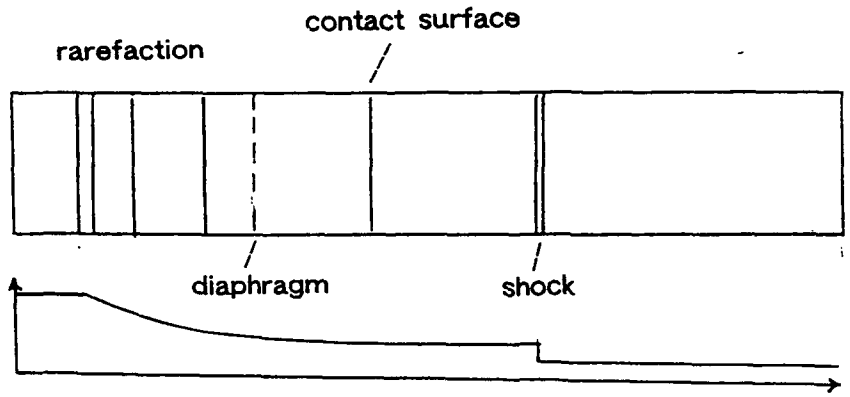

a.

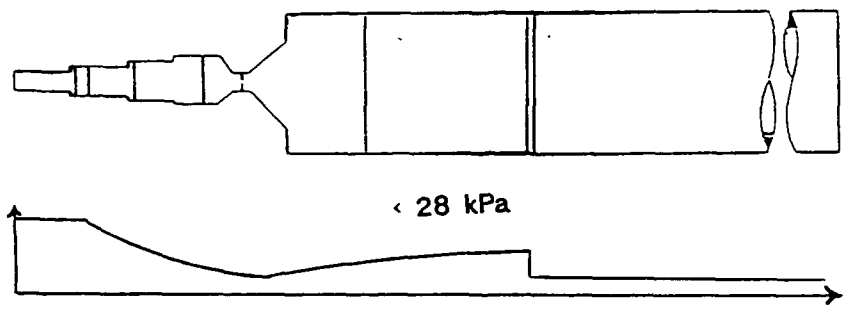

b.

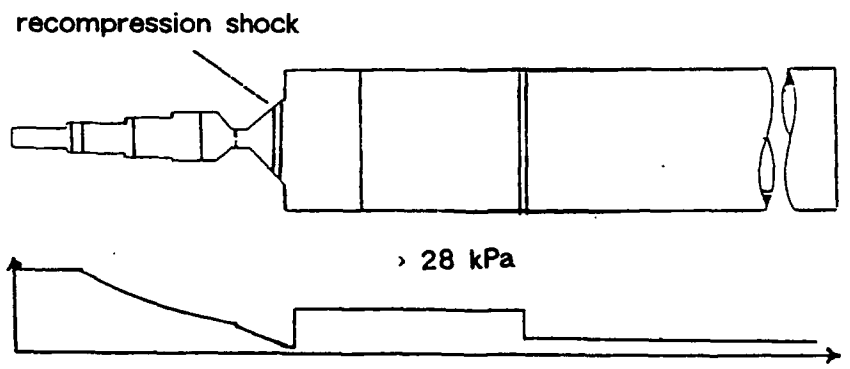

c.

Figure 4. Typical Flow Patterns for Quasi-One-Dimensional LB/TS Geometry Compared to Straight Shock Tube.

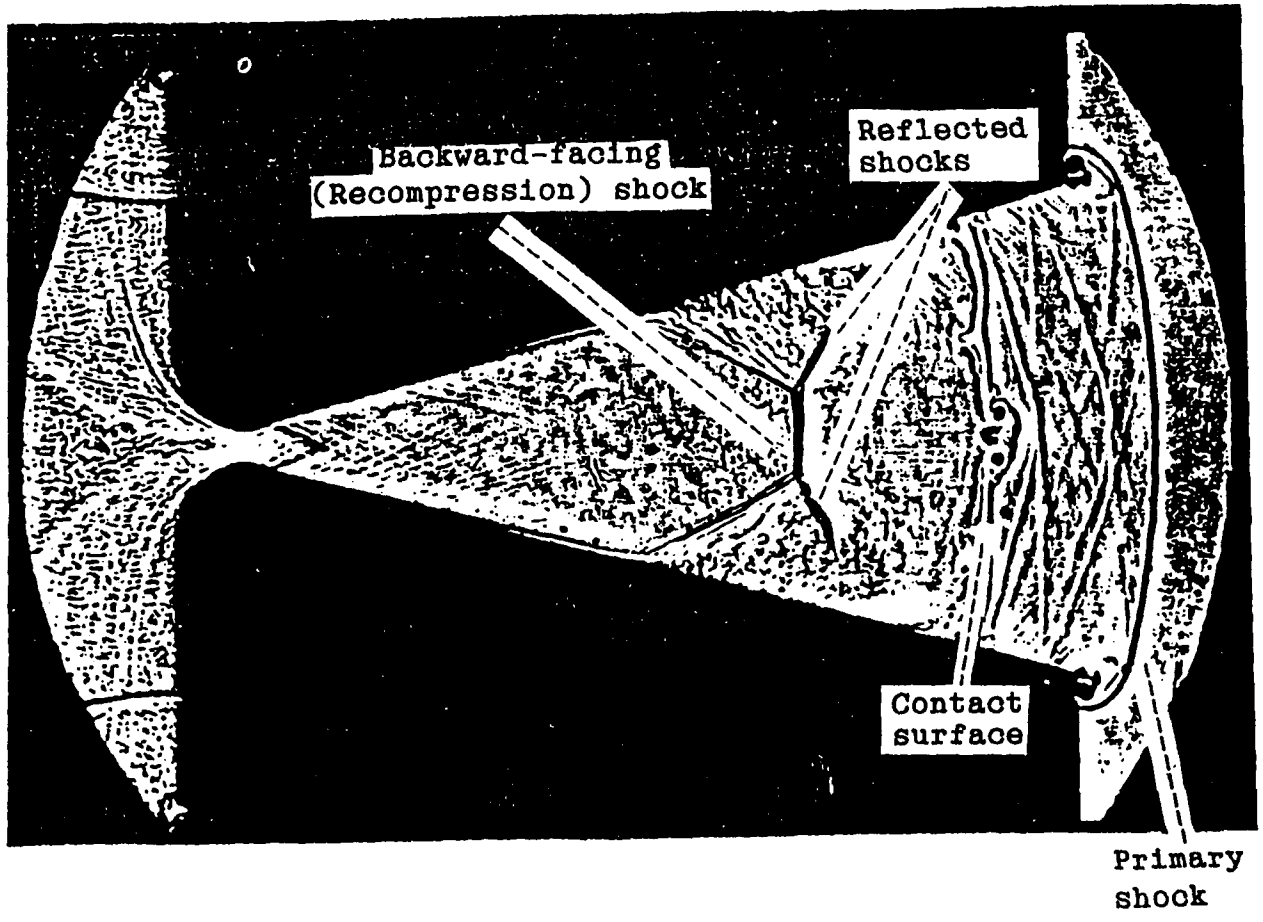

Figure 5. Shadowgraph of Primary Shock, Contact, and Recompression Shock in Diverging Nozzle, Amann (1990).

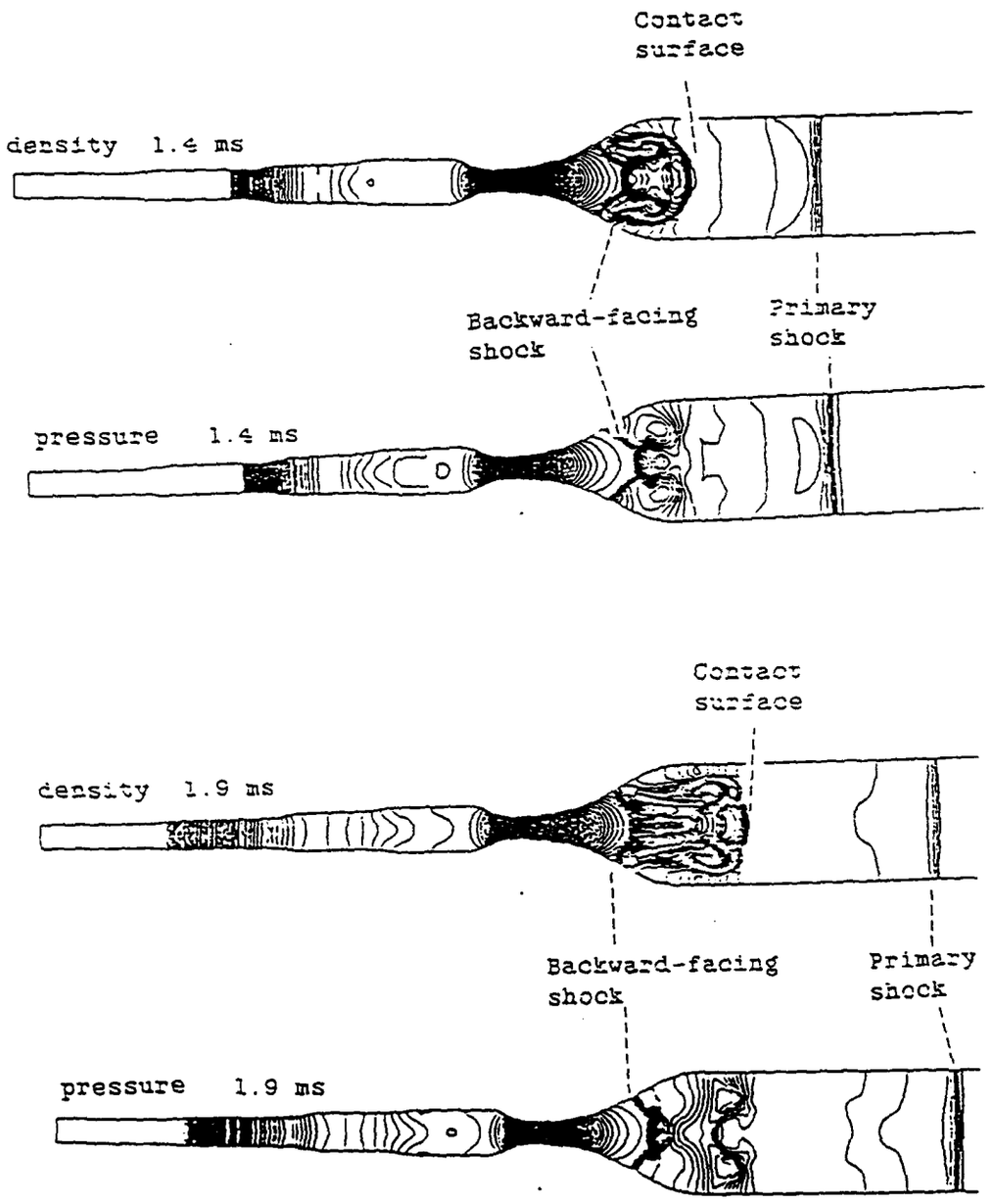

Figure 6. Computational Density and Pressure Contour Plots of Recompression Shock System in Diverging Nozzle.

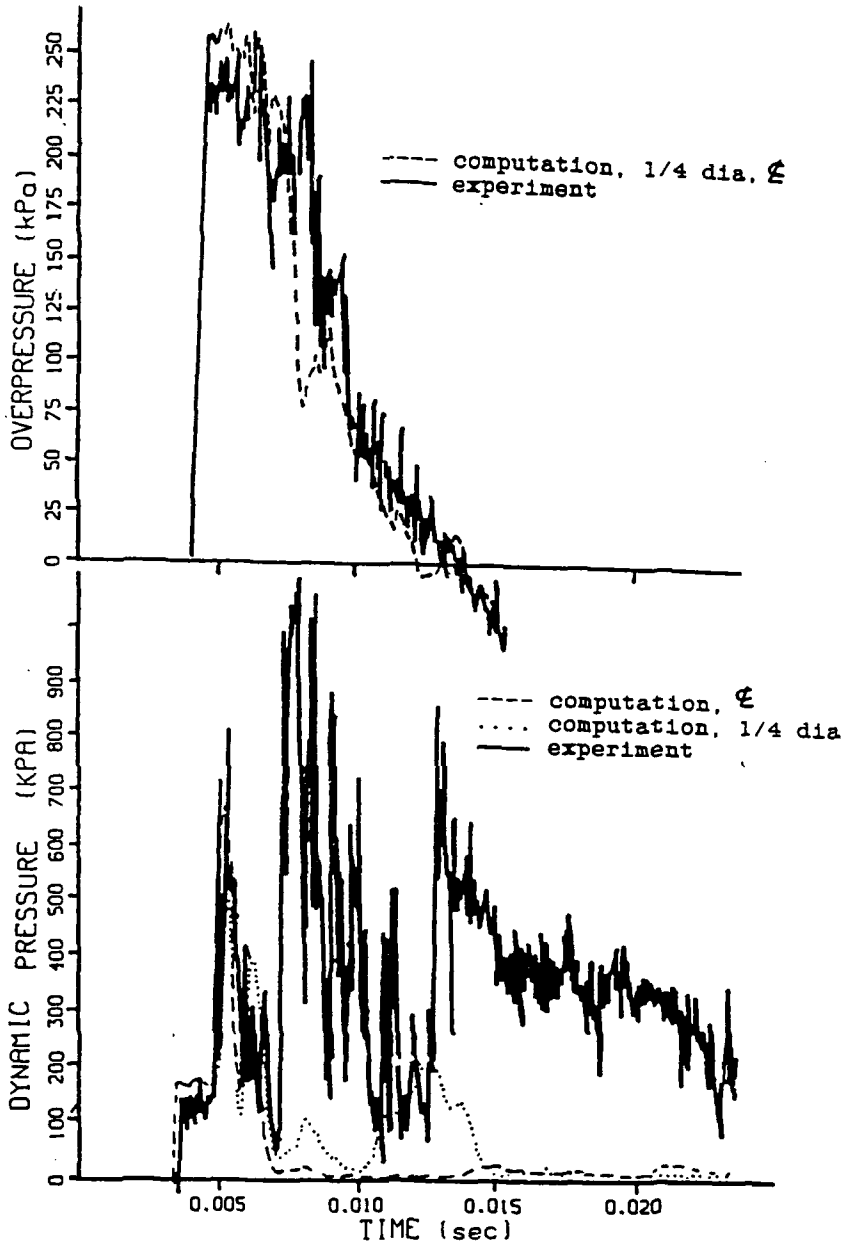

Figure 7. Computational (Inviscid) and Experimental Comparison of Static and Dynamic Pressure for Two-Dimensional Axisymmetric Shock Tube, Figure 3a.

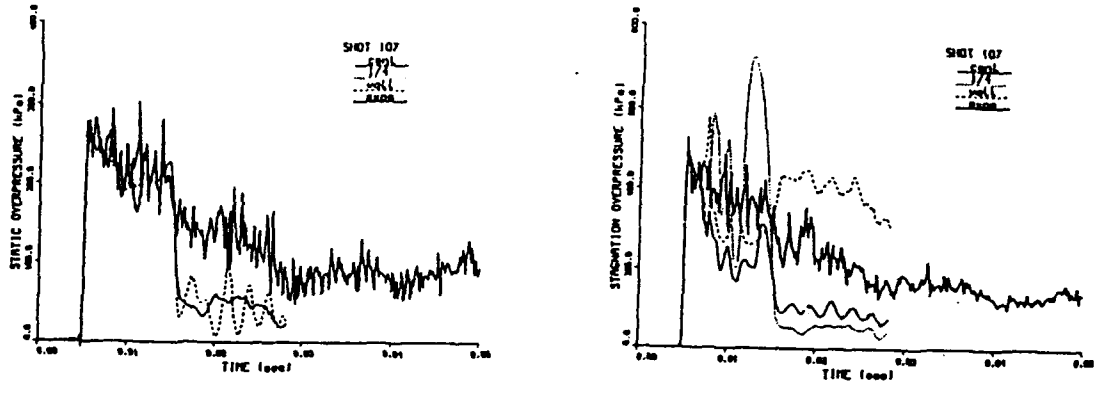

Figure 3b

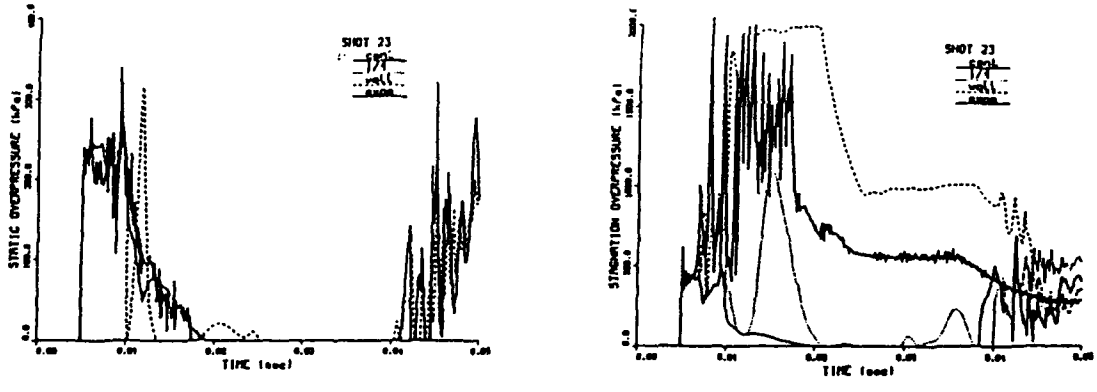

Figure 3c

Figure 8. Computational (Inviscid) and Experimental Comparison of Static and Stagnation Pressure for Two-Dimensional Axisymmetric Shock Tube, Figures 3b and 3c.

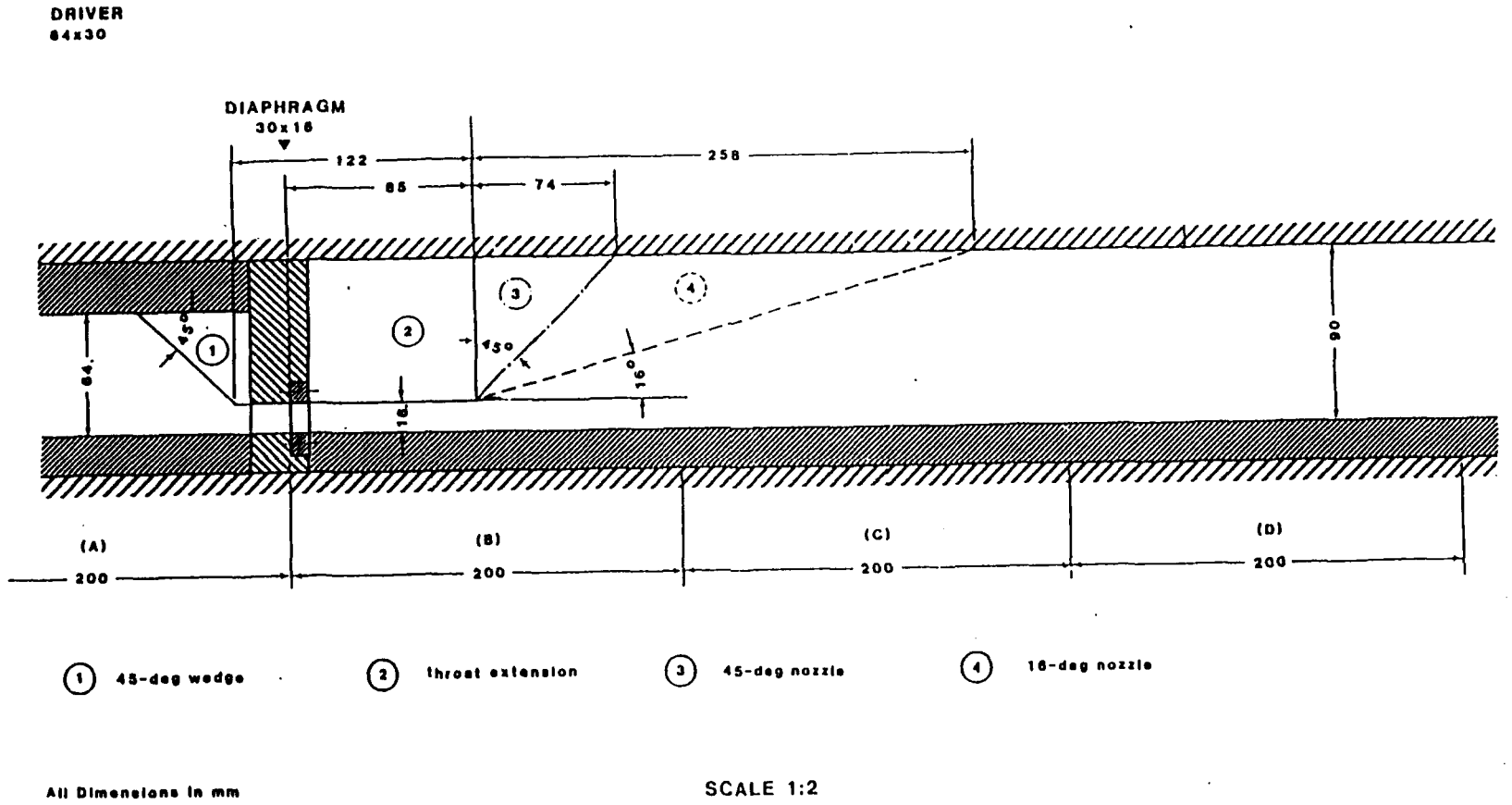

Figure 9. Two-Dimensional Planar 16° and 45°-Nozzle Configurations.

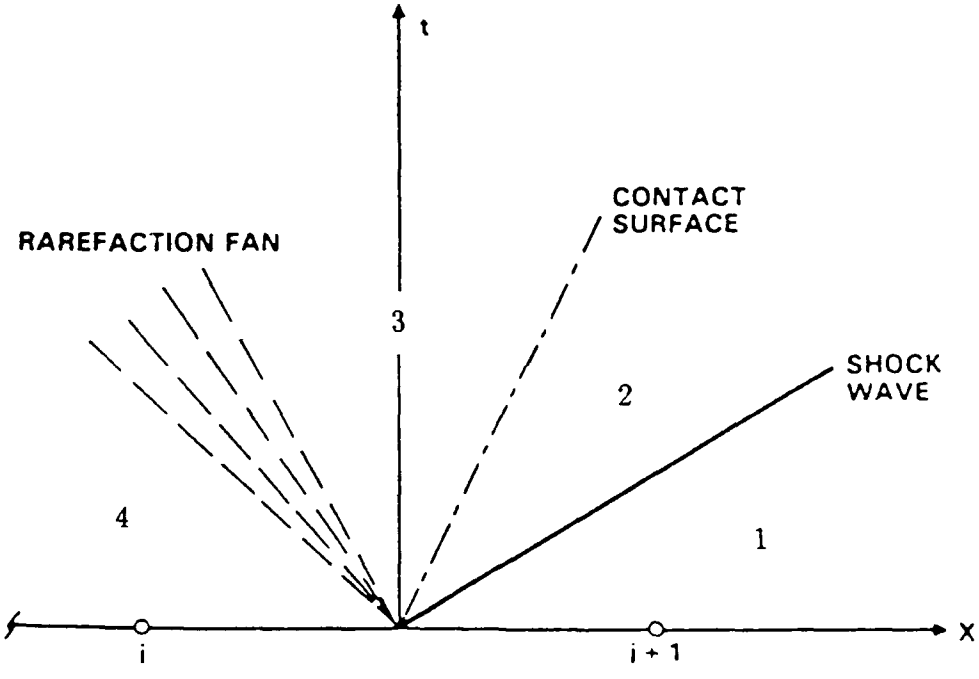

Figure 10. One-Dimensional Riemann Problem.

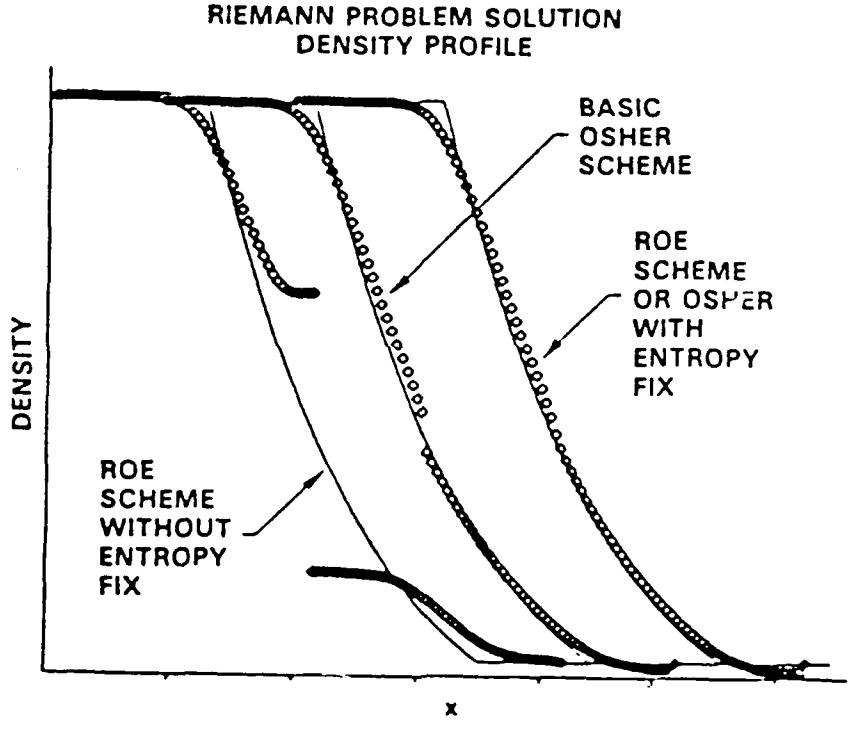

Figure 11. Expansion Shocks, "Glitches," and Entropy Fix.

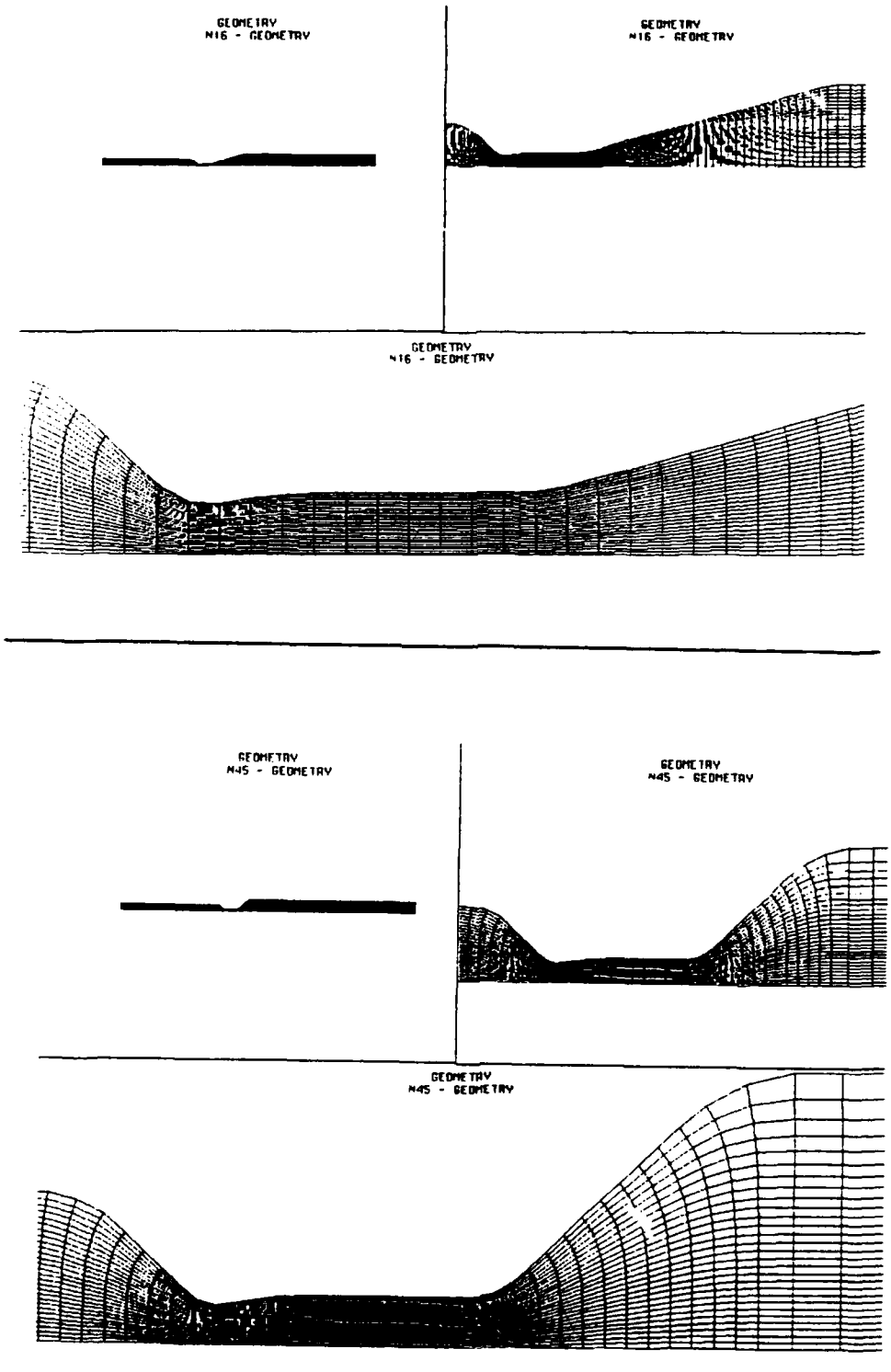

Figure 12. Inviscid Computational Grids.

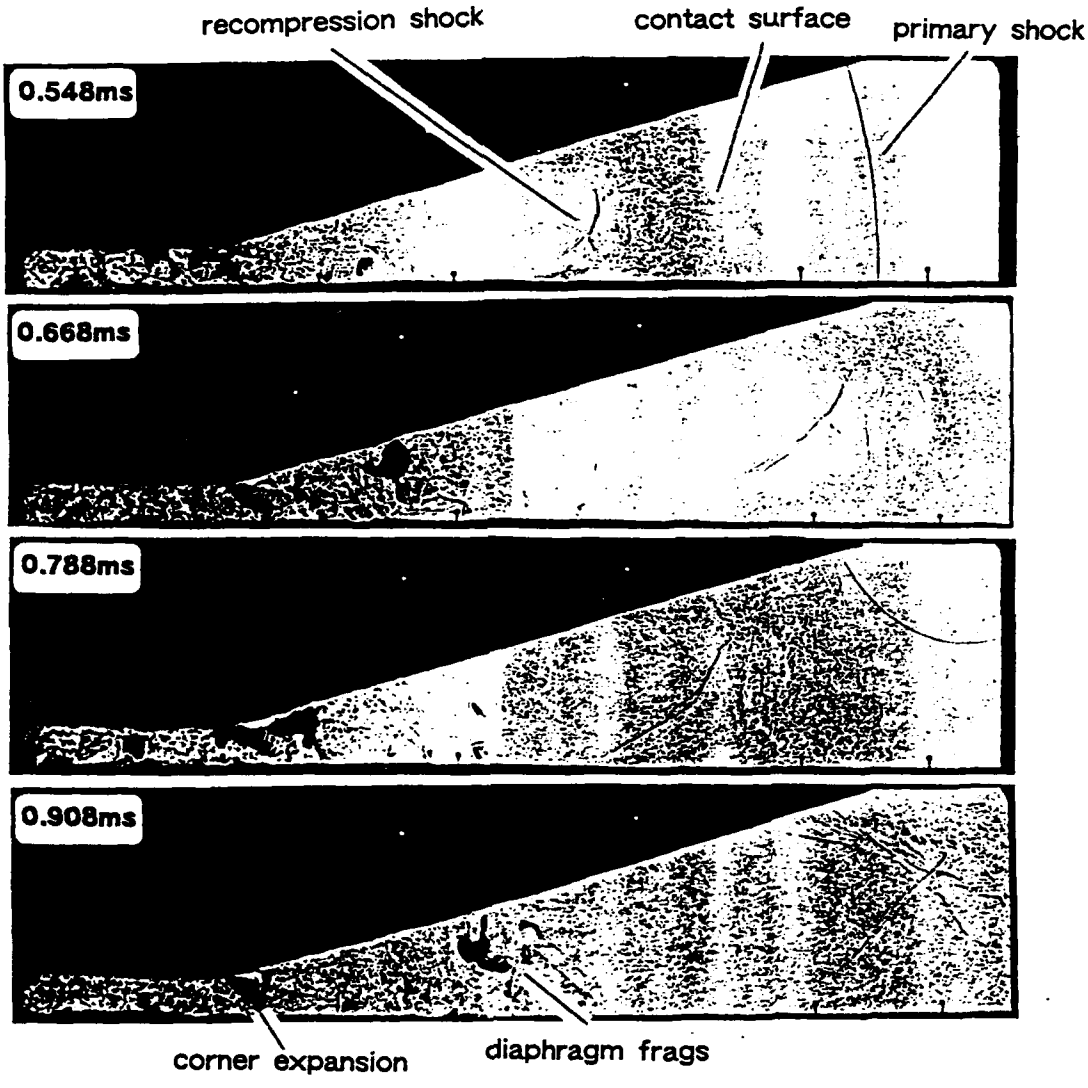

Figure 13. 16° Nozzle Shadowgraph.

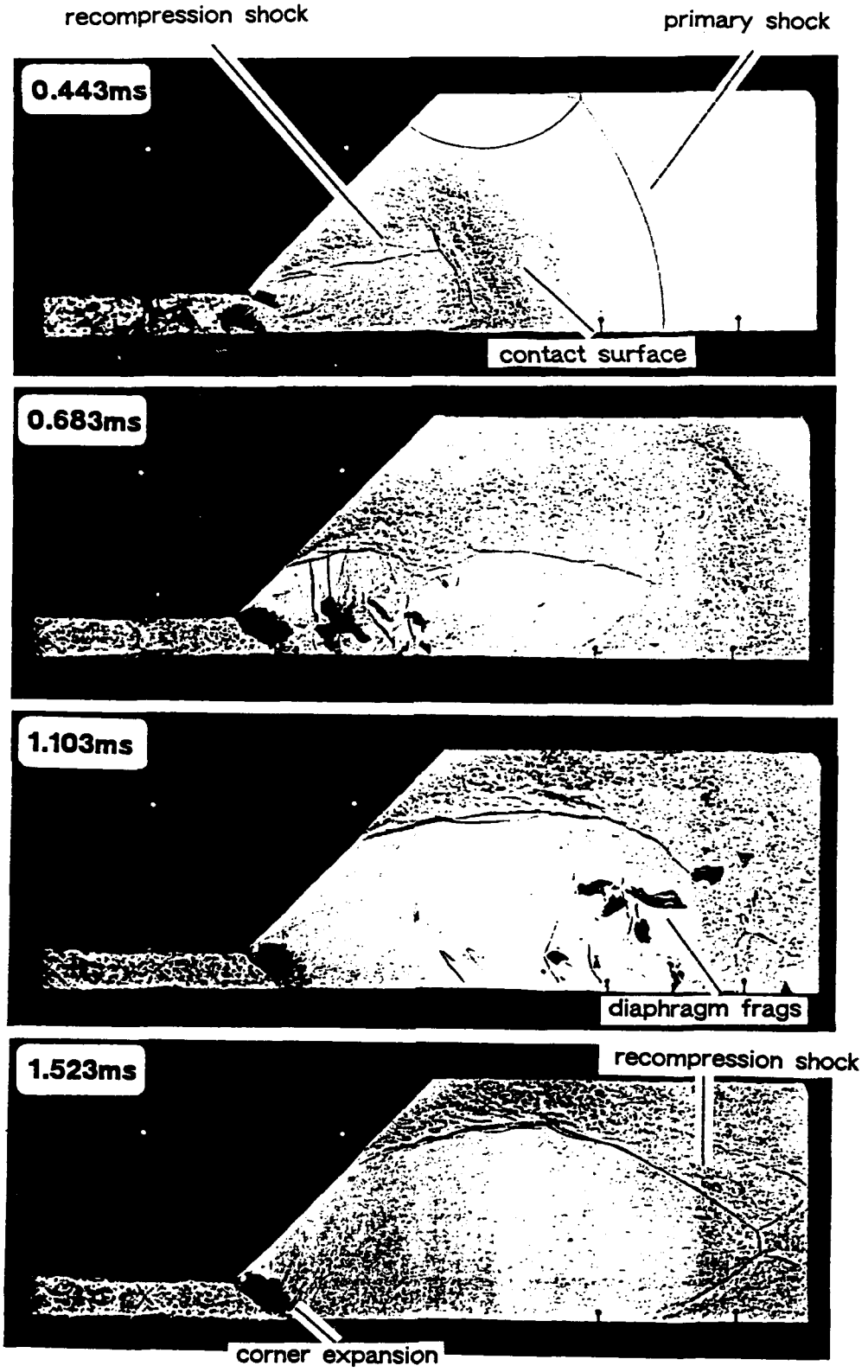

Figure 14. 45° Nozzle Shadowgraph.

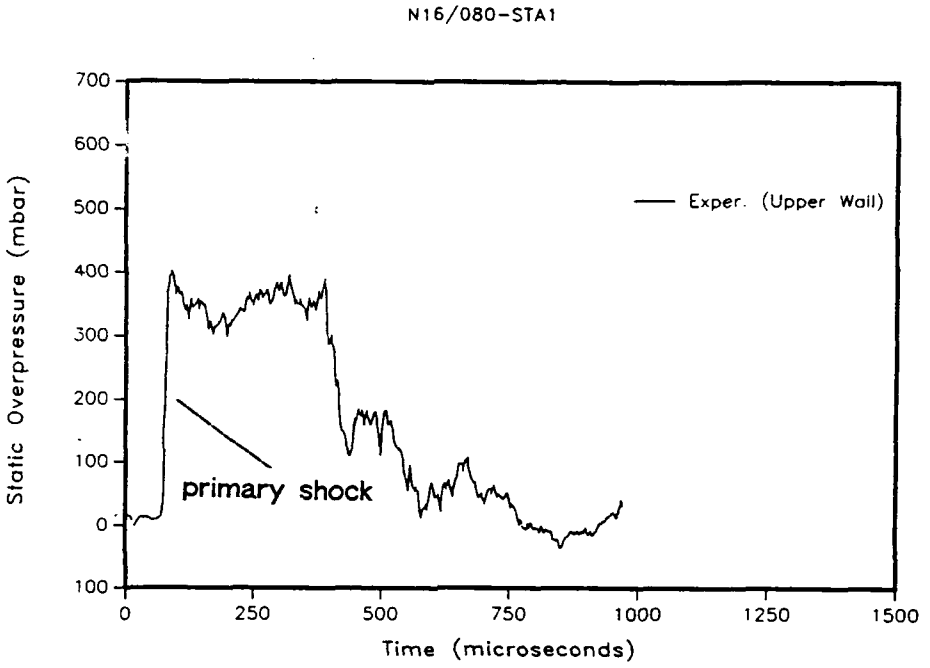

Figure 15a. Experimental Static Overpressure vs. Time–16° Nozzle.

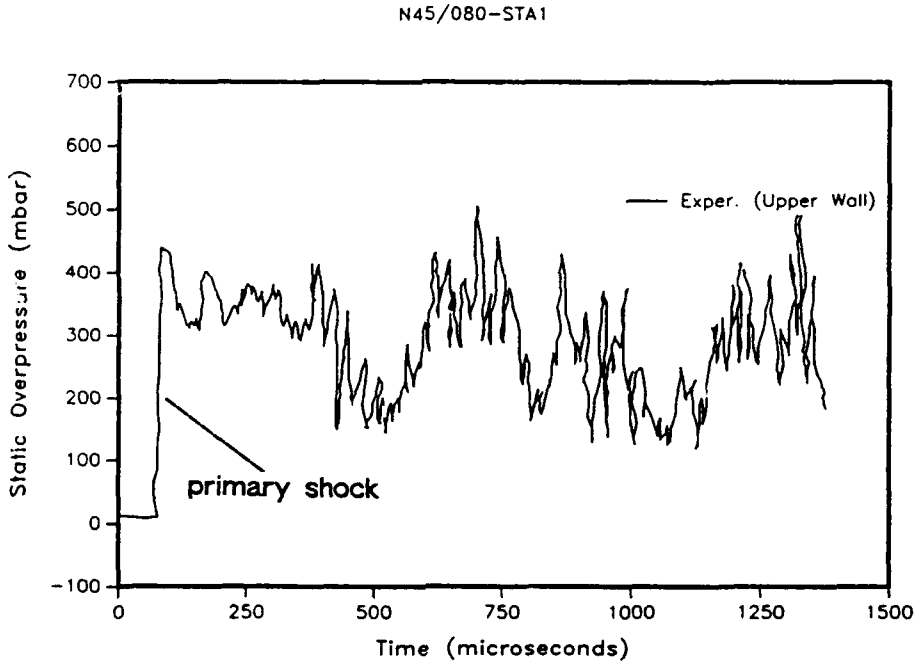

Figure 15b. Experimental Static Overpressure vs. Time–45° Nozzle.

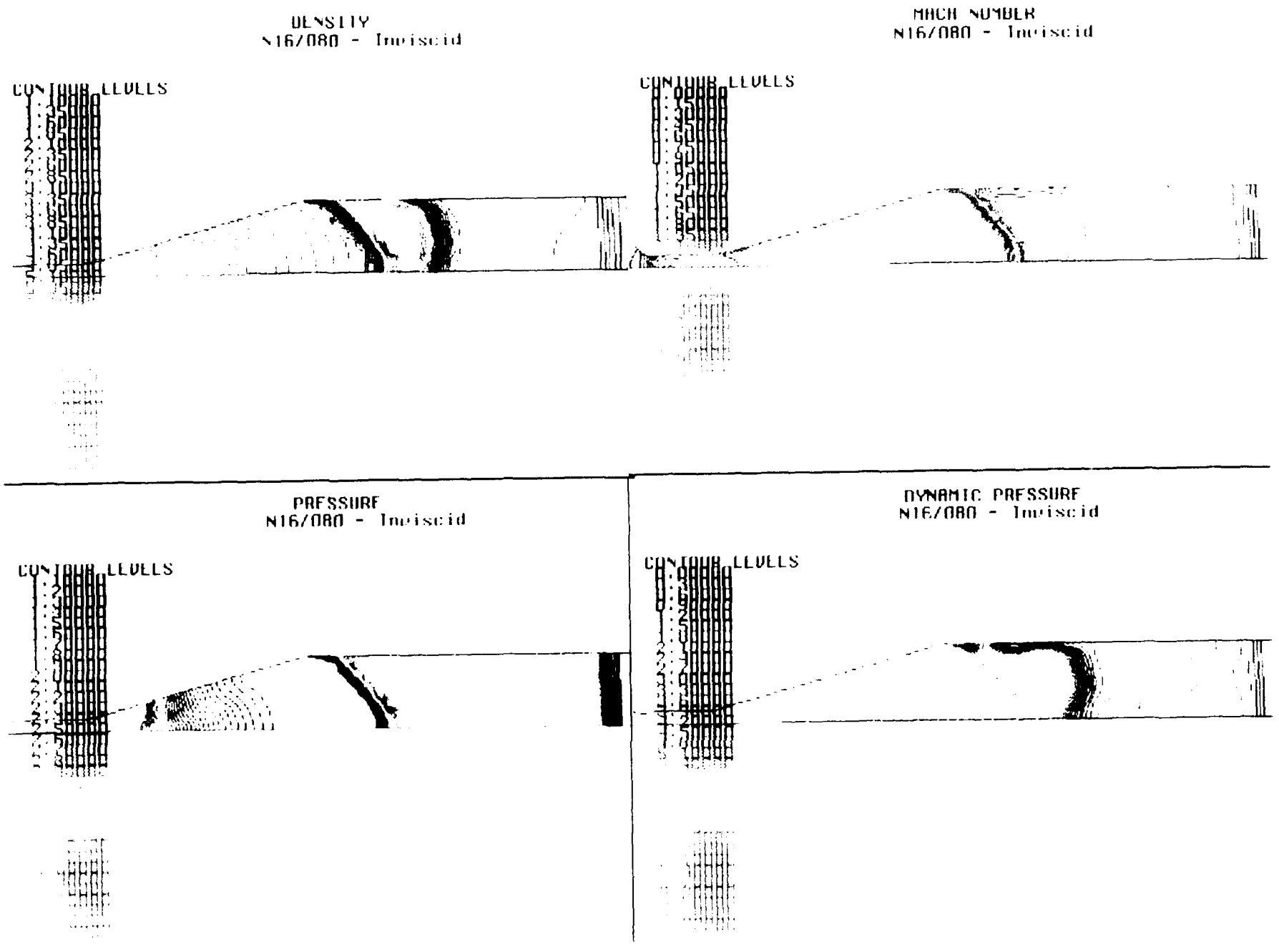

Figure 16. Inviscid 16° Nozzle Contour Plots–1.45 ms.

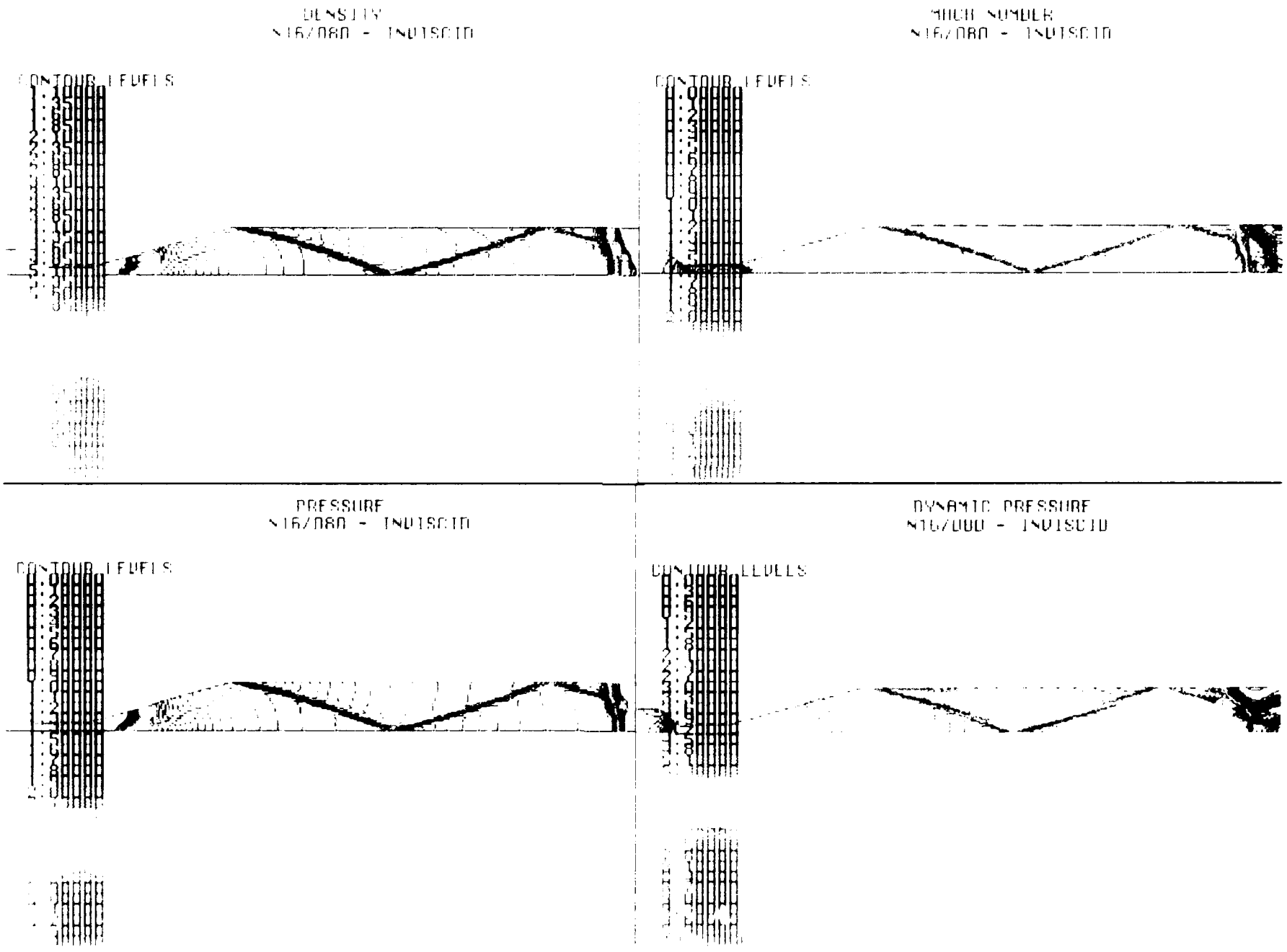

Figure 17. Inviscid 16° Nozzle Contour Plots–4.87 ms.

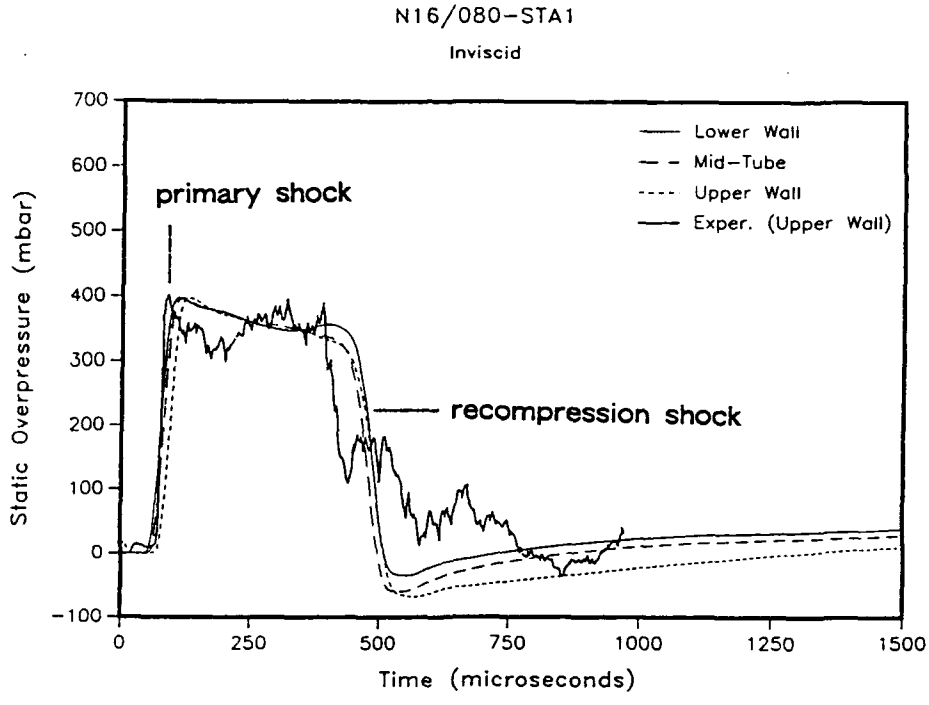

Figure 18a. Inviscid Static Overpressure vs. Time–16° Nozzle.

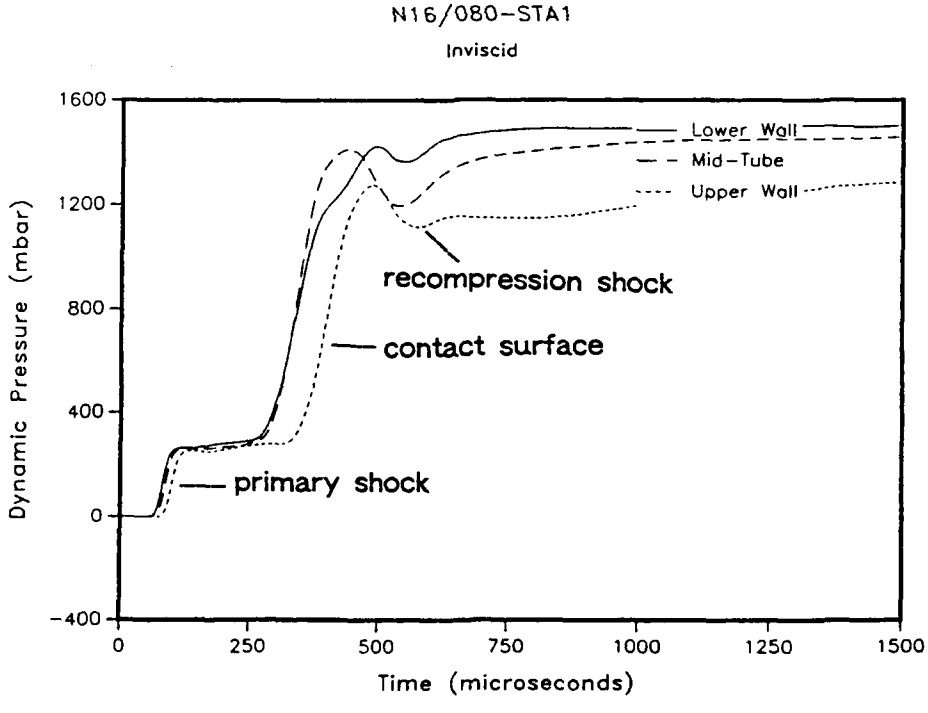

Figure 18b. Inviscid Dynamic Pressure vs. Time–16° Nozzle.

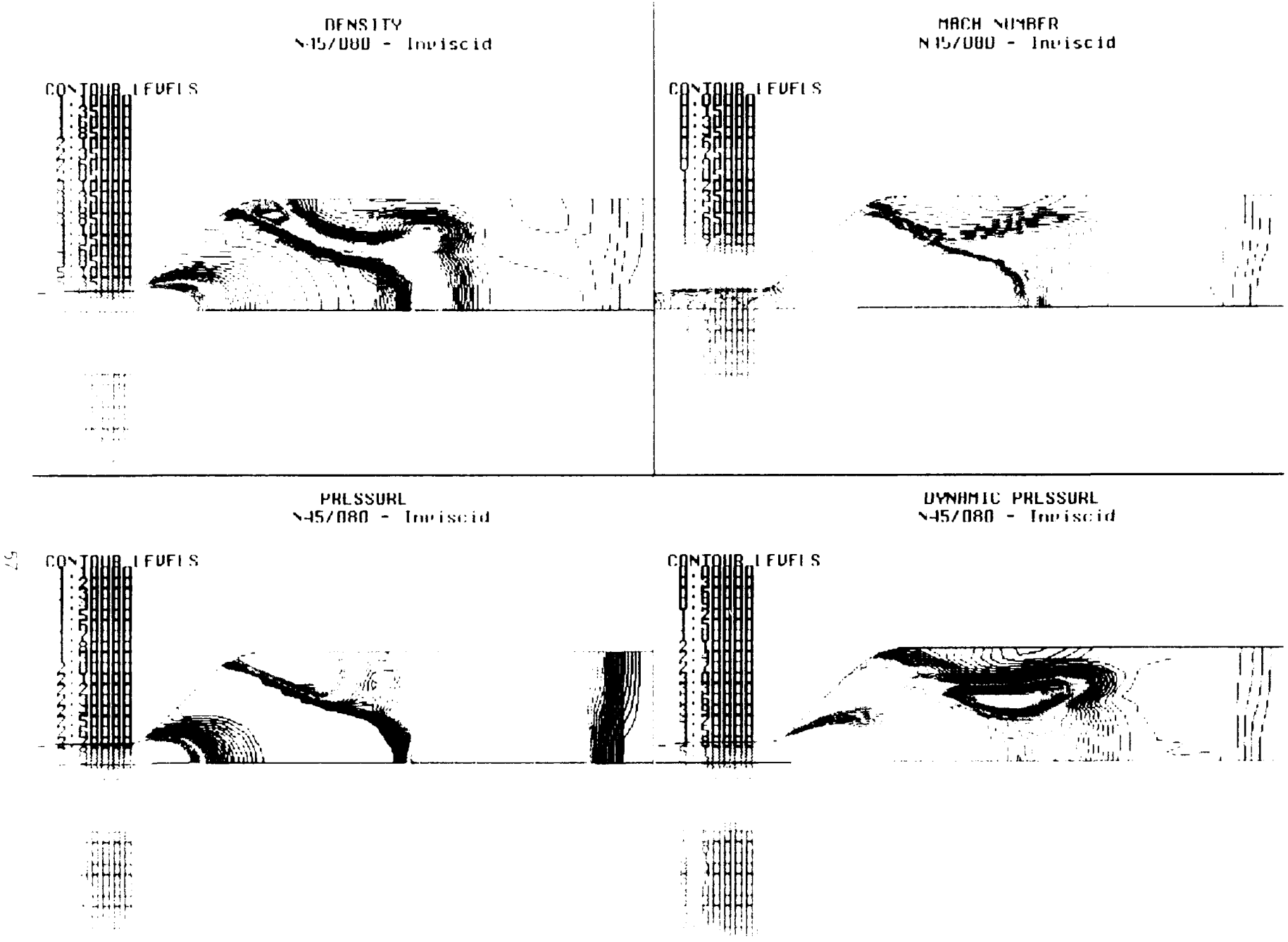

Figure 19. Inviscid 45° Nozzle Contour Plots–.92 ms.

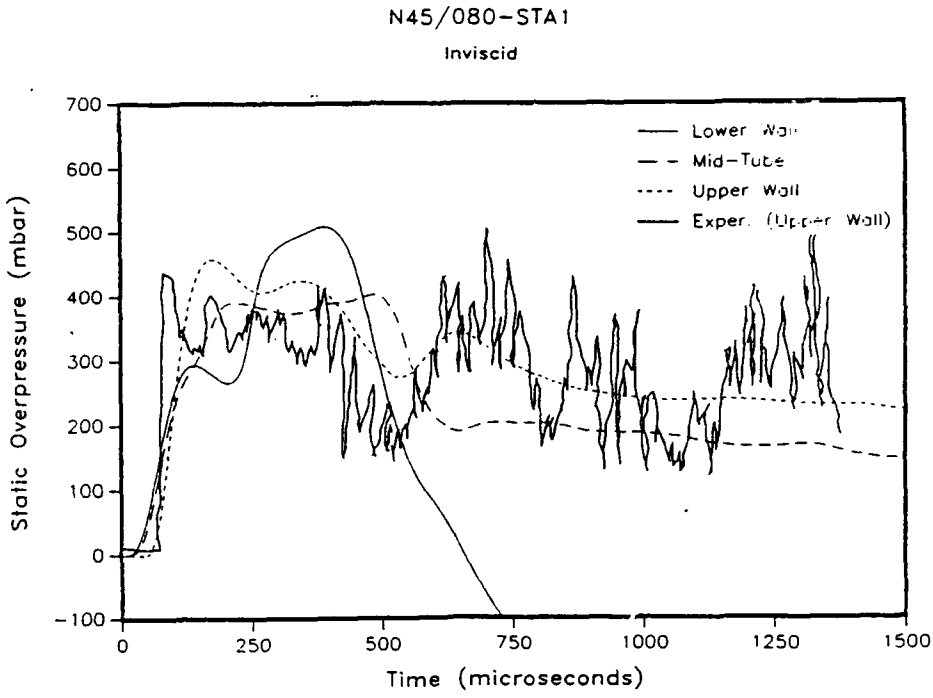

Figure 20a. Inviscid Static Overpressure vs. Time–45° Nozzle.

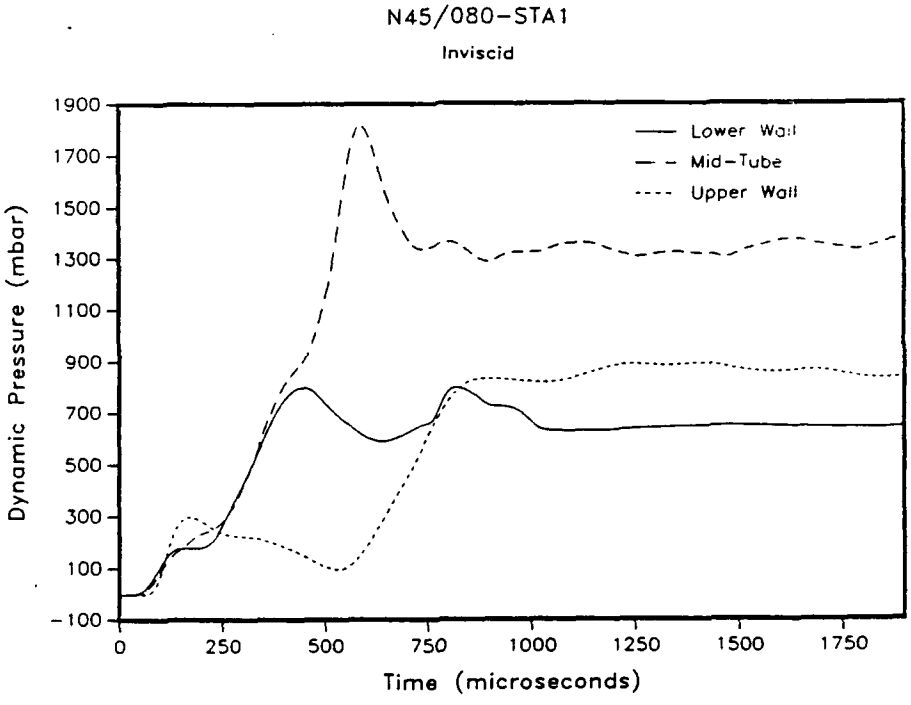

Figure 20b. Inviscid Dynamic Pressure versus Time - Forty-Five Degree Nozzle.

Figure 20b. Inviscid Dynamic Pressure vs. Time–45° Nozzle.

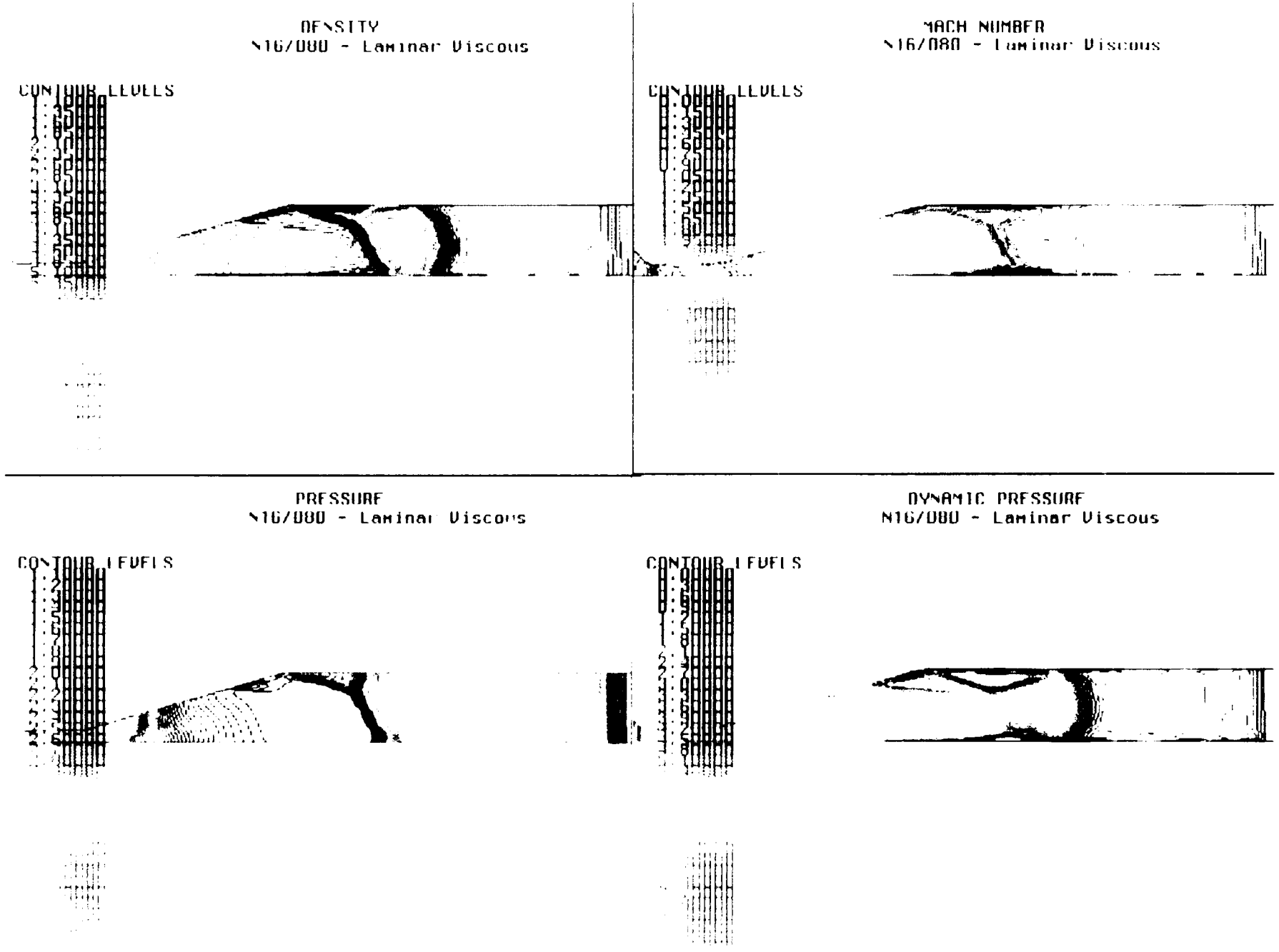

Figure 21. Laminar Viscous 16° Nozzle Contour Plots–1.62 ms.

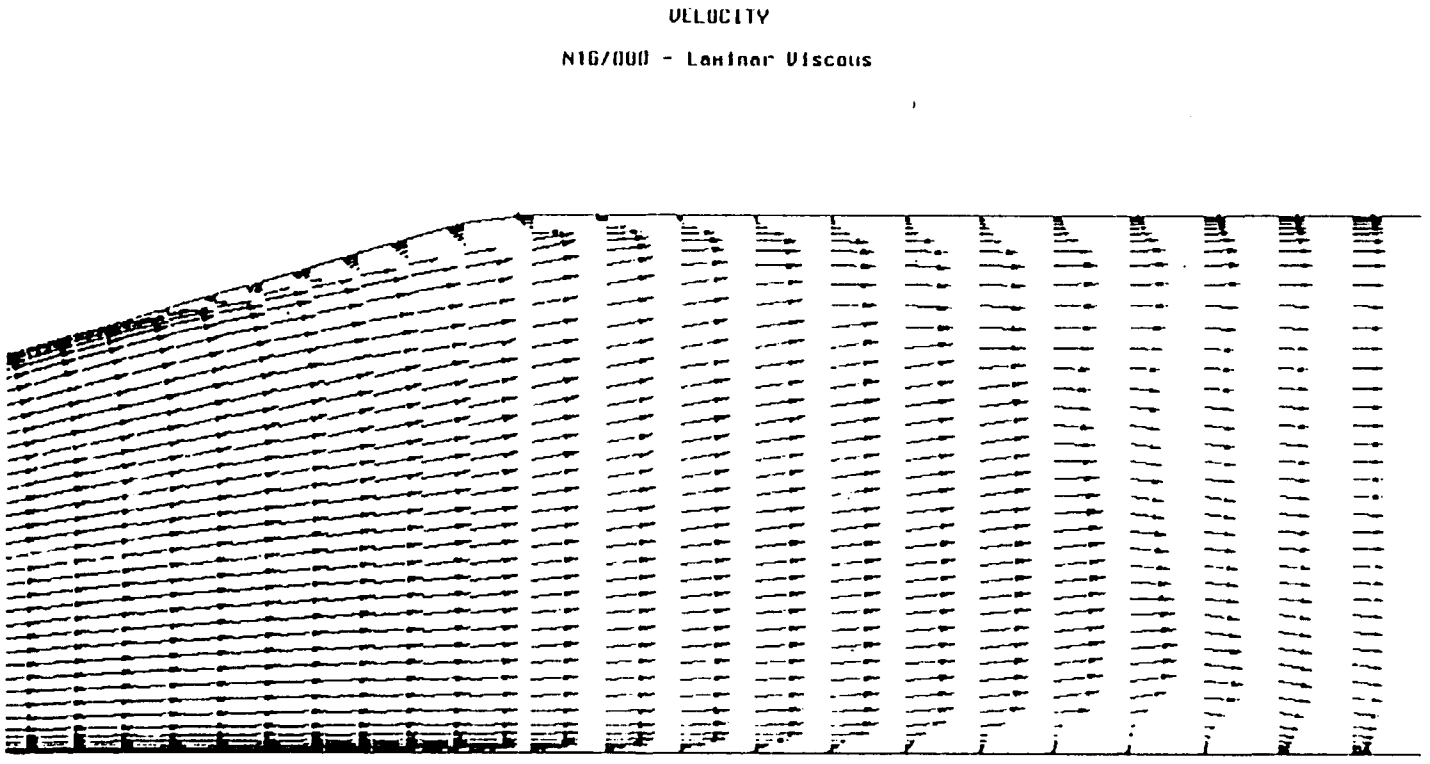

Figure 22. Laminar Viscous Velocity Vectors Plot, 16° Nozzle–1.62 ms.

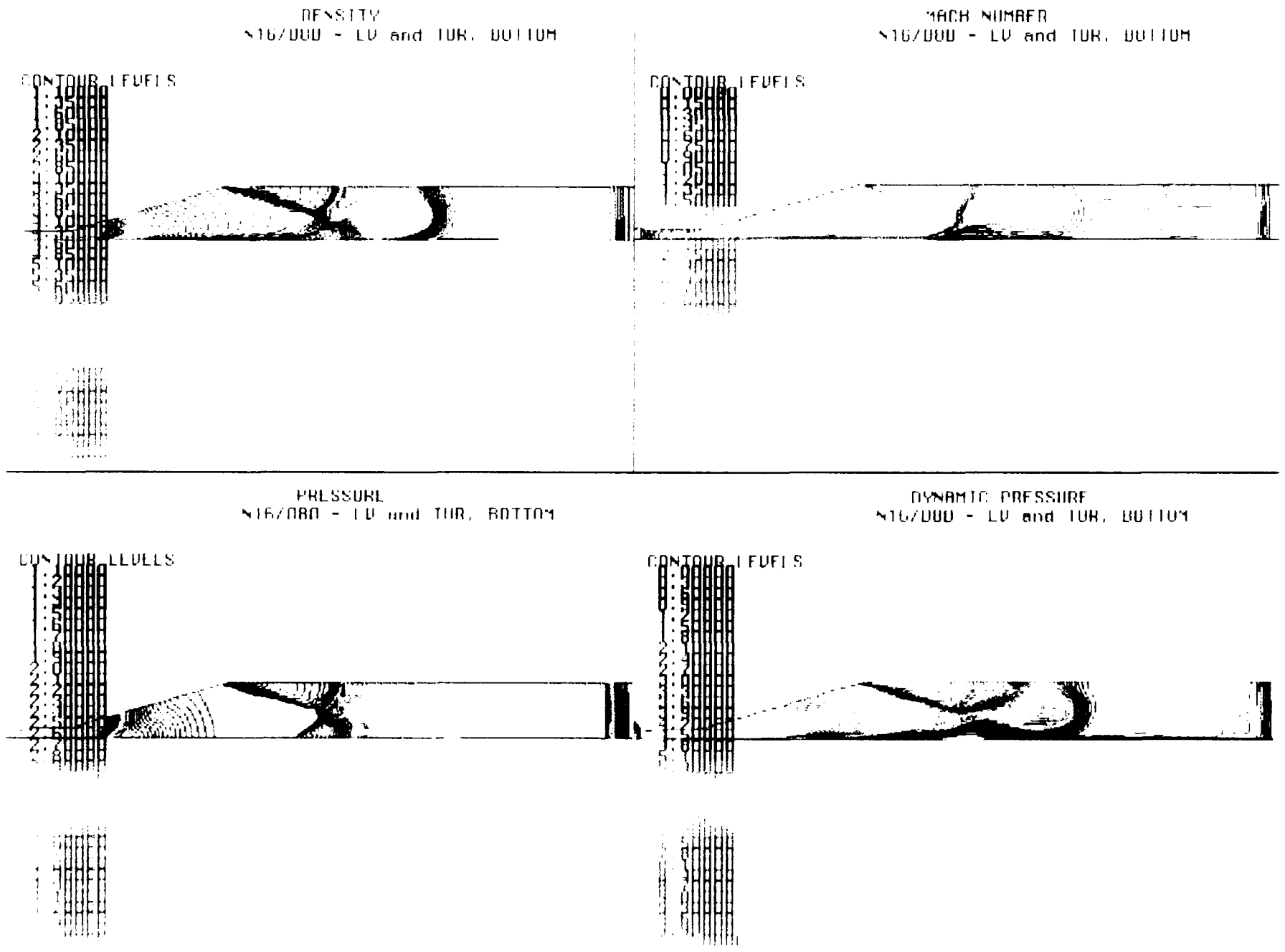

Figure 23. "LV and TUR Bot," 16° Nozzle Contour Plots–2.1 ms.

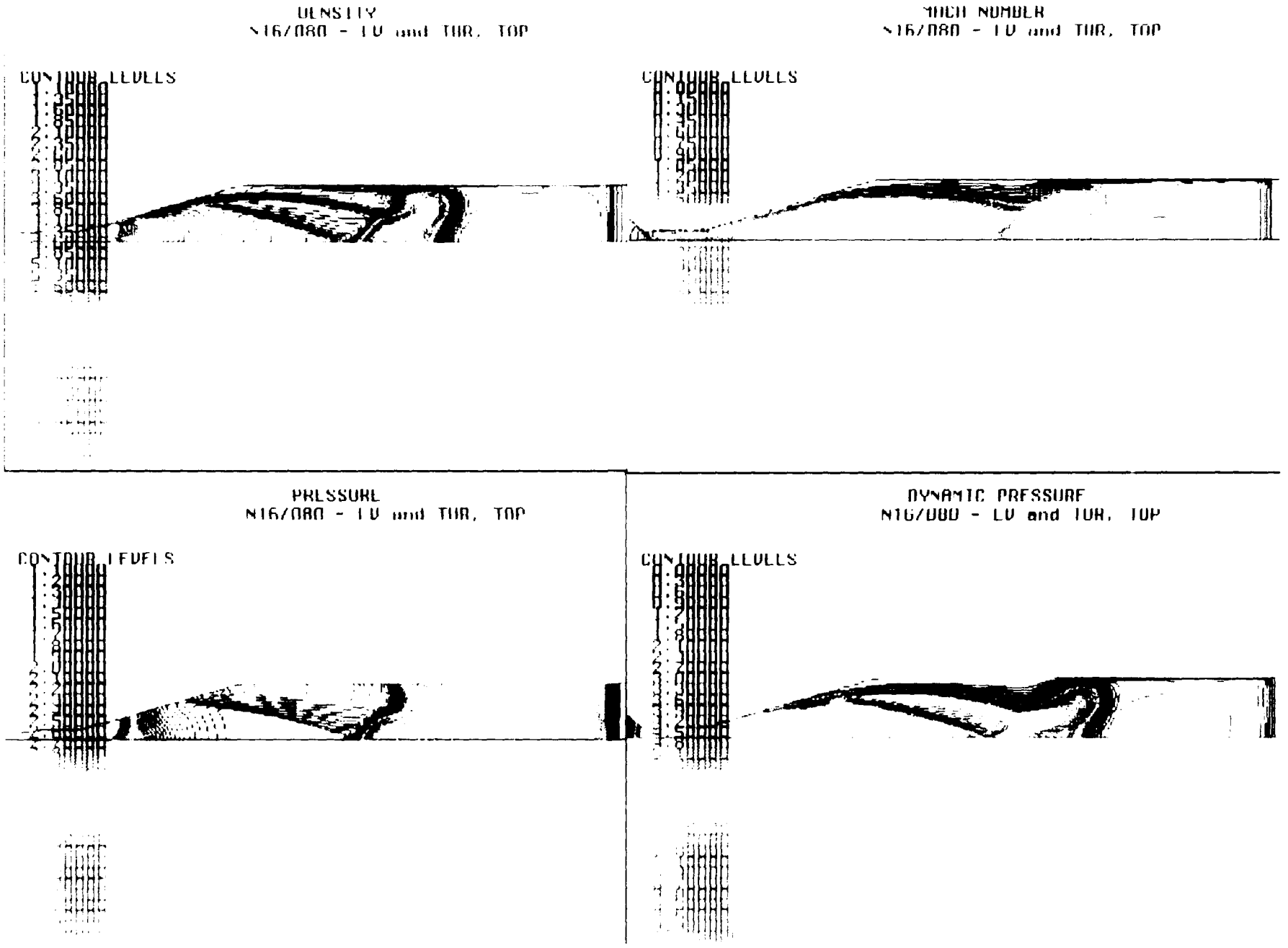

Figure 24. "LV and TUR Top," 16° Nozzle Contour Plots–2.0 ms.

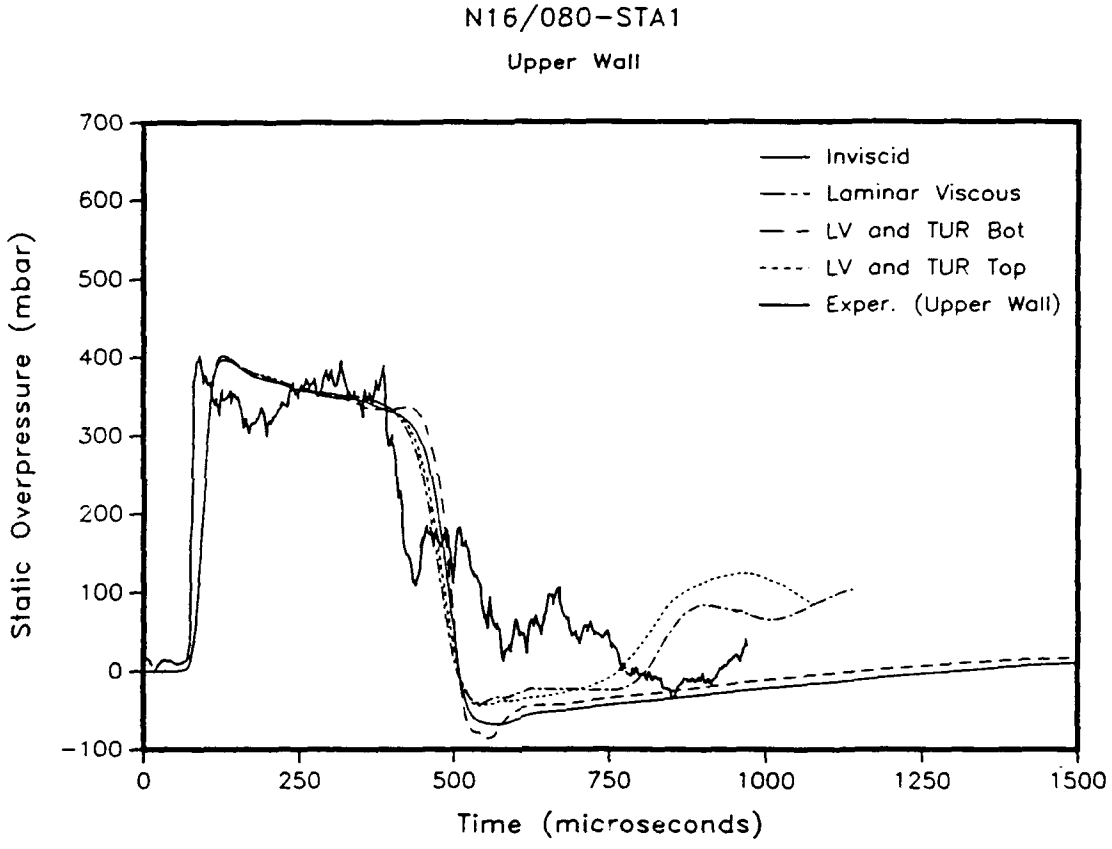

Figure 25. Comparison of Inviscid, Laminar Viscous, and Turbulent Static Overpressure vs. Time, 16° Nozzle, Upper Wall.

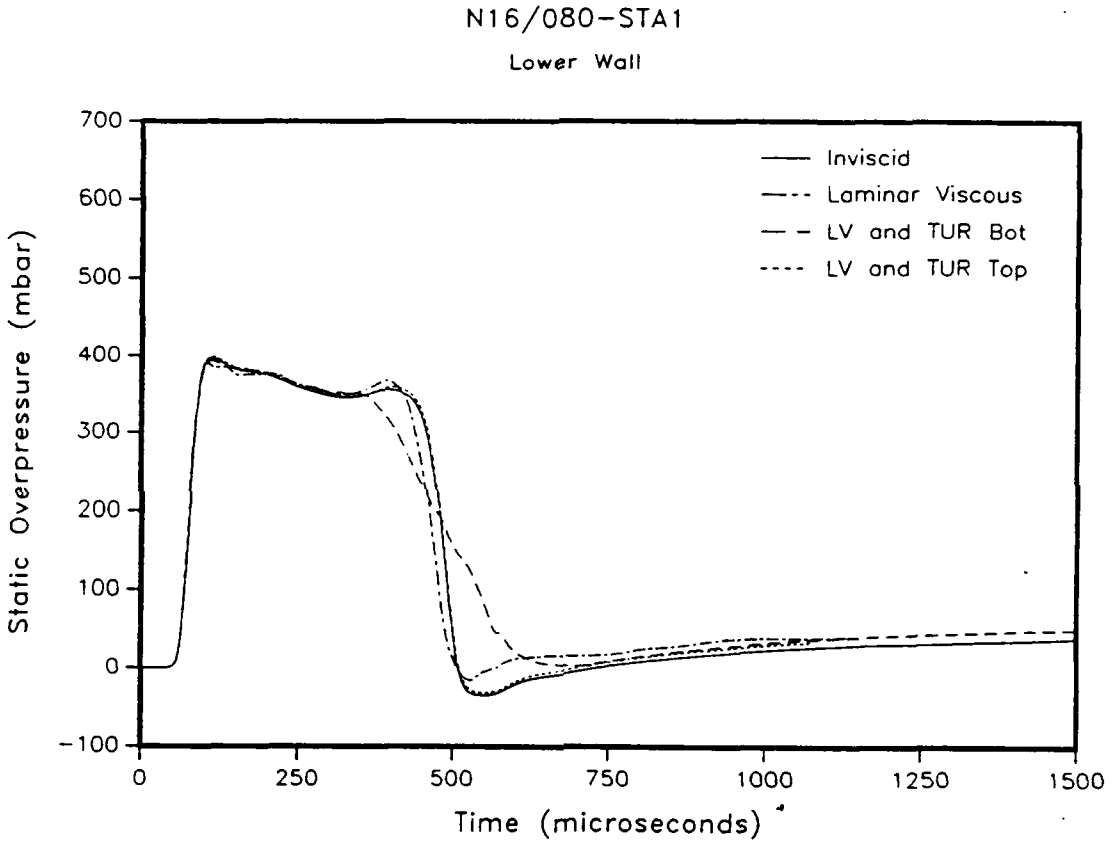

Figure 26. Comparison of Inviscid, Laminar Viscous, and Turbulent Static Overpressure vs. Time, 16° Nozzle, Lower Wall.

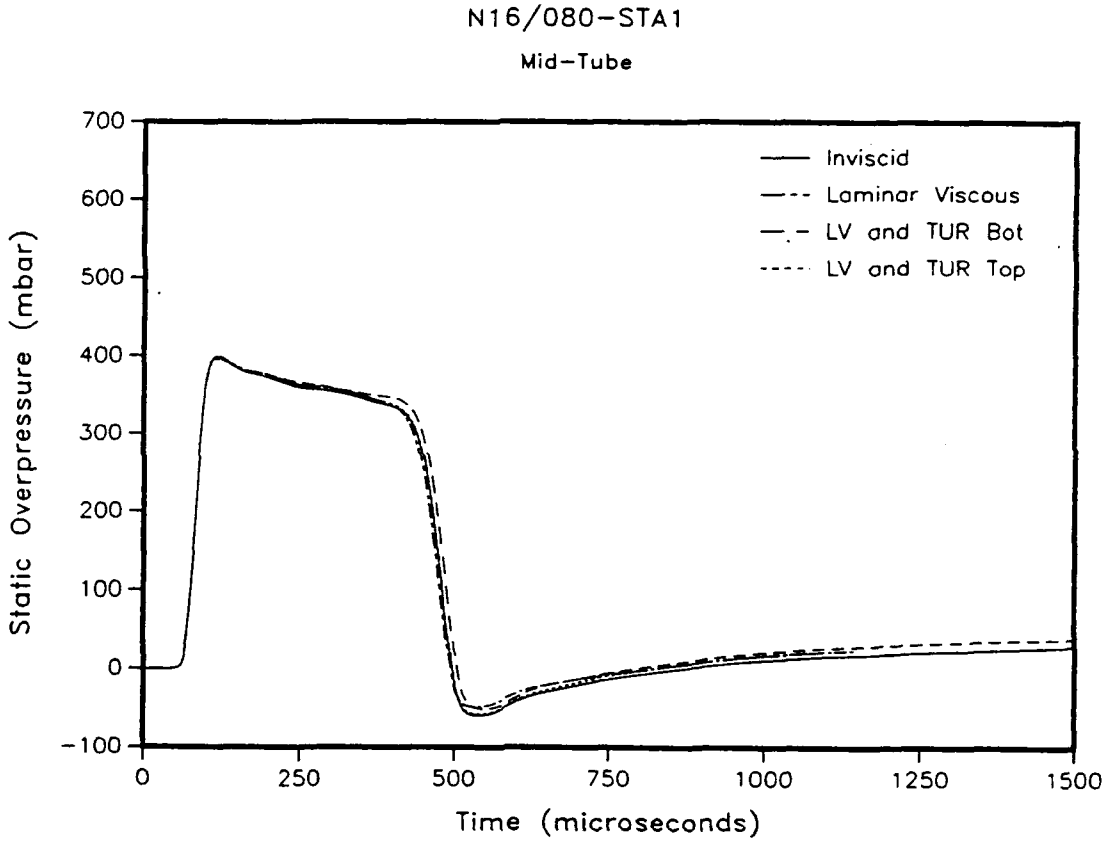

Figure 27. Comparison of Inviscid, Laminar Viscous, and Turbulent Static Overpressure vs. Time, 16° Nozzle, Mid-tube.

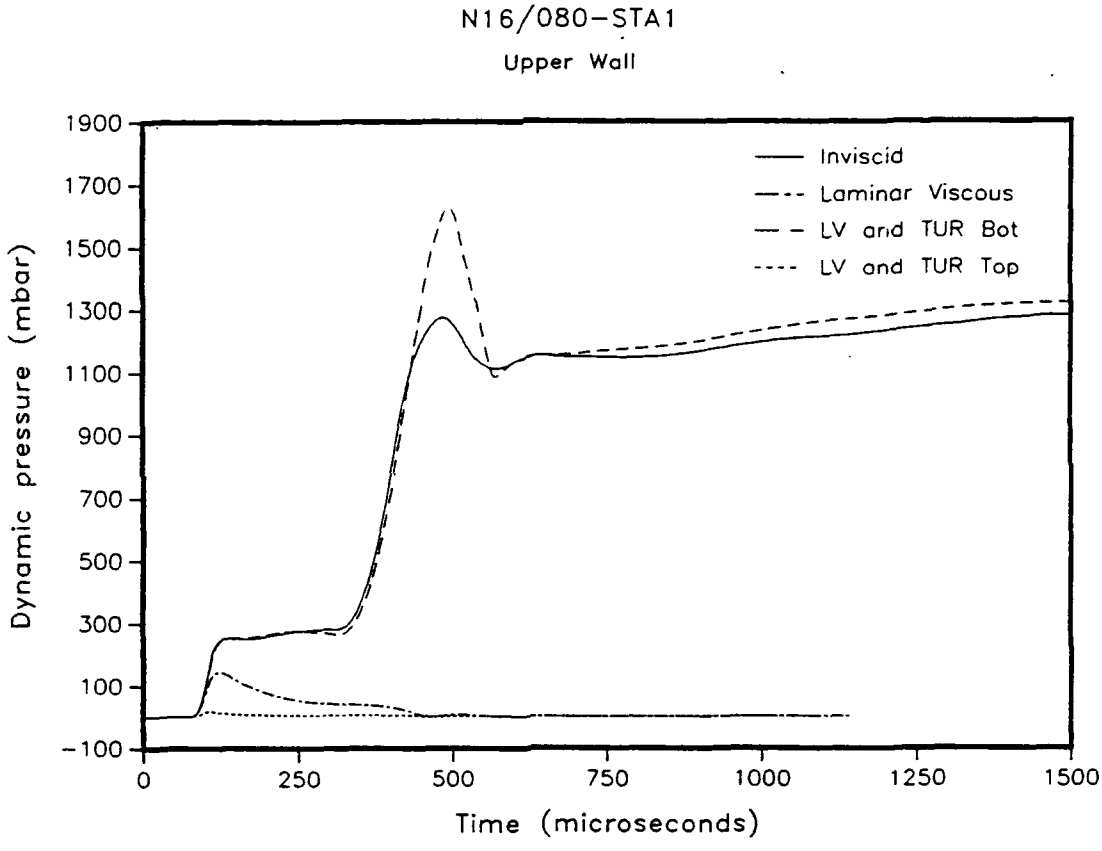

Figure 28. Comparison of Inviscid, Laminar Viscous, and Turbulent Dynamic Pressure vs. Time, 16° Nozzle, Upper Wall.

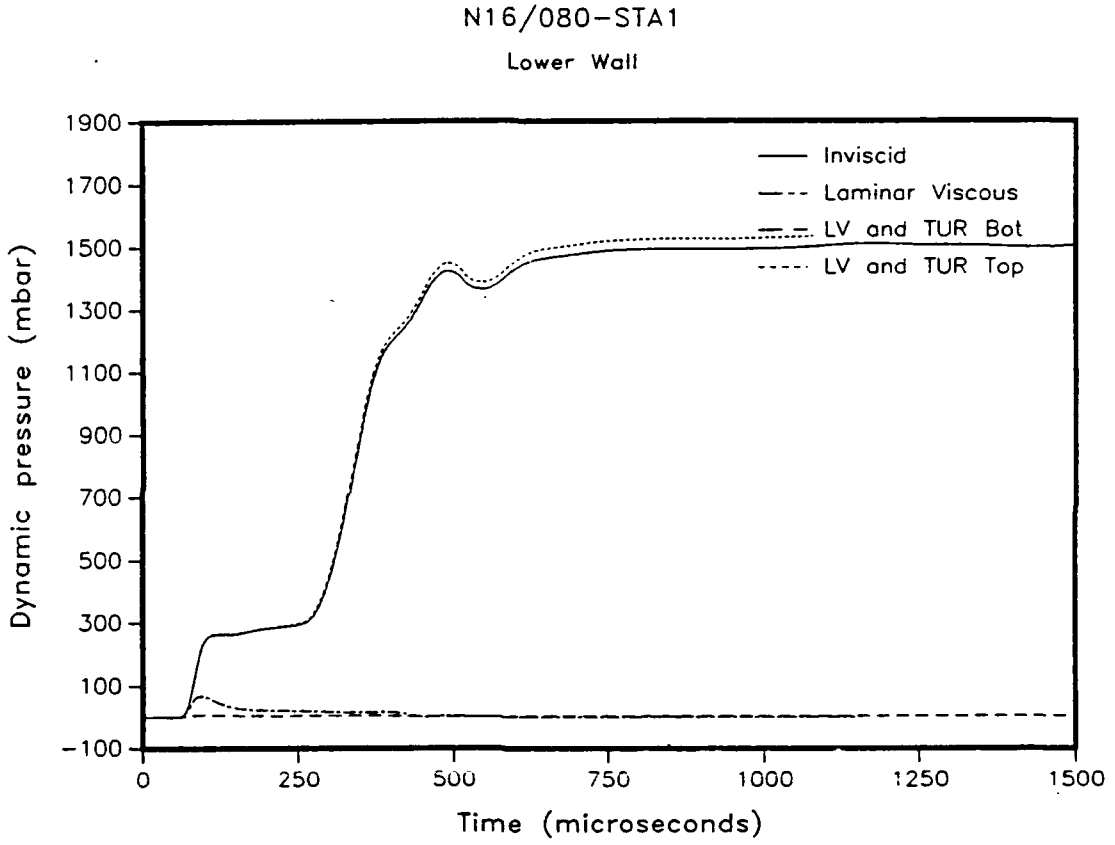

Figure 29. Comparison of Inviscid, Laminar Viscous, and Turbulent Dynamic Pressure vs. Time, 16° Nozzle, Lower Wall.

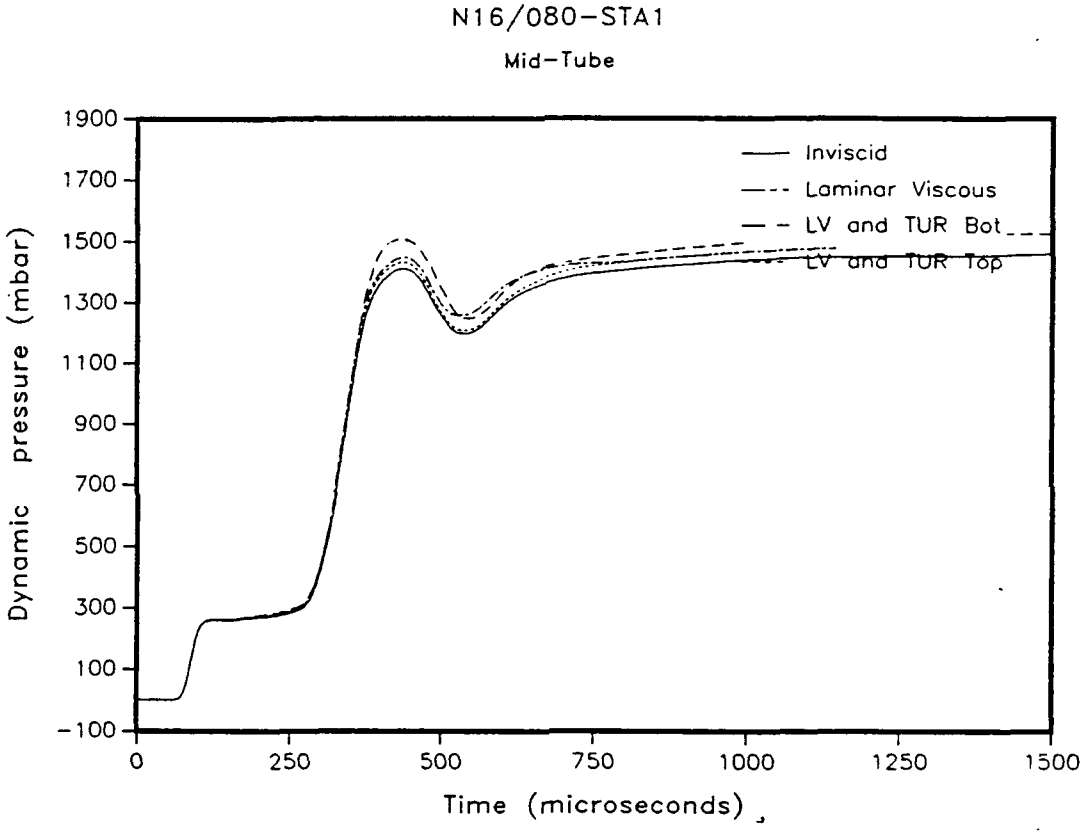

Figure 30. Comparison of Inviscid, Laminar Viscous, and Turbulent Dynamic Pressure vs. Time, 16° Nozzle, Mid-tube.

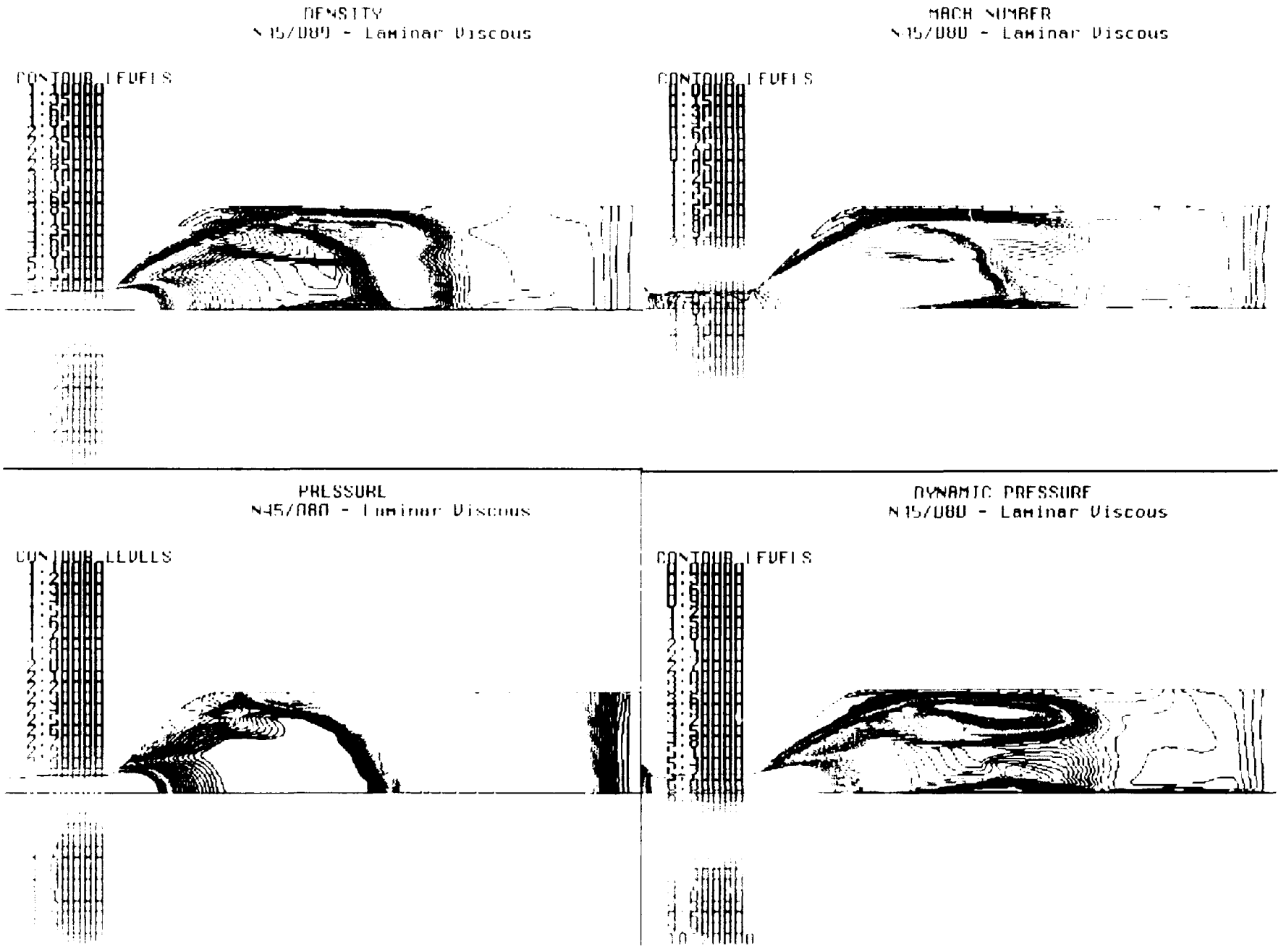

Figure 31. Laminar Viscous 45° Nozzle Contour Plots–1.1 ms.

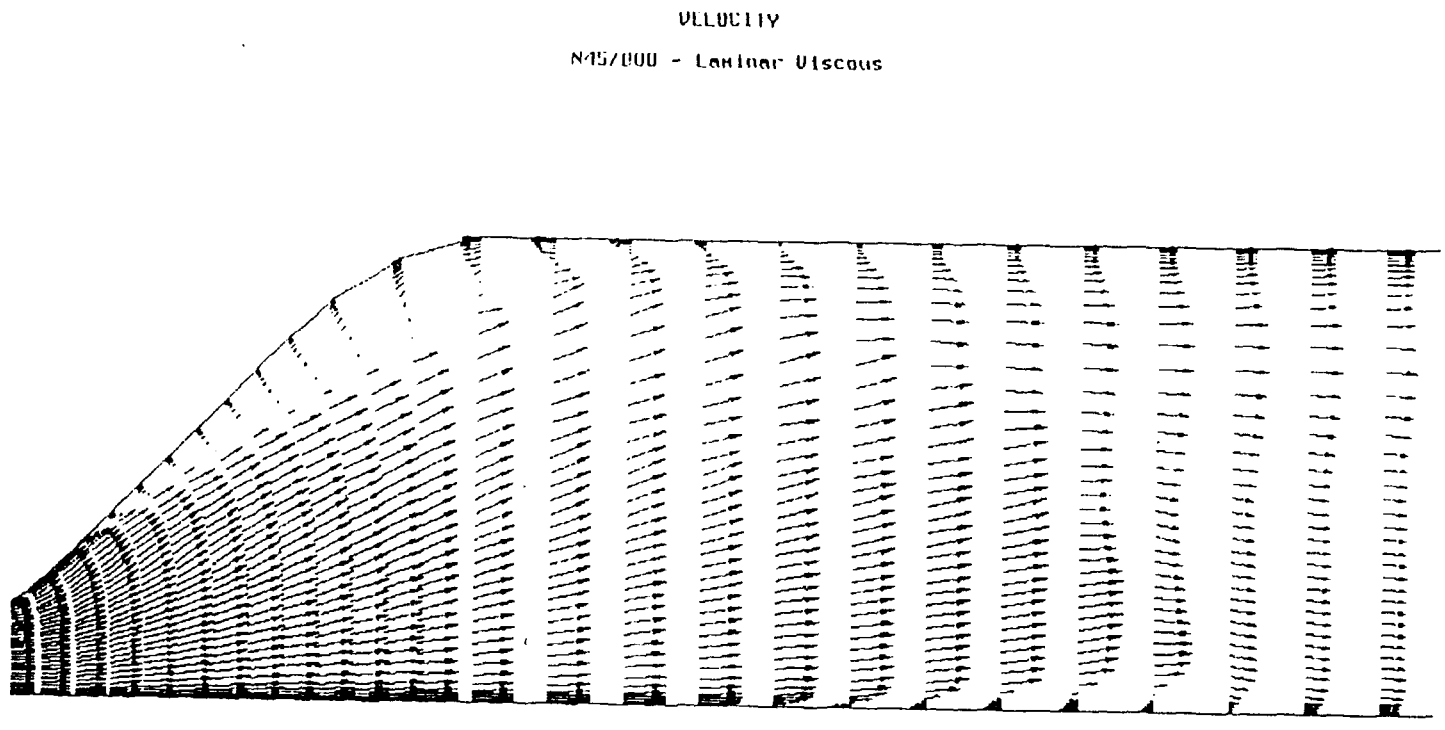

Figure 32. Laminar Viscous Velocity Vectors Plot, 45° Nozzle–1.1 ms.

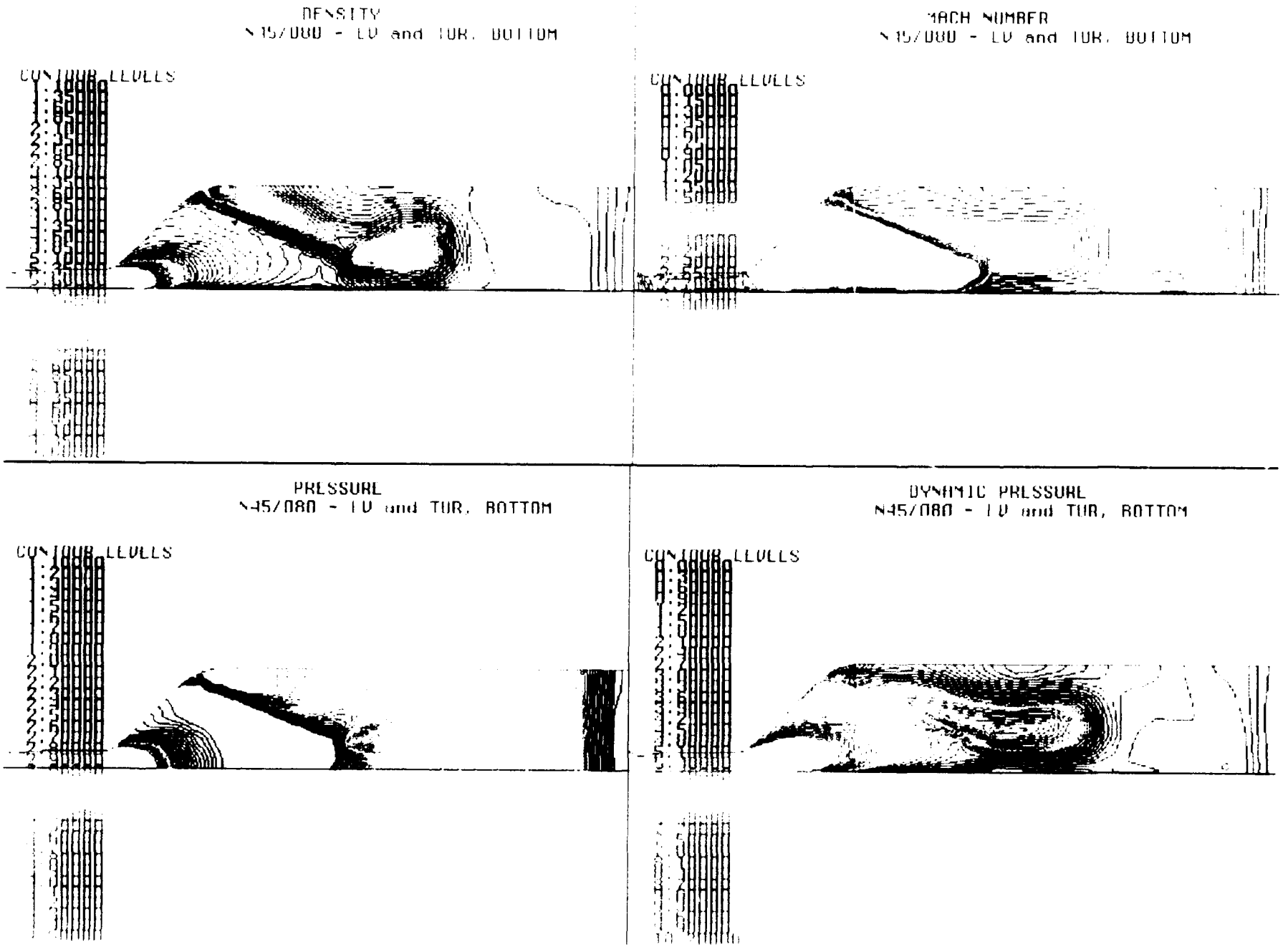

Figure 33. "LV and TUR Bot," 45° Nozzle Contour Plots–1.1 rns.

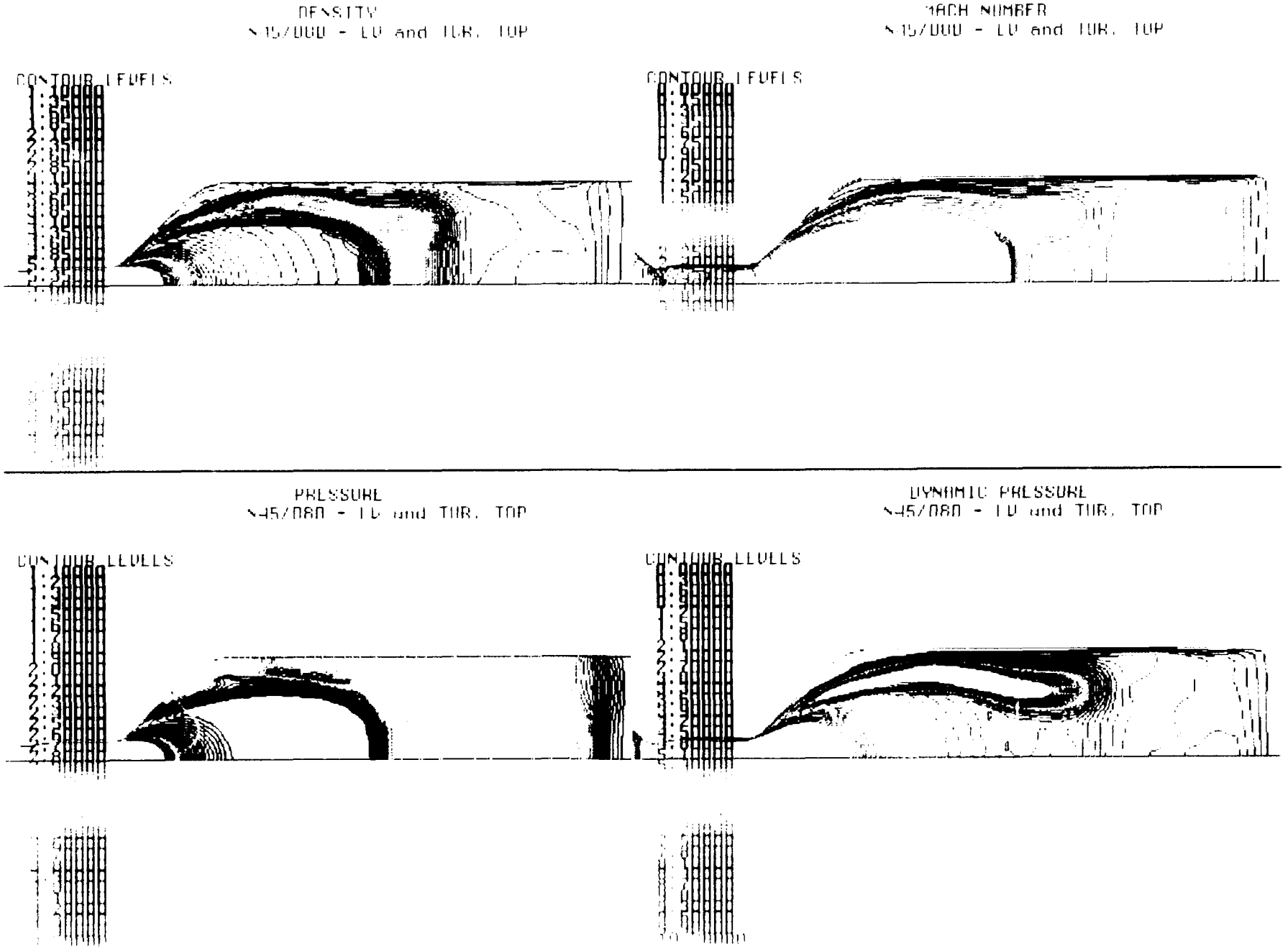

Figure 34. "LV and TUR Top," 45° Nozzle Contour Plots–1.1 ms.

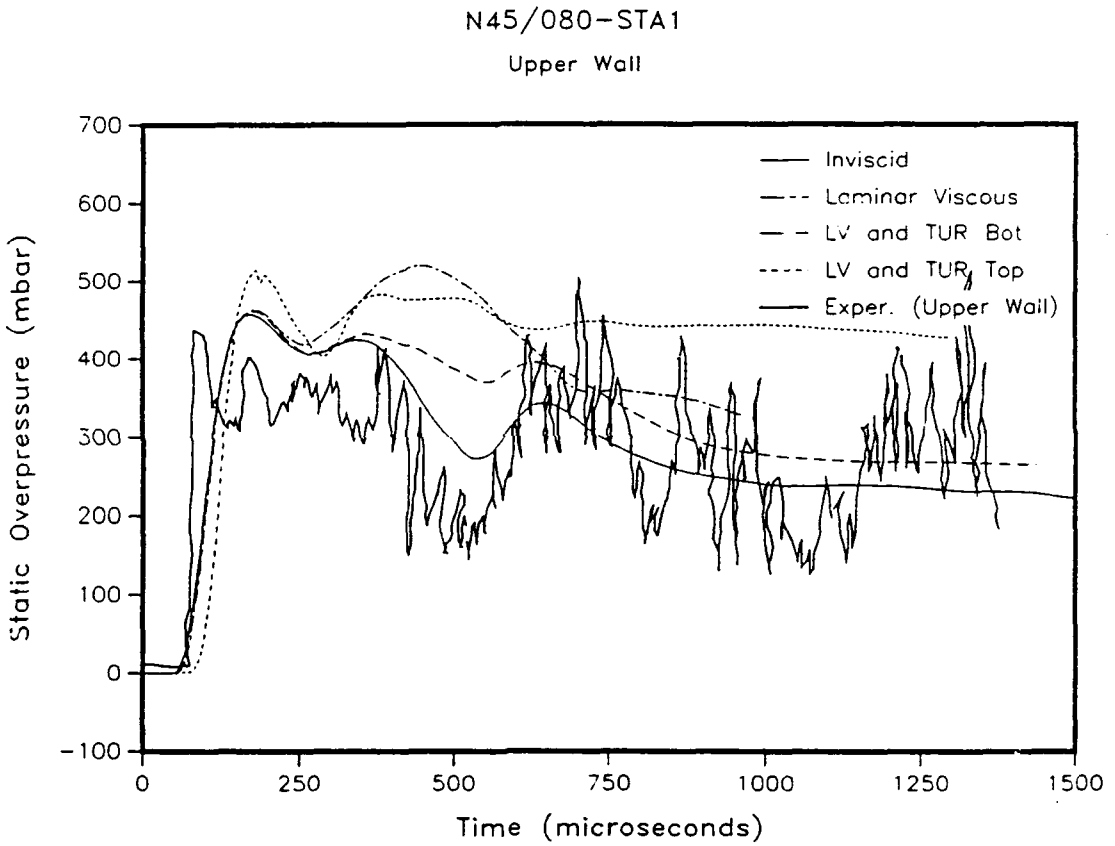

Figure 35. Comparison of Inviscid, Laminar Viscous, and Turbulent Static Overpressure vs. Time, 45° Nozzle, Upper Wall.

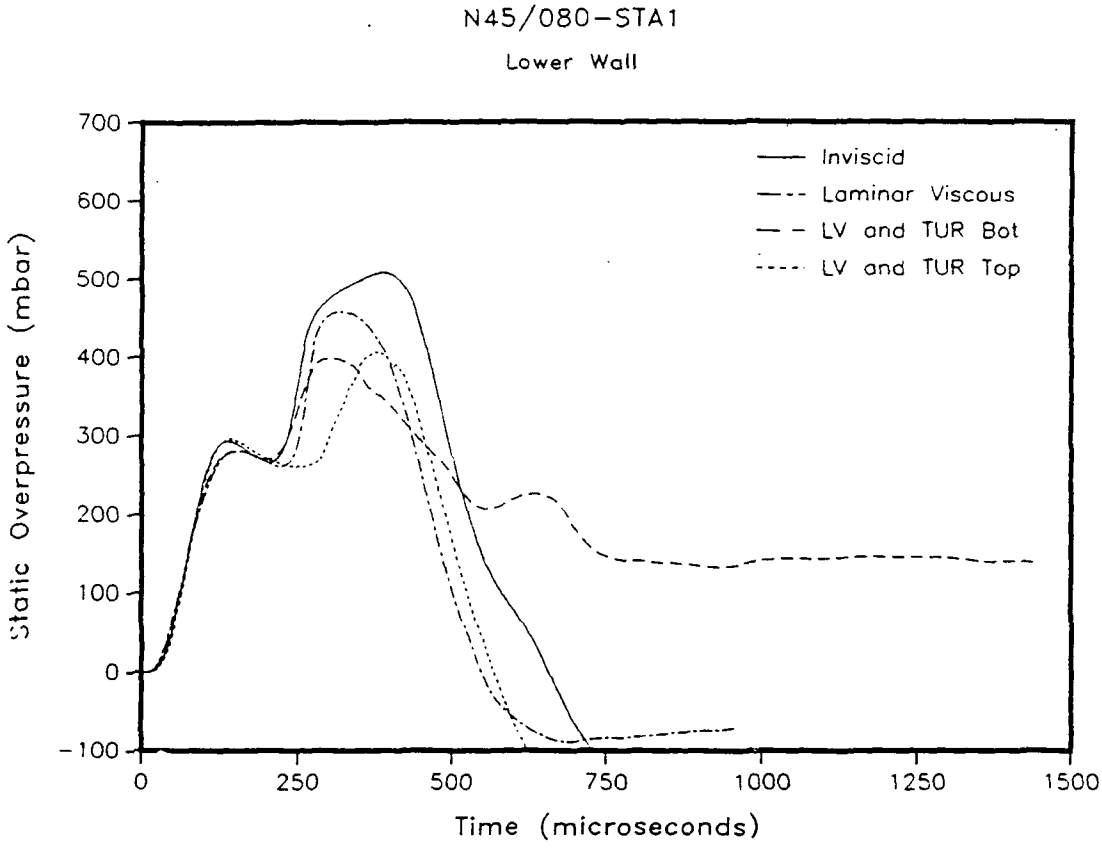

Figure 36. Comparison of Inviscid, Laminar Viscous, and Turbulent Static Overpressure vs. Time, 45° Nozzle, Lower Wall.

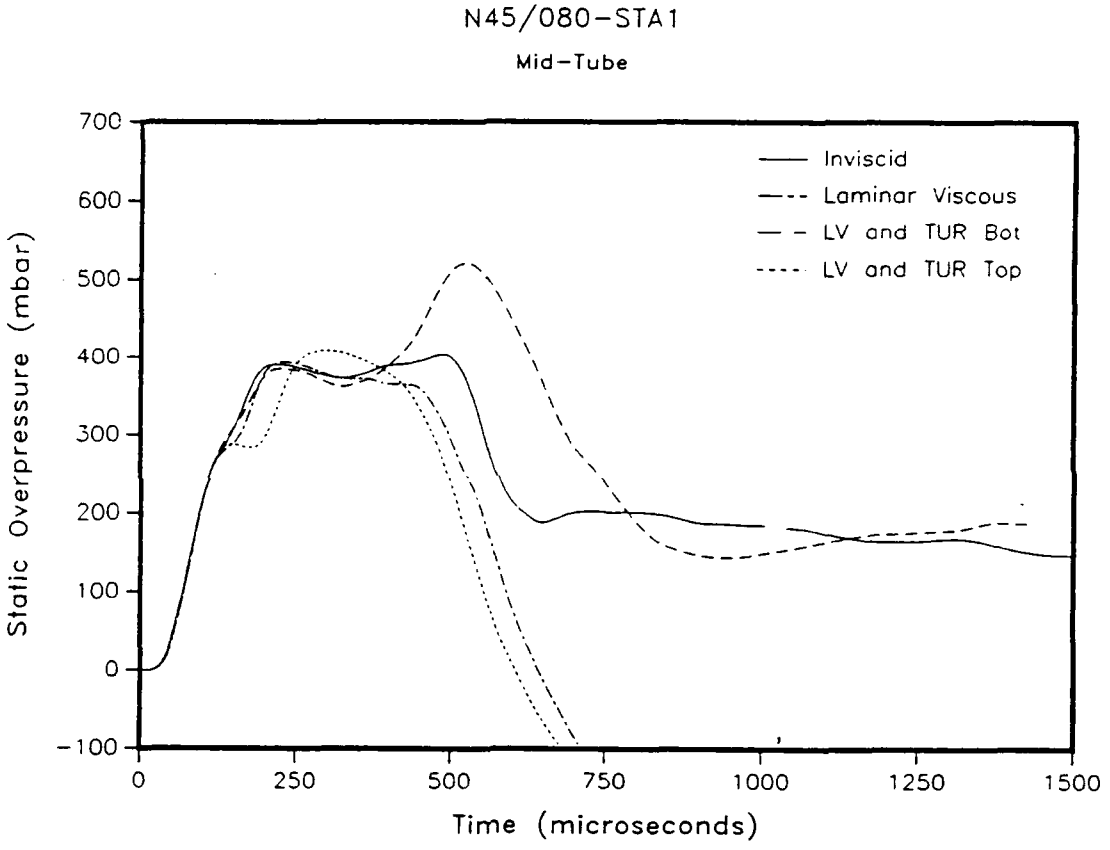

Figure 37. Comparison of Inviscid, Laminar Viscous, and Turbulent Static Overpressure vs. Time, 45° Nozzle, Mid-tube.

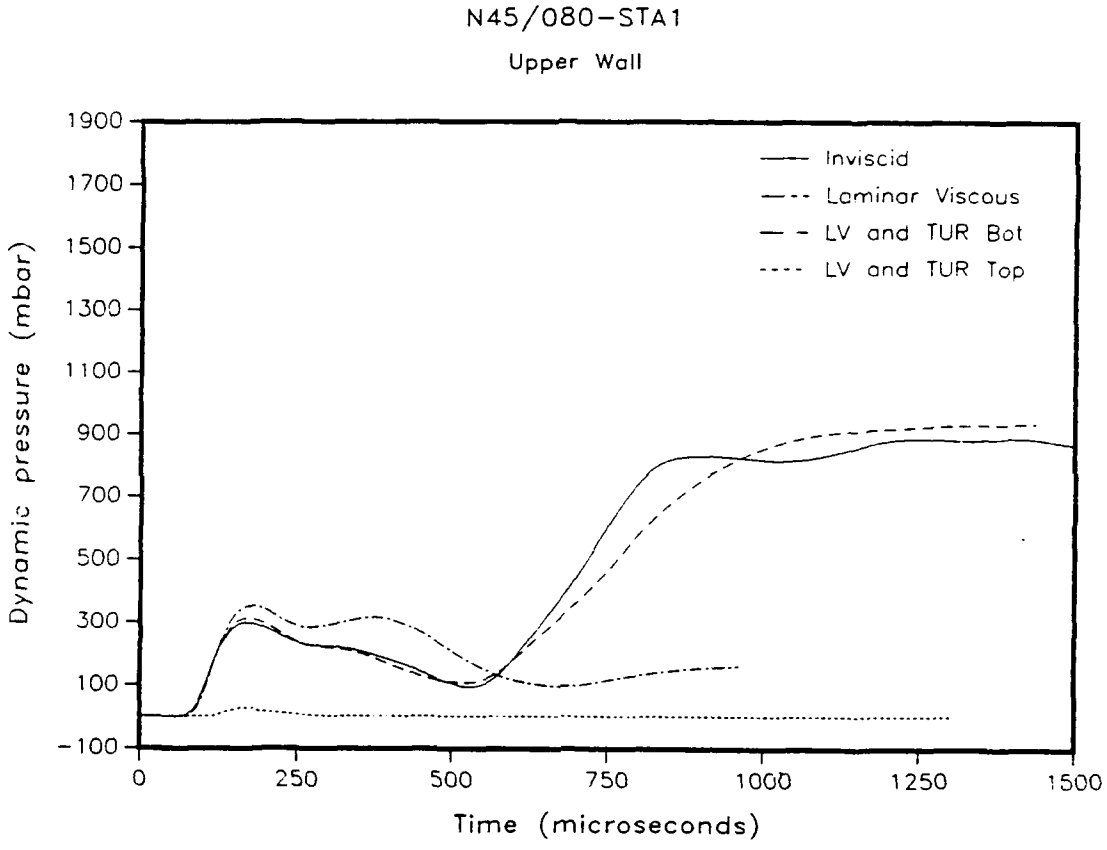

Figure 38. Comparison of Inviscid, Laminar Viscous, and Turbulent Dynamic Pressure vs. Time, 45° Nozzle, Upper Wall.

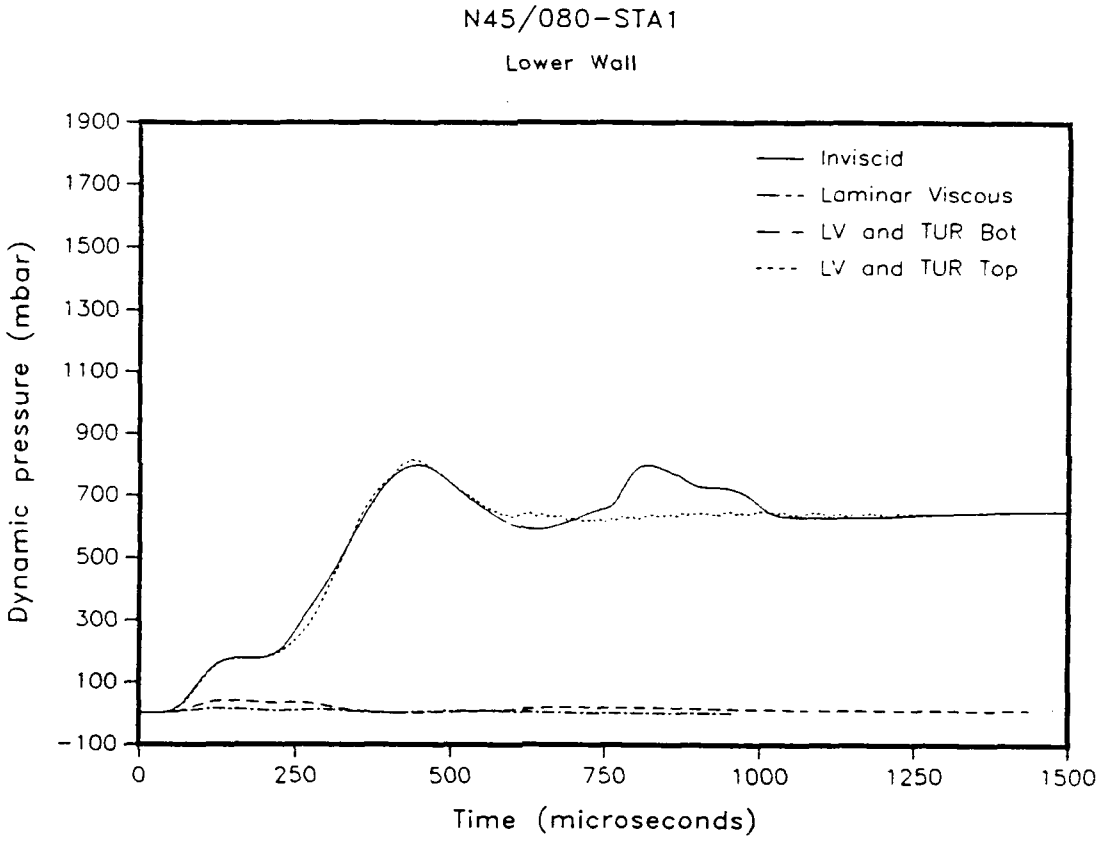

Figure 39. Comparison of Inviscid, Laminar Viscous, and Turbulent Dynamic Pressure vs. Time, 45° Nozzle, Lower Wall.

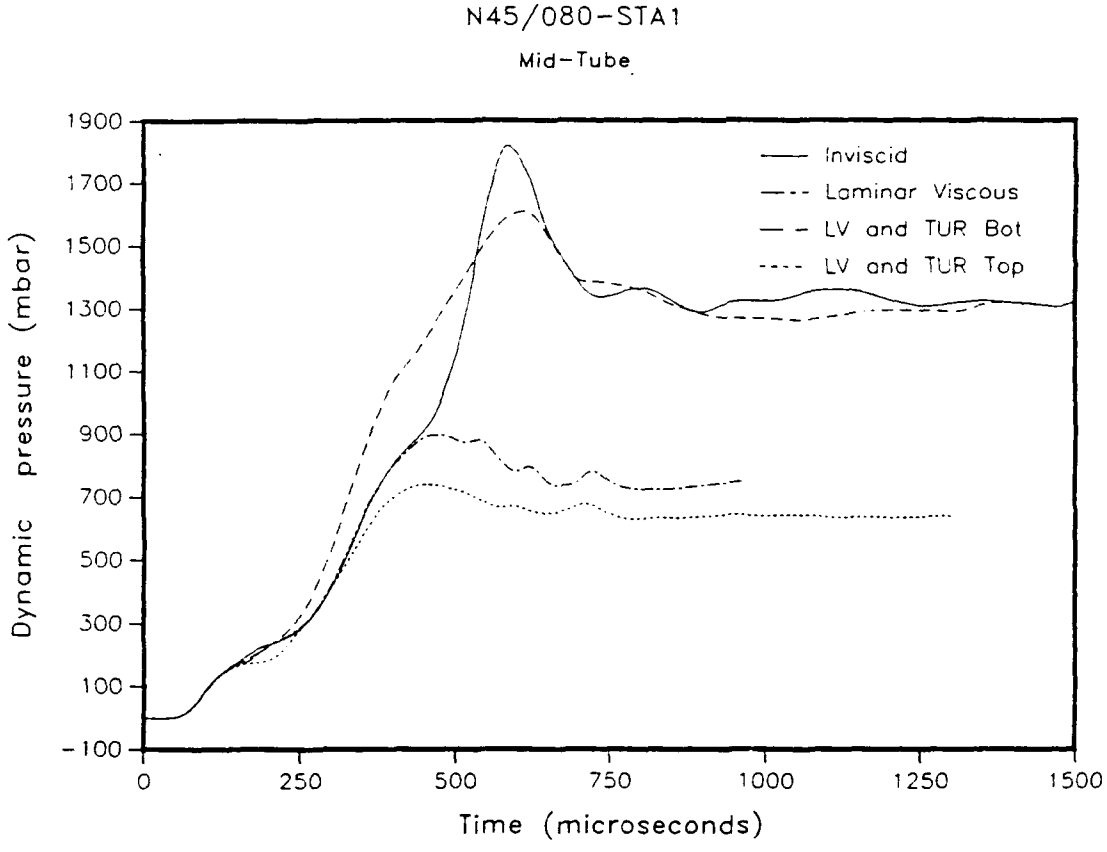

Figure 40. Comparison of Inviscid, Laminar Viscous, and Turbulent Dynamic Pressure vs. Time, 45° Nozzle, Mid-tube.

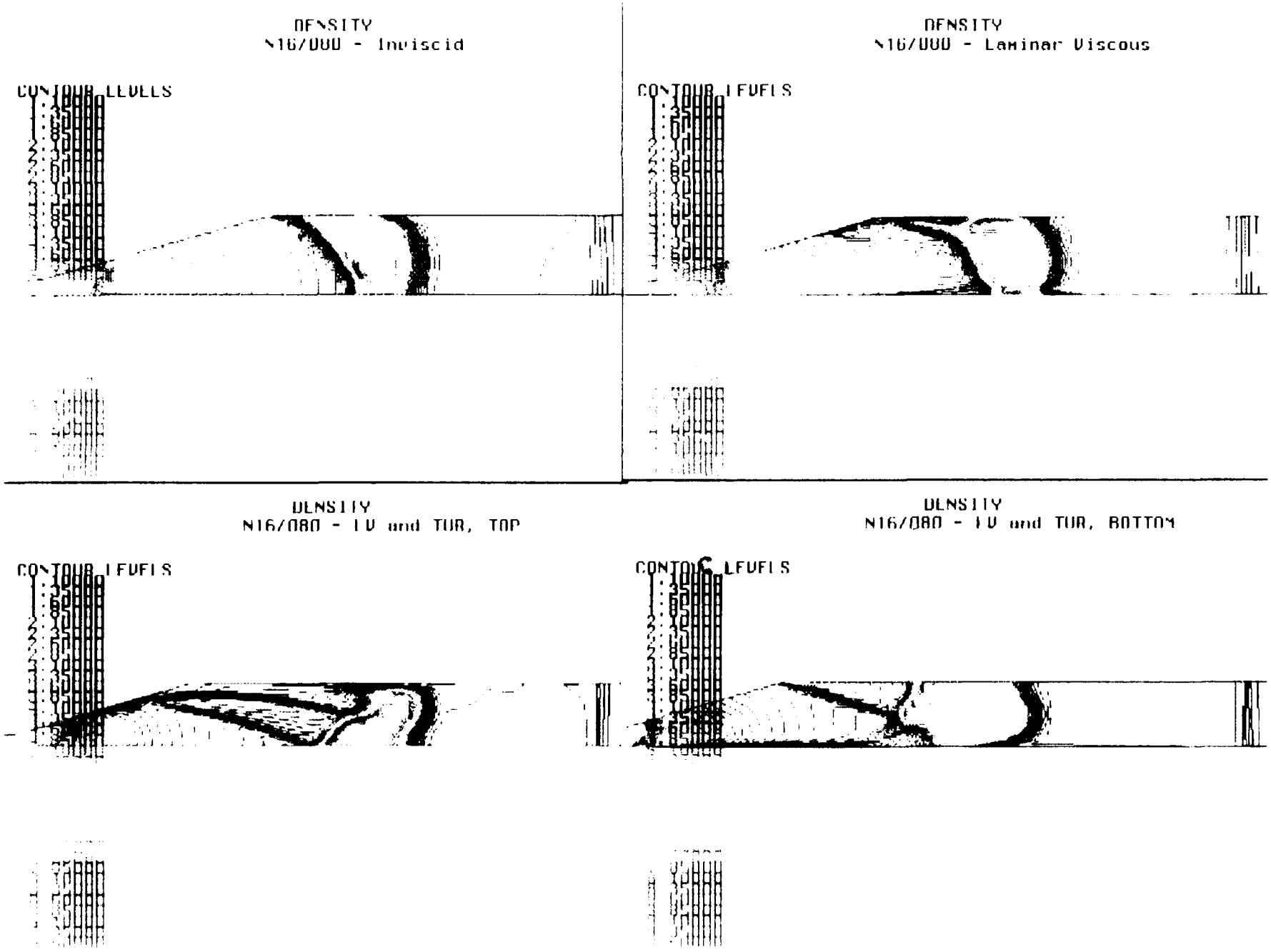

Figure 41. Comparison of the Inviscid, Laminar Viscous, and Turbulent Density Contour Plots, 16° Nozzle.

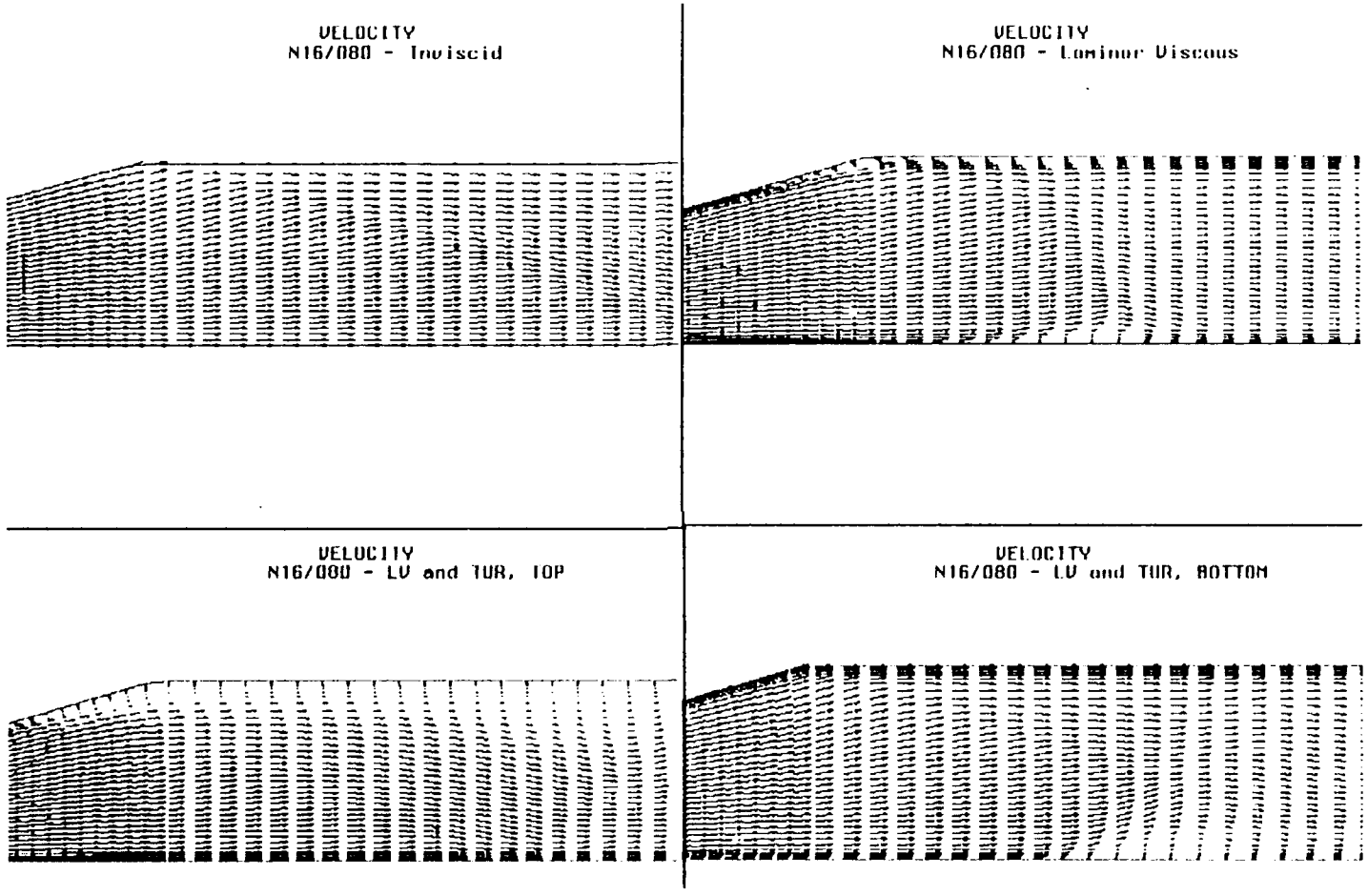

Figure 42. Comparison of the Inviscid, Laminar Viscous, and Turbulent Velocity Vectors Plots, 16° Nozzle.

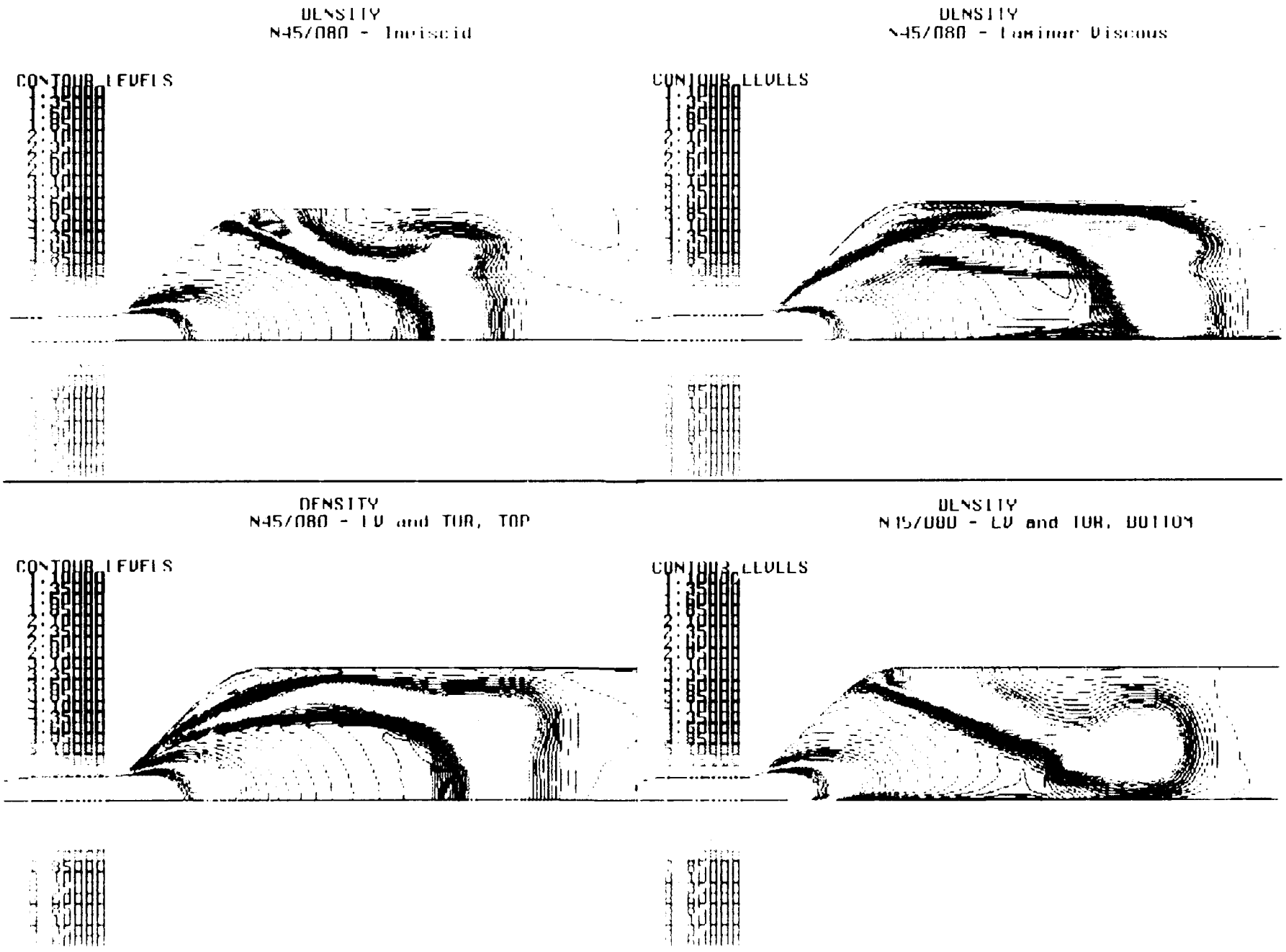

Figure 43. Comparison of the Inviscid, Laminar Viscous, and Turbulent Density Contour Plots, 45° Nozzle.

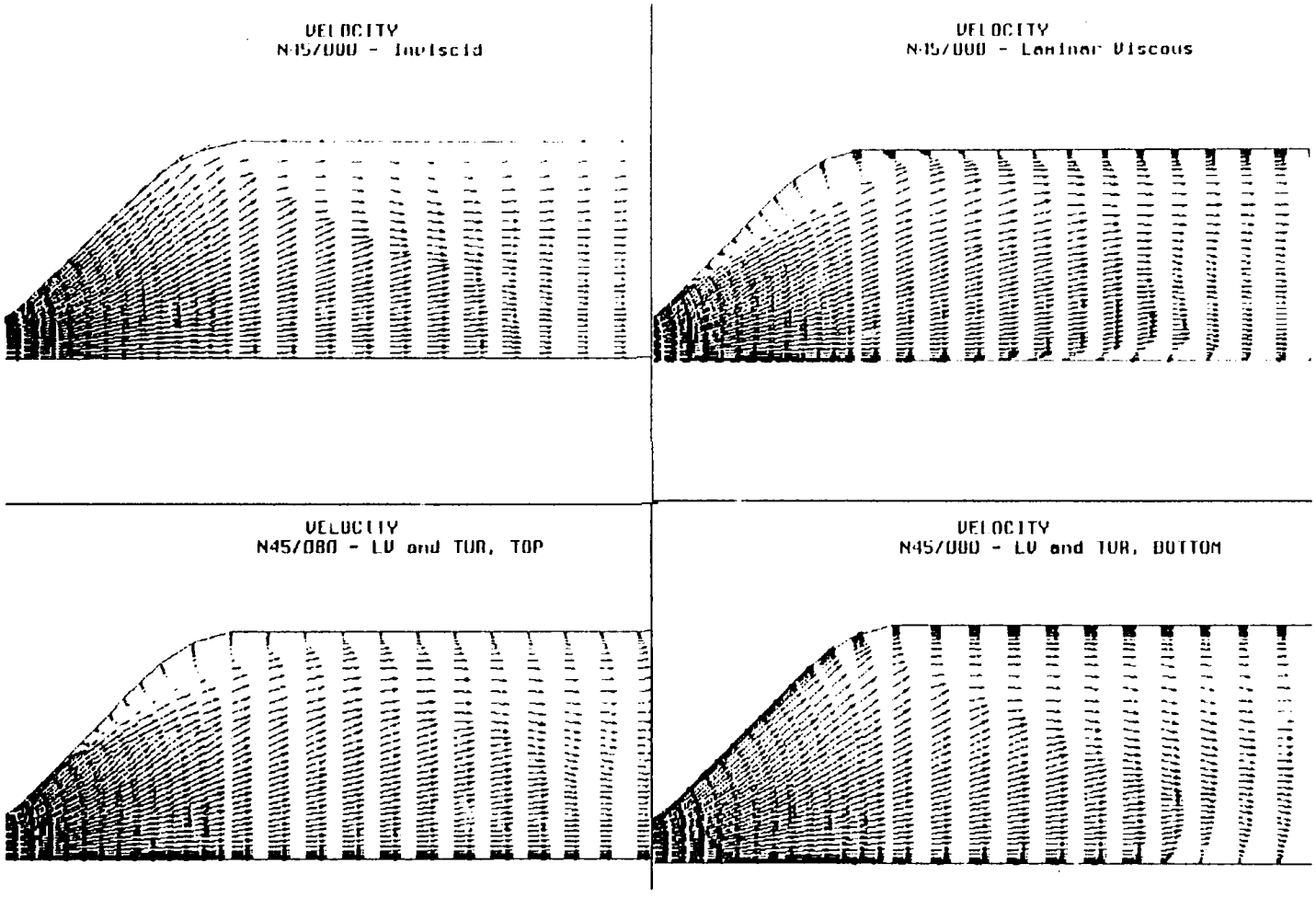

Figure 44. Comparison of the Inviscid, Laminar Viscous, and Turbulent Velocity Vectors Plots, 45° Nozzle.

7. REFERENCES

Amann, H. O. "Vorgaenge beim Start einer ebenen Reflexionsduese." Bericht Nr. 9/68 Ernst-Mach-Institut, Freiburg i. Br., Eckerstrase 4, 1968.

Amann, H. O. In An Album of Fluid Motion. Edited by Van Dyke. Sanford, CA: The Parabolic Press, p. 171, 1982.

Anderson, J. D., Jr. "Hypersonic and High Temperature Gas Dynamics." New York: McGraw-Hill, 1989.

Atwood, C. A. "An Upwind Approach to Unsteady Flowfield Simulation." AIAA paper, to be published.

Baldwin, B. S., and H. Lomax. "Thin Layer Approximation and Algebraic Model for Separated Turbulent Flows." AIAA-78-257, Huntsville, AL, January 1978.

Bennett, B. C., M. J. Abbett, and C. J. Wolf. "Viscous Effects of Blast Wave Flowfields." AIAA-86-0031, January 1986.

Byun, Y., J. Y. Lee, J. D. Anderson, Jr., and A. P. Kothari. "Unsteady Hypersonic Viscous Flow in Impulse Facilities." AIAA-90-0421, Reno, NV, January 1990.

Chakravarthy, S. R. "A New Class of High Accuracy TVD Schemes for Hyperbolic Conservation Laws." AIAA-85-0363, Reno, NV, January 1985.

Chakravarthy, S. R., and S. Osher. "Computing With High-Resolution Upwind Schemes for Hyperbolic Equations." Lectures in Applied Mathematics, vol. 22, pp. 57-86, 1985.

Coulter, G. "Blast Parametric Study Using a 1/57 Scale Single Driver Model of a Large Blast Simulator - Part I." BRL-MR-3597, U.S. Army Ballistic Research Laboratory, Aberdeen Proving Ground, MD, June 1987a.

Coulter, G. "Blast Parametric Study Using a 1/57 Scale Single Driver Model of a Large Blast Simulator - Part II." Draft Memorandum Report to be published, U.S. Army Ballistic Research Laboratory, Aberdeen Proving Ground, MD, November 1987b.

Deschambault R. L., and I. I. Glass. "An Update on Non-Stationary Oblique Shock-Wave Reflections: Actual Isopycnics and Numerical Experiments." Journal of Fluid Mechanics, vol. 131, pp. 27-57, 1983.

Glaz, H. M., P. Colella, I. I. Glass, and R. L. Deschambault. "A Detailed Numerical, Graphical, and Experimental Study of Oblique Shock Wave Reflections." UTIAS Report No. 285, CN ISSN 0082-5255, Institute for Aerospace Studies, University of Toronto, August 1986.

Goldberg, U., and S. R. Chakravarthy. "Prediction of Separated Flows With a New Backflow Turbulence Model." AIAA Journal, vol. 26, no. 4, pp. 405-408, April 1988.

Hikida, S., R. L. Bell, and C. E. Needham. "The SHARC Codes: Documentation and Sample Problems. Volume I: Inviscid Fluid Dynamics." SSS-R-89-9878, S-Cubed, A Division of Maxwell Laboratories, Inc., Albuquerque, NM, September 1988.

Hisley, D. M. "BLAST2D Computations of the Reflection of Planar Shocks From Wedge Surfaces With Comparison to Sharc and Stealth Results." BRL-TR-3147, U.S. Army Ballistic Research Laboratory, Aberdeen Proving Ground, MD, September 1990a.

Hisley, D. M. "Computational Studies for 1/57-Scale Large Blast Simulator (LBS) Configurations With the BLAST2D Code." BRL-TR-3152, U.S. Army Ballistic Research Laboratory, Aberdeen Proving Ground, MD, September 1990b.

Hisley, D. M., and G. A. Molvik. "Axisymmetric Calculations for the Large Blast/Thermal Simulator (LB/TS) Shock Tube Configuration." BRL-TR-2935, U.S. Army Ballistic Research Laboratory, Aberdeen Proving Ground, MD, October 1986.

Jones, E. "Lecture Notes on Viscous Flows II." University of Maryland, College Park, MD, January 1989.

Lock, G. D., and J. M. Dewey. "An Experimental Investigation of the Sonic Criterion for Transition From Regular to Mach Reflection of Weak Shock Waves." Experiments in Fluids, vol. 7, pp. 289-292, 1989.

Mark, A., and P. Kutler. "Computation of Shock Wave/Target Interaction." AIAA-83-0039, January 1983.

Molvik, G. A. "Computation of Viscous Blast Wave Solutions With an Upwind Finite Volume Method." AIAA-87-1290, Honolulu, HI, June 1987.

Opalka, K. O., and A. Mark. "The BRL-Q1D Code: A Tool for the Numerical Simulation of Flows in Shock Tubes With Variable Cross-Sectional Areas." BRL-TR-2763, U.S. Army Ballistic Research Laboratory, Aberdeen Proving Ground, MD, October 1986.

Pearson, R., K. O. Opalka, and D. M. Hisley. "Design Studies for the US Large Blast/Thermal Simulator." Proceedings of the Ninth International Symposium on Military Applications of Blast Simulation, Oxford, England, September 1985.

Rai, M. M. "An Implicit Form for the Osher Upwind Scheme." AIAA-84-0088, Reno, NV, January 1984.

Reichenbach, H. and K. O. Opalka. "An Optical Study of the Flow Start-Up Process in Four Convergent-Divergent Nozzles." Report No. E3-90, Ernst-Mach-Institut, Fraunhofer-Gesellschaft, Freiburg (B.r.), Germany, March 1990.

Roe, P. L. "Approximate Riemann Solvers, Parameter Vectors, and Difference Schemes." Journal of Computational Physics, vol. 43, pp. 357-372, 1981.

Shirouzu, M., and I. I. Glass. "An Assessment of Recent Results on Pseudo-Stationary Oblique-Shock-Wave Reflections." Presented at the 4th Mach Reflection Symposium, Tokyo and Sendai, 18-22 June 1984.

Steger, J. L., and R. F. Warming. "Flux Vector Splitting of the Inviscid Gasdynamic Equations With Application to Finite-Difference Methods." Journal of Computational Physics, vol. 40, pp. 263-293, 1981.

Steinbrenner, J., and C. Fouts. "A Workshop on Numerical Grid Generation Using GRIDGEN." Wright Patterson Air Force Base, OH, April 1990.

Yee, H. C. "Upwind and Symmetric Shock-Capturing Schemes." NASA TM-89464, May 1987.

INTENTIONALLY LEFT BLANK.

LIST OF SYMBOLS

A, B - inviscid flux Jacobian matrices

c - speed of sound

c_p - specific heat at constant pressure

c_v - specific heat at constant volume

e - total energy per unit volume

E, F - inviscid flux vectors

F_{MAX} - maximum of function $F(y)$

G - second order tensor of inviscid and viscous flux

h - total enthalpy per unit mass

i, j, k - unit vectors in Cartesian space

J - coordinate transformation Jacobian

k - coefficient of thermal conductivity

m_1, m_2 - constants

M - viscous flux Jacobian or Mach number

p - static pressure

Pr - Prandtl number, .72

Pr_t - turbulent Prandtl number, .9

q_x, q_y - heat transfer gradients

q - heat transfer vector

Q - vector of dependent variables

R - right eigenvector matrix or specific gas constant

R^1 - left eigenvector matrix

Re - Reynolds number

S - viscous flux vector or elemental surface area

t - time

T - absolute temperature

u, v - Cartesian velocity components

u_τ - friction velocity, $\sqrt{\tau_w/\rho_w}$

U, V - contravariant velocities

$\mathcal{V}$ - cell volume

x, y - Cartesian physical space coordinates

y^+ - law-of-the-wall coordinate, $\rho_w u_\tau y/\mu_w$

y_{MAX} - value of y at which $F(y)$ is maximum

β - compression parameter

δ_f - measure of numerical dissipation for first-order upwind scheme

γ - ratio of specific heats - constant of 1.4

ε - internal energy per unit mass

ζ - bulk coefficient of viscosity

λ - second coefficient of viscosity

Λ - diagonal matrix of eigenvalues

μ - first coefficient or molecular coefficient of viscosity

μ_t - eddy viscosity coefficient

ξ, η - curvilinear space coordinates

ρ - density

τ - computational time

$\tau_{i,j}$ - viscous stress tensor

σ - measure of change in flux

ω - vorticity

Subscripts

i, j - ξ, η direction indices

x, y - partial with respect to Cartesian coordinate

ξ, η - partial with respect to curvilinear coordinate

ref - reference quantity, taken to be ambient condition

Superscripts

n - time level

p - subiteration level

Roe - Roe-averaged quantity

Superscripts

~	-	dimensional quantity
+ or *R*	-	positive eigenvalues or right-running waves
- or *L*	-	negative eigenvalues or left-running waves
-	-	denotes cell-averaged quantity
^	-	denotes numerical flux consistent with physical flux
*	-	denotes intermediate value
1st	-	denotes first-order flux
2nd	-	denotes second-order flux

INTENTIONALLY LEFT BLANK.

No. of Copies	Organization
2	Administrator Defense Technical Info Center ATTN: DTIC-DDA Cameron Station Alexandria, VA 22304-6145
1	Commander U.S. Army Materiel Command ATTN: AMCDRA-ST 5001 Eisenhower Avenue Alexandria, VA 22333-0001
1	Commander U.S. Army Laboratory Command ATTN: AMSLC-DL 2800 Powder Mill Road Adelphi, MD 20783-1145
2	Commander U.S. Army Armament Research, Development, and Engineering Center ATTN: SMCAR-IMI-I Picatinny Arsenal, NJ 07806-5000
2	Commander U.S. Army Armament Research, Development, and Engineering Center ATTN: SMCAR-TDC Picatinny Arsenal, NJ 07806-5000
1	Director Benet Weapons Laboratory U.S. Army Armament Research, Development, and Engineering Center ATTN: SMCAR-CCB-TL Watervliet, NY 12189-4050
(Unclass only)1	Commander U.S. Army Armament, Munitions and Chemical Command ATTN: AMSMC-IMF-L Rock Island, IL 61299-5000
1	Director U.S. Army Aviation Research and Technology Activity ATTN: SAVRT-R (Library) M/S 219-3 Ames Research Center Moffett Field, CA 94035-1000

No. of Copies	Organization
1	Commander U.S. Army Missile Command ATTN: AMSMI-RD-CS-R (DOC) Redstone Arsenal, AL 35898-5010
1	Commander U.S. Army Tank-Automotive Command ATTN: ASQNC-TAC-DIT (Technical Information Center) Warren, MI 48397-5000
1	Director U.S. Army TRADOC Analysis Command ATTN: ATRC-WSR White Sands Missile Range, NM 88002-5502
1	Commandant U.S. Army Field Artillery School ATTN: ATSF-CSI Ft. Sill, OK 73503-5000
(Class. only)1	Commandant U.S. Army Infantry School ATTN: ATSH-CD (Security Mgr.) Fort Benning, GA 31905-5660
(Unclass. only)1	Commandant U.S. Army Infantry School ATTN: ATSH-CD-CSO-OR Fort Benning, GA 31905-5660
1	Air Force Armament Laboratory ATTN: WL/MNOI Eglin AFB, FL 32542-5000
	Aberdeen Proving Ground
2	Dir, USAMSAA ATTN: AMXSY-D AMXSY-MP, H. Cohen
1	Cdr, USATECOM ATTN: AMSTE-TC
3	Cdr, CRDEC, AMCCOM ATTN: SMCCR-RSP-A SMCCR-MU SMCCR-MSI
1	Dir, VLAMO ATTN: AMSLC-VL-D
10	Dir, BRL ATTN: SLCBR-DD-T

INTENTIONALLY LEFT BLANK.

USER EVALUATION SHEET/CHANGE OF ADDRESS

This laboratory undertakes a continuing effort to improve the quality of the reports it publishes. Your comments/answers below will aid us in our efforts.

1. Does this report satisfy a need? (Comment on purpose, related project, or other area of interest for which the report will be used.) _____

2. How, specifically, is the report being used? (Information source, design data, procedure, source of ideas, etc.) _____

3. Has the information in this report led to any quantitative savings as far as man-hours or dollars saved, operating costs avoided, or efficiencies achieved, etc? If so, please elaborate. _____

4. General Comments. What do you think should be changed to improve future reports? (Indicate changes to organization, technical content, format, etc.) _____

BRL Report Number BRL-TR-3261 Division Symbol _____

Check here if desire to be removed from distribution list. ____

Check here for address change. ____

Current address: Organization _____
Address _____

DEPARTMENT OF THE ARMY
Director
U.S. Army Ballistic Research Laboratory
ATTN: SLCBR-DD-T
Aberdeen Proving Ground, MD 21005-5066

OFFICIAL BUSINESS

BUSINESS REPLY MAIL
FIRST CLASS PERMIT No 0001, APG, MD

Postage will be paid by addressee

Director
U.S. Army Ballistic Research Laboratory
ATTN: SLCBR-DD-T
Aberdeen Proving Ground, MD 21005-5066

NO POSTAGE
NECESSARY
IF MAILED
IN THE
UNITED STATES